Growth of cubic GaN by molecular-beam epitaxy on porous GaAs substrates

V. V. Mamutin, V. P. Ulin, V. V. Tret'yakov, S. V. Ivanov, S. G. Konnikov, and P. S. Kop'ev

A. F. Ioffe Physicotechnical Institute, Russian Academy of Sciences, St. Petersburg

(Submitted September 4, 1998)
Pis'ma Zh. Tekh. Fiz. **25**, 3–9 (January 12, 1999)

It is shown that GaN layers can be grown on (100)- and (111)-oriented porous single-crystal GaAs substrates by molecular-beam epitaxy with plasma activation of the nitrogen by an rf electron cyclotron resonance discharge. The resulting undoped epitaxial layers possessed *n*-type conductivity with a carrier concentration $\sim 10^{18}$. Data obtained by scanning electron microscopy and cathodoluminescence indicate that at thicknesses ~2000 Å, continuous layers of the cubic GaN modification are obtained regardless of the substrate orientation. © *1999 American Institute of Physics.* [S1063-7850(99)00101-9]

It is well known that the metastable cubic (β-GaN) phase has various electrophysical and luminescence parameters superior to those of the stable hexagonal modification (α-GaN), in particular it has a lower effective mass and higher carrier mobility, while the ionization efficiency of acceptor impurities is higher.[1] However, epitaxial growth of sufficiently high-quality β-GaN has not yet been successfully achieved. The main stumbling blocks here are growing the single-phase films and reducing their defect levels (the densities of mismatch dislocations and packing defects penetrating into the layer). One possible approach to solving this problem may involve using ''soft'' substrates capable of accommodating the elastic strains created in the heterostructure during its formation and subsequent cooling, and thus providing a sink for mismatch dislocations. In this respect the use of porous substrates[2] prepared from III–V single crystals is extremely promising for obtaining β-GaN. Here we study the possibility of growing GaN on porous GaAs substrates by molecular beam epitaxy.

Substrates of *n*-GaAs having a carrier concentration of $>10^{18}$ and oriented in the (100) and (111) *A* and *B* directions were treated in a 3M aqueous solution of HF. A pulsed anode bias of 8–14 V was applied to the cell at a frequency ~2 Hz. The maximum current density was ~0.6–1 A/cm^2. The pores, formed as a result of treating the GaAs with HF, do not have the form of rectilinear channels of triangular cross section with well-defined propagation anisotropy in the ⟨111⟩ directions. The largest (110–130 nm) and longest pores develop in all possible ⟨111⟩ V directions, intersecting the surface of the substrate with this orientation (Fig. 1a). Smaller pores (60–80 nm), extending in the ⟨111⟩*A* direction, have a higher density and a more uniform spatial distribution. The surface density of these pores is $\sim 10^9$ cm^{-2}. With the existence of pores, the degree of microroughness of the substrate surface increases, as does the density of elementary steps on the surface. In our opinion, this should promote the formation of a continuous epitaxial β-GaN film outside the pores even in the earliest stages of epitaxial growth and should impede the formation of spontaneous hexagonal-phase nuclei.

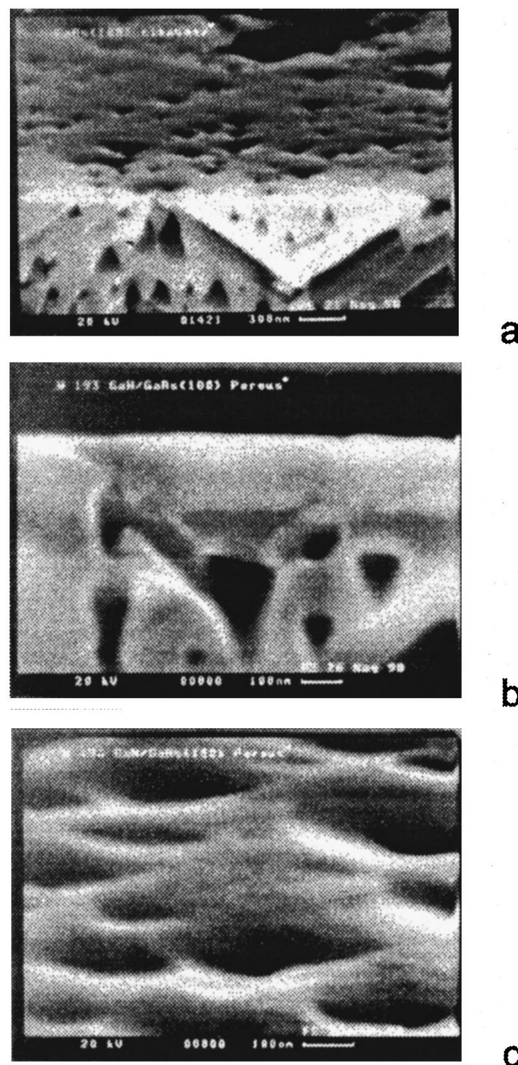

FIG. 1. a — Image of cleaved section and morphology of porous (100) GaAs substrate, b — image of cleaved section of layer grown on GaAs (100) substrate, and c — morphology of GaN layer on (100) GaAs.

 © 1999 American Institute of Physics

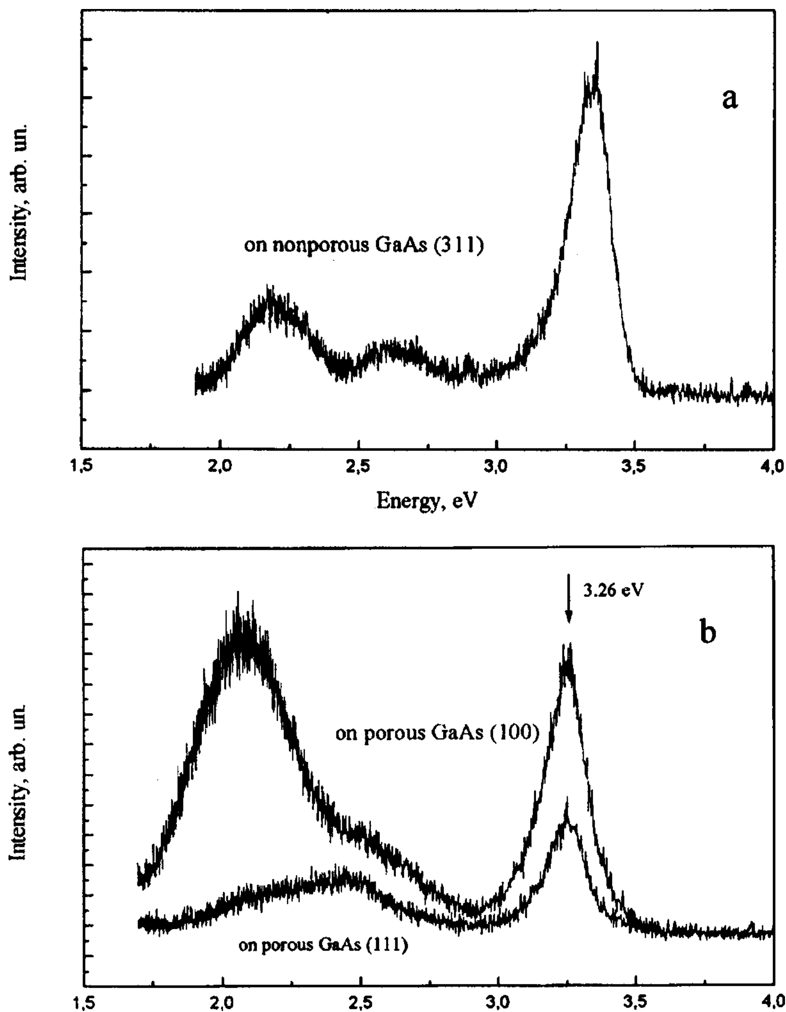

FIG. 2. a — Cathodoluminescence spectrum from GaN film grown on solid GaAs (311) substrate. Electron beam energy = 5 keV, current ~10 nA and sample temperature ~10 K, b — cathodoluminescence spectra from GaN films obtained on (100) and (111) porous GaAs substrates. The measurements were made under the same conditions.

The GaN was grown in a Russian-built ÉP-1203 molecular-beam epitaxy machine using an ASTEX (USA) electron-cyclotron-resonance nitrogen plasma source.[3] The morphology and crystal quality of the films were monitored during growth using high-energy electron diffraction.

The growth chamber and the source were evacuated using a Turbovac 560 turbomolecular pump with an effective speed of up to 350 l/s, which was dependent on the geometry of the growth chamber. The source was mounted on one of the standard flanges of the molecular beam epitaxy machine.

Layers of GaN were grown on GaAs (111) *A* and *B* and (100) substrates at temperatures between 550 and 560 °C to avoid thermal dissociation of the GaAs. Each growth process began with outgassing and removal of the GaAs–electrolyte interaction products from the porous layer. Above 400 °C changes in the high-energy electron diffraction pattern indicated that the surface had been purified and oxides removed. The surface was then nitrided for 10–15 min in an activated nitrogen stream. A layer of GaN was then grown at 550 °C and minimum growth rate. The growth processes were then investigated at various temperatures and growth rates in the range 0.01–0.5 E/s. For the GaAs (100) and (111) substrates, a high-energy electron diffraction pattern corresponding to cubic GaN was observed during the epitaxy.

The electrophysical properties of the layers were investigated using capacitance–voltage measurements. The resulting undoped layers exhibited *n*-type conductivity with electron concentrations $\sim 10^{18}$ cm^{-3}.

The thickness, morphology, and cross-sectional structure of the layers (cleaved sections) were investigated using a CamScan scanning electron microscope with a resolution ~100 E. Electron-microscope examinations of the films (Figs. 1b and 1c) revealed that at thicknesses ~2000 Å a continuous layer forms on the porous substrates, having a growth morphology characteristic of GaN under conditions of excess Ga, starting from Ga droplets present on the surface of the films. The luminescence properties of the layers were investigated using their cathodoluminescence.

The cathodoluminescence spectra were obtained at near liquid-nitrogen temperature with electron beam energies of 10 and 5 keV and a probe current ~5–10 nA. The spectra were recorded using a grating monochromator with a dispersion ~2 nm/mm^2 and a photon counting system.

The cathodoluminescence spectra from films obtained on solid GaAs (311) substrates revealed three bands (Fig. 2a): 1) a short-wavelength band which is usually ascribed to an exciton bound at a neutral donor (DBE) in α-GaN with a maximum energy $E_{\max}\sim 3.36$ eV and a full width at half-maximum (FWHM) ~120 meV; a "yellow" defect band with $E_{\max}\sim 2.2$ eV, FWHM ~250 meV, and 3) a band with

E_{max}~2.65 eV, FWHM ~200 meV. Published data indicate that this line is attributed to donor–acceptor recombination[4] with impaired stoichiometry [Ga]/[N]>1 (Ref. 5). From our observations, this band is frequently present in the spectra of films obtained on GaAs at high temperatures (>620 °C), regardless of the other growth conditions, and in our opinion may be attributed to arsenic doping of the GaN films.[6]

For films grown on (100) and (111)-oriented porous GaAs substrates we observed edge luminescence (Fig. 2b) with a maximum energy E_{max}~3.26 eV and FWHM ~180 meV. This line may be assigned to DBE in β-GaN (Ref. 7). From the intensity ratio of the DBE line for GaN films obtained on (111)- and (100)-oriented porous substrates we can conclude that the films grown on the (100) substrate are of superior crystal quality. In addition, the cathodoluminescence spectra exhibited a complex emission band whose energy was close to the center of the GaN band gap. Resolving this band into its elementary components revealed a band with (E_{max}~2.07–2.17 eV, FWHM~250 meV) and a band with (E_{max}~2.5 eV, FWHM~420 meV). The first band may be described as ''red'' in consequence of the color of the emission and is an analog of the yellow band in α-GaN, while the second band with E_{max}~2.5 eV is ascribed to donor–acceptor recombination.

The results of analyzing the spectra indicate that epitaxial films of the cubic (β) modification of GaN were obtained on porous GaAs (100) and (111) substrates, whereas for nonporous substrates, α-GaN forms preferentially on (111) GaAs and two-phase GaN forms on (100) GaAs (Ref. 8).

In conclusion, we have demonstrated for the first time that (100) and (111)-oriented porous GaAs single crystals may be used as a soft substrate for growing epitaxial heterostructures using materials whose lattice constant and coefficient of thermal expansion differ appreciably. The films obtained possessed *n*-type conductivity with an electron concentration ~10^{18} cm^{-3}. Data obtained by scanning electron microscopy and cathodoluminescence indicate that at thicknesses ~2000 Å a continuous layer of cubic GaN was obtained regardless of the substrate orientation.

This work was partially supported by the program ''Physics of Nanostructures.''

[1] M. E. Lin, G. Xue, G. L. Zhou, J. E. Greene, and H. Morkoç, Appl. Phys. Lett. **63**, 932 (1993).
[2] S. Luryi and E. Suhir, Appl. Phys. Lett. **49**, 140 (1986).
[3] V. V. Mamutin, V. N. Zhmerik, T. V. Shubina, A. A. Toropov, A. V. Lebedev, V. A. Vekshin, S. V. Ivanov, and P. S. Kop'ev, Pis'ma Zh. Tekh. Fiz. **24**(12), 30 (1998) [Tech. Phys. Lett. **24**, 467 (1998)].
[4] A. Salvador, W. Kim, Ö. Aktas, A. Botchkarev, Z. Fan, and H. Morkoç, Appl. Phys. Lett. **69**, 2692 (1996).
[5] R. Dingle, D. D. Shell, S. E. Stokowski, and M. Iligems, Phys. Rev. B **4**, 1211 (1971).
[6] R. D. Metcalfe, D. Wickenden, and W. C. Clark, J. Lumin. **16**, 405 (1978).
[7] J. Menniger, U. Jahr, O. Brandt, H. Yang, and K. Ploog, Phys. Rev. B **53**, 1881 (1996).
[8] V. G. Antipov, A. S. Zubrilov, A. V. Merkulov, S. A. Nikishin, A. A. Sitnikova, M. V. Stepanov, S. I. Troshkov, V. P. Ulin, and N. N. Faleev, Fiz. Tekh. Poluprovodn. **29**, 490 (1995) [Semiconductors **29**, 946 (1995)].

Translated by R. M. Durham

Stability of a charged bubble in a dielectric liquid against radial perturbations

A. I. Grigor'ev

Yaroslavl State University

(Submitted June 3, 1998)
Pis'ma Zh. Tekh. Fiz. **25**, 25–29 (January 12, 1999)

It is shown that the critical conditions for instability of a charged vapor-gas bubble in a dielectric liquid against virtual radially symmetric volume perturbations are substantially less stringent than the critical conditions for it to be unstable against virtual distortions of the shape. © *1999 American Institute of Physics.* [S1063-7850(99)00401-2]

Investigations of the stability of charged bubbles in liquid dielectrics are of interest in connection with numerous geophysical, technical, and technological problems, ranging from electrical breakdown of liquid dielectrics to hydrodynamic cavitation and flotation.[1–5] Nevertheless, this problem is as yet at the initial stages of theoretical interpretation.

Let us assume that a liquid dielectric of permittivity ε contains a spherical bubble of radius R_0 with an ideally conducting surface (because of the high surface mobility of the carriers). This surface is exposed to the action of capillary forces from the surface tension of the phase boundary δ and the action of the electric field of the bubble's own charge Q. For an equilibrium spherical bubble the pressure balance condition should be satisfied at its walls:

$$P=P_v+P_g-2\delta/R_0+Q^2/8\pi\varepsilon R_v^4, \tag{1}$$

where P is the pressure in the liquid at the surface of the bubble, P_v is the saturated-vapor pressure of the surrounding liquid in the bubble, and P_g is the gas pressure in the bubble. In Eq. (1) the third term initially describes the capillary pressure beneath the spherical surface and the fourth term describes the pressure of the bubble's own electric field.

We shall assume that unlike the surrounding liquid, which is assumed to be incompressible, the gas and vapor filling the bubble are highly compressible, and we shall analyze the stability of the bubble against virtual radially symmetric changes in its volume. Such changes in volume may be caused by radially symmetric movements of the bubble walls, which for small bubbles will have short characteristic times. However, these times exceed the characteristic time for equalization of the gas pressure in the bubble, whose order of magnitude is determined by the ratio of the bubble radius to the velocity of sound in the gas–vapor mixture filling the bubble. Under these conditions, we shall take the saturated vapor pressure P_v to be constant and we shall assume that the gas pressure P_g varies adiabatically. Equation (1) can then be rewritten as

$$P=P_v+\left(P_0-P_v+\frac{2\sigma}{R_0}-\frac{Q^2}{8\pi\varepsilon R_0^4}\right)\left(\frac{R_0}{R}\right)^{3\gamma}-\frac{2\sigma}{R}+\frac{Q^2}{8\pi\varepsilon R^4}, \tag{1a}$$

where γ is the adiabatic exponent. The second term on the right describes the adiabatically varying gas pressure in the bubble.

We shall also assume that the motion of a viscous liquid characterized by the kinematic viscosity ν near a bubble whose walls move with radial symmetry is radially symmetric, i.e., is one-dimensional in a spherical coordinate system with its origin at the center of the bubble, and is therefore irrotational. We shall assume that at any time the gas–vapor mixture filling the bubble is homogeneous in the hydrodynamic and thermal senses. The equation for the radially symmetric motion of the walls of a spherical bubble obtained from the system of hydrodynamics equations for a viscous liquid with suitable boundary conditions and allowance for Eq. (1) is given as

$$\ddot{R}R+1.5\dot{R}^2-\rho^{-1}\left(P_0-P_v+\frac{2\sigma}{R_0}-\frac{Q^2}{8\pi\varepsilon R_0^4}\right)\left(\frac{R_0}{R}\right)^{3\gamma}+\frac{4\nu\dot{R}}{R}+\frac{2\sigma}{\rho R}-\frac{Q^2}{8\pi\varepsilon R^4}+\frac{P_v-P}{\rho}=0. \tag{2}$$

The dot over R denotes a time derivative, $\dot{R}\equiv dR/dt$, and ρ is the density of the liquid.

In terms of dimensionless variables such that $\rho=1$, $\sigma=1$, and $R_0=1$, Eq. (2) becomes

$$\ddot{X}X+1.5\dot{X}^2+\eta\dot{X}X^{-1}-\beta X^{-3\gamma}-WX^{-4}+X^{-1}-\beta_*=0; \tag{3}$$

$$X=\frac{R}{R_0};\quad \tau=\frac{t}{R_0^{3/2}}\left(\frac{2\sigma}{\rho}\right);\quad \eta=2\nu\left(\frac{2\rho}{\sigma R_0}\right)^{1/2};$$

$$W=\frac{Q^2}{16\pi\varepsilon R_0^3\sigma};\quad \beta_*=\frac{(P_v-P)R_0}{2\sigma};$$

$$\beta=\frac{R_0}{2\sigma}\left(P_0-P_v+\frac{2\sigma}{R_0}-\frac{Q^2}{8\pi\varepsilon R_0^4}\right),$$

where P_0 is the initial pressure in the liquid near the bubble, which is determined by the atmospheric pressure above the free surface and by the hydrostatic pressure of the liquid column above the bubble.

 © 1999 American Institute of Physics

Equation (3), like Eq. (2), is nonlinear; it cannot be solved analytically, but must be integrated numerically. However, some conclusions on the motion of the bubble walls can be gleaned from a qualitative analysis.

By substituting $Y \equiv \dot{R}$ and converting from t to a new independent variable X, we lower the order of Eq. (3), reducing it to the form

$$\frac{\partial Y}{\partial X}=\frac{1.5Y^2+\eta Y X^{-1}-\beta X^{-3\gamma}-W X^{-4}+X^{-1}-\beta_*}{-YX}. \tag{4}$$

Equation (4) has an isolated singular point * $X=X_*$; $Y=Y_*=0$, where X_* is the solution of the equation

$$\beta_* X^{3\gamma}-X^{3\gamma-1}+W X^{3\gamma-4}+\beta=0.$$

The terms X_* and Y_* characterize the radius and velocity of the bubble walls.

We linearize the numerator and denominator of Eq. (4) and construct a characteristic equation for the singular point. An analysis of this equation readily shows that depending on the physical parameters of the problem, the singular point can either be a saddle, where the bubble is unstable against virtual radially symmetric perturbations of its volume, or it can be a stable node when the bubble is stable. The relation among the parameters W, β, and β_*, separating the stable and unstable states of the bubble, then has the form (for $\gamma=4/3$)

$$W+\beta-0.1055\beta_*=0.$$

Under real conditions, when the value of the parameter β_* characterizing the difference between the saturated vapor pressure and the static pressure in the liquid surrounding the bubble does not differ appreciably from unity, the critical value of the sum of the parameters W and β for instability of the bubble against virtual radially symmetric perturbations of its volume is approximately an order of magnitude lower than the corresponding critical value for instability of the charged bubble against spheroidal distortions of its equilibrium spherical shape (at constant volume), which has the form[5]

$$W+\beta \geqslant 1. \tag{5}$$

Nevertheless, it should be borne in mind that the instability of a bubble against changes in volume for $W+\beta \neq 0$ merely implies that the equilibrium state determined by X_* and Y_* is unstable and that as a result of the instability, the bubble is transferred to another stable equilibrium state with radius X_+, which differs from X_*, while keeping its spherical shape. At this point it should be noted that Eq. (1a), which determines the equilibrium dimensions of a bubble in accordance with the Descartes rule of signs, has two real positive solutions, one corresponding to a stable state and the other corresponding to an unstable state. If the surface charge and gas pressure are fairly high, a bubble that is stable against radially symmetric virtual perturbations of its volume may become unstable against distortion of its shape as given by inequality (5).

To conclude, unlike the critical conditions for instability of a highly charged spherical droplet of incompressible liquid,[6,7] whose volume remains constant under arbitrary deformations of the droplet, the critical conditions for instability of a highly charged spherical gas–vapor bubble in a liquid dielectric are determined not by the virtual distortions of the bubble shape but by the virtual change in its volume accompanying radially symmetric deformations.

[1] C. G. Garton and Z. Krasucki, Trans. Faraday Soc. **60**, 211 (1964).
[2] Ya. E. Geguzin, *Bubbles* [in Russian], Nauka, Moscow (1985), 174 pp.
[3] V. V. Glazkov, O. A. Sinkevich, and P. V. Smirnov, Teplofiz. Vys. Temp. **29**, 1095 (1991).
[4] I. V. Pylaeva, O. A. Sinkevich, and P. V. Smirnov, Teplofiz. Vys. Temp. **30**, 367 (1992).
[5] A. I. Grigor'ev, V. A. Koromyslov, and A. N. Zharov, Pis'ma Zh. Tekh. Fiz. **23**(19), 60 (1997) [Tech. Phys. Lett. **23**, 760 (1997)].
[6] A. I. Grigor'ev and S. O. Shiryaeva, J. Phys. D **23**, 1361 (1990).
[7] A. I. Grigor'ev and S. O. Shiryaeva, Izv. Ross. Akad. Nauk Ser. Mekh. Zhidk. Gaza No. 3, 3 (1994).

Translated by R. M. Durham

Possibility of using a large orbit regime for operation at bounce-frequency harmonics in a free-electron maser with a guiding magnetic field

N. S. Ginzburg, I. É. Kamenetskiĭ, A. A. Kaminskiĭ, A. K. Kaminskiĭ, N. Yu. Peskov, S. N. Sedykh, and A. P. Sergeev

Institute of Applied Physics, Russian Academy of Sciences, Nizhniĭ Novgorod; Joint Institute for Nuclear Research, Dubna

(Submitted August 8, 1998)
Pis'ma Zh. Tekh. Fiz. **25**, 30–36 (January 12, 1999)

It is suggested that a free-electron maser based on the LIU-3000 accelerator (Joint Institute for Nuclear Research, Dubna) can be made to emit in the short-wavelength part of the microwave range by using radiation at harmonics of the bounce frequency of an electron beam propagating along a helical trajectory with a large gyration radius on the transverse inhomogeneity scale of the rf field and selectively exciting a cylindrical waveguide mode whose azimuthal index is equal to the number of the harmonic. © *1999 American Institute of Physics.* [S1063-7850(99)00501-7]

Free-electron masers with a guiding magnetic field are promising sources of strong microwaves. The highly efficient operation of these devices in the long-wavelength part of the microwave range has been demonstrated for amplifier[1,2] and oscillator[3] systems. These experiments used thin axial filamentary relativistic electron beams propagating in the field of a helical wiggler and a guiding longitudinal magnetic field. Interaction between particles and a synchronous wave of frequency ω and longitudinal number h took place at the fundamental harmonic $(n=1)$ of the bounce frequency $\Omega_b=2\pi v_\parallel/d$:

$$\omega - h v_\parallel = n\Omega_b, \tag{1}$$

where $v_\parallel$ is the translational velocity of the particles and d is the wiggler period. The propagation of 0.5–1 MeV particles through wigglers with a period of 3–7 cm produces radiation at wavelengths of 8–10 mm with an output power of 30–60 MW and an electron efficiency of 25–30% (Refs.1–3).

At a given particle energy, which depends on the type of accelerator used, the wavelength can in principle be shortened, either by reducing the wiggler period or by operating at harmonics of the bounce frequency. However, the constraints of electrical strength, thermal loads, and so on, make it difficult to produce current wigglers with periods of less than 3–5 cm. In addition, if the cross section of the interaction space is kept the same (which is a necessary condition for high-current relativistic electron beams), a reduction in the wiggler period is associated with an increase in the transverse inhomogeneity of the wiggler field, an increase in the spread of the velocities acquired by the particles in the wiggler, and therefore a lower efficiency.

Thus, a promising method of increasing the emission frequency of a free-electron maser is to operate at harmonics of the bounce frequency.[4,5] In this way, radiation with wavelenth shorter by a factor n times than the resonance at the fundamental harmonic can be obtained for the same geometric dimensions of the electron-optical system. Moreover, when an axisymmetric waveguide is used as the electrodynamic system, a thin axial filamentary beam in a helical wiggler can only emit in the waveguide mode whose azimuthal index m is equal to the number of the bounce harmonic, $m=n$. This allows selective discrimination of the excitation of parasitic modes. It should be noted that the proposed mechanism for selection of the working mode is similar to that used in so-called large-orbit gyrotrons.[6,7]

The energy exchange of a thin relativistic electron beam propagating in a helical wiggler along a standard helical trajectory with the translational velocity $v_\perp$ and orbit radius $a_\perp = v_\perp/\Omega_b$ and interacting under resonance conditions (1) with the $H_{m,k}$ mode of a circular waveguide, may be described by the following averaged equations:

$$\frac{dE}{dz} = \mathrm{Re}\left\{(-1)^m e A_0 \frac{v_\perp}{v_\parallel} J_{m-n}(\kappa_\perp R) \times e^{i(n-m)\Psi} J'_m(\kappa_\perp a_\perp) e^{j\Theta}\right\},$$

$$\frac{d\Theta}{dz} = \frac{1}{v_\parallel}(\omega - n\Omega_b) - h, \tag{2}$$

where $E=\gamma mc^2$ is the particle energy, $\Theta=\omega t - hz - n\Omega_b t$ is the phase of the particles relative to the synchronous wave, A_0 is the amplitude of the synchronous wave, $\kappa_\perp = \sqrt{\omega^2/c^2 - h^2}$ is the transverse wave number of the wave, $(R;\Psi)$ are the polar coordinates of the beam injection point, J_k is a Bessel function of order k, and J'_k is its derivative. The boundary conditions for a monoenergetic beam with unmodulated incoming phases have the form

$$E|_{z=0}=E_0, \quad \Theta|_{z=0}=\Theta_0 \epsilon [0,2\pi). \tag{3}$$

The factor $J_{m-n}(\kappa_\perp R)$ in Eq. (2a) describes the mechanism of mode selection according to the azimuthal index, as noted above. Obviously, when the beam is injected centrally $(R=0)$, only the $m=n$ mode has nonzero coupling with the beam. For this case we express Eq. (2) in a universal form for devices with predominant inertial bunching:[8]

 © 1999 American Institute of Physics

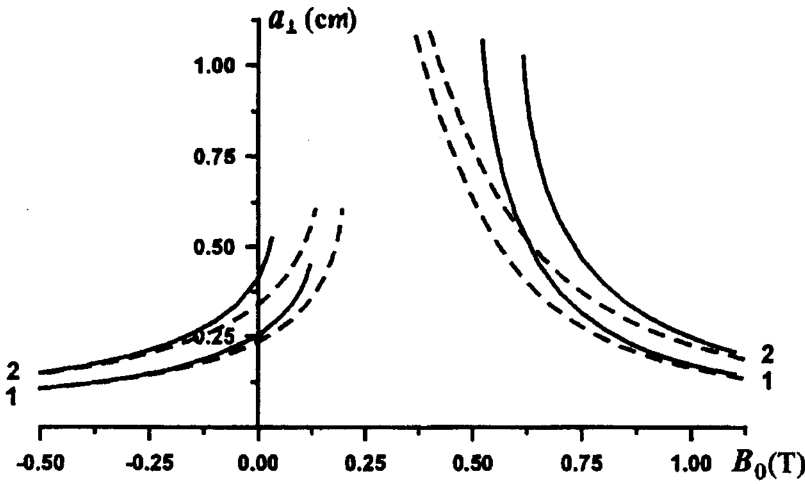

FIG. 1. Radius of electron gyration in an adiabatically switched helical wiggler as a function of the guiding magnetic field: *1* — $B_w=0.1$ T, *2* — $B_w=0.14$ T. The dashed curve gives the approximation using formula (7) ($d=6$ cm, $\gamma=2.6$).

$$\frac{du}{dZ}=\sin\Theta,\quad \frac{d\Theta}{dZ}=\Delta+u\ \mathrm{sign}\,\mu. \tag{4}$$

Here we use the dimensionless variables $Z=hz\sqrt{\alpha_s\rho\mu}$, $u=(1-\gamma/\gamma_0)\sqrt{\mu/\alpha_s\rho}$, $\Delta=[\beta_{ph}\beta_{\|0}^{-1}(1-n\Omega_b/\omega)-1]/\sqrt{\alpha_s\rho\mu}$ is the initial phase mismatch, $\mu=d\beta_{\|}^{-1}/d\gamma$ is the inertial bunching parameter,[8–10] $\alpha_s=eA_0/\gamma_0 hmc^2$, and $\rho=J_n'(\kappa_\perp a_\perp)\beta_\perp/\beta_\|$ is the coefficient of electron coupling with the wave. In terms of the new variables, the efficiency is given by

$$\eta=\sqrt{\frac{\alpha_s\rho}{\mu}}\frac{\hat{\eta}}{1-\gamma_0^{-1}},\quad \hat{\eta}=\frac{1}{2\pi}\int_0^{2\pi}u\,d\Theta_0. \tag{5}$$

The maximum of the reduced efficiency $\hat{\eta}_{\max}=1.37$ is achieved for $\Delta_{\mathrm{opt}}=-1.3\mathrm{sign}\mu$, $L_{\mathrm{opt}}=3.9$. The oscillator starting current is

$$I_{st}=\frac{mc^3}{e}\frac{\gamma_0 SN}{\pi l^2 Q\mu\rho^2}, \tag{6}$$

where $S=\pi D^2/4$ is the cross-sectional area of the waveguide, l is the length of the interaction space, $N=(1-4m^2/\kappa_\perp^2D^2)J_m^2(\kappa_\perp D/2)$ is the wave norm, and Q is the cavity Q-factor.

If the dipolarity condition $\kappa_\perp a_\perp\ll 1$ is satisfied, the coupling coefficients decrease fairly rapidly with increasing harmonic number: $\rho\approx(\kappa_\perp a_\perp)^{n-1}\beta_\perp/2^n\beta_\|(n-1)!$, which leads to a rapid increase in the oscillator starting current (6) and reduces the efficiency (5). However, efficient harmonic emission can only take place if the no-dipole condition $\kappa_\perp a_\perp\sim 1$ is satisfied, when the radius of the electron orbit is of the order of the transverse inhomogeneity scale of the wave field. Thus, operating a free-electron maser at higher harmonics involves increasing the radius of the electron orbits compared with that at the fundamental harmonic.

The radius of electron gyration (the radius of the electron orbit) acquired in an adiabatically switched wiggler field is plotted as a function of the guiding and wiggler field strengths in Fig. 1. It can be seen that the orbit $a_\perp\approx$ 0.2–0.3 cm required for efficient operation of a free-electron maser at harmonics may be achieved for parameters similar to the experimental conditions described in Ref. 3 with a so-called reverse guiding field[1,2] (denoted by the minus sign in Fig. 1), when the direction of particle gyration in the helical wiggler is opposite to their direction of gyration in the guiding field. Under these conditions, the radius of particle gyration in the wiggler may be approximated by[9,10]

$$a_\perp=\frac{eH_w d}{2\pi\gamma mc(\omega_H+\Omega_b)}. \tag{7}$$

Theoretical analyses[3,11] indicate that operation of a free-electron maser under conditions far from cyclotron resonance, including regimes with a reverse guiding field, has the advantages that high-quality helical relativistic electron beams are formed in the wiggler and the sensitivity to the initial particle velocity spread is low. This is confirmed by the results of experiments[1–3] in which the maximum efficiency (25–30%) for millimeter free-electron masers with a guiding magnetic field was obtained under these conditions. The high efficiency of a free-electron maser with a reverse guiding field achieved at the fundamental harmonic of the bounce frequency in the long-wavelength part of the millimeter range suggests that a fairly high efficiency may also be predicted in experiments at harmonics in shorter-wavelength ranges.

We shall use the results of this analysis to assess the possibility of operating a free-electron maser based on the LIU-3000 accelerator at bounce-frequency harmonics in the short-wavelength part of the microwave range (this 1 MeV/200 A/200 ns accelerator is located at the Joint Institute for Nuclear Research, Dubna). A working electron transverse velocity $\beta_\perp\approx$ 0.2–0.3 (orbit radius $a_\perp\approx$ 0.2–0.3 cm) can be achieved in a wiggler with period $d=6$ cm and a wiggler field of 0.1–0.15 T with a reverse guiding field of around 0.2 T. For these parameters, 4 mm emission can be obtained when the free-electron maser is operated at the second harmonic of the bounce frequency and the $H_{2,1}$ mode of a 2 cm diameter circular waveguide is excited. Selective feedback can be achieved for the working mode by using a two-mirror Bragg cavity,[8] which consists of waveguide sections, rippled with a period of 2 mm and depth of 0.2 mm, separated by a section of regular waveguide.

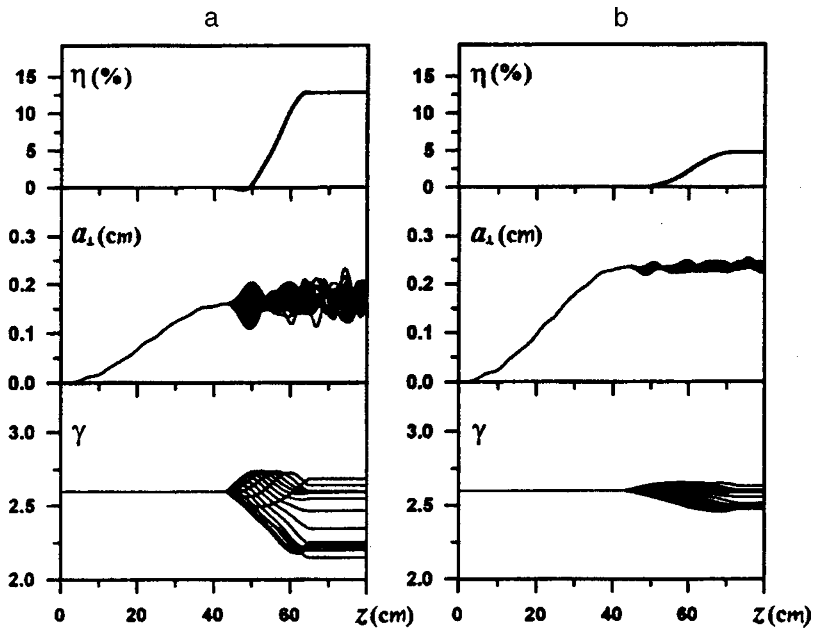

FIG. 2. Electron efficiency and also energies and gyration radii of particles with different initial phases for excitation of the $H_{m,1}$ mode, plotted as a function of the longitudinal coordinate z: $H_{m,1}$: a — $m=2$, $\lambda=4$ mm, $B_w=0.1$ T, $A_0=350$ kV/cm; b — $m=4$, $\lambda=2$ mm, $B_w=0.14$ T, $A_0=550$ kV/cm ($d=6$ cm, $\gamma=2.6$, $D=2$ cm, $B_0=-0.2$ T).

Analysis of the averaged equations (4) together with numerical simulation of the complete (nonaveraged) equations of particle motion plotted in Fig. 2a shows that for parameters close to the projected experimental conditions an efficiency of around 15% and an output power of 20–30 MW can be obtained at a wavelength of 4 mm. Equation (6) gives an oscillator starting current of 20 A for the cavity Q factor $Q\approx 2000$.

Emission at 2 mm can be achieved at the fourth harmonic of the bounce frequency with the $H_{4,1}$ mode excited. A simulation indicates that if the oscillator parameters are optimized, an efficiency of around 5% and an output power of around 5–10 MW may be predicted (Fig. 2b). For an oversize waveguide $D/\lambda \geqslant 10$, it is advisable to use a Bragg cavity open in the transverse direction to resolve the spectrum of transverse modes and maintain the feedback selectivity.[12,13]

[1] A. A. Kaminsky, A. K. Kaminsky, and S. B. Rubin, Part. Accel. **33**, 189 (1990).
[2] M. E. Conde and G. Bekefi, Phys. Rev. Lett. **67**, 3082 (1991).
[3] N. S. Ginzburg, A. A. Kaminsky, A. K. Kaminsky, N. Yu. Peskov, S. N. Sedykh, A. P. Sergeev, and A. S. Sergeev, IEEE Trans. Plasma Sci. **26**, 786 (1998).
[4] N. S. Ginzburg, Zh. Tekh. Fiz. **51**, 764 (1981) [Sov. Phys. Tech. Phys. **26**, 454 (1981)].
[5] W. B. Colson, IEEE J. Quantum Electron. **QE-17**, 1417 (1981).
[6] D. B. McDermott, N. C. Luhmann, A. Kupiszewski, and H. P. Jory, Phys. Fluids **26**, 1936 (1983).
[7] V. L. Bratman, Yu. K. Kalynov, N. G. Kolganov, V. N. Manuilov, M. M. Ofitserov, A. V. Savilov, V. L. Samsonov, and A. B. Volkov, in *Proceedings of the Third International Workshop on Strong Microwaves in Plasmas*, Nizhny Novgorod, Russia, 1996 Vol. 2, p. 745.
[8] V. L. Bratman, G. G. Denisov, N. S. Ginzburg, and M. I. Petelin, IEEE J. Quantum Electron. **QE-19**, 282 (1983).
[9] H. P. Freund, S. Jonston, and P. Sprangle, IEEE J. Quantum Electron. **QE-19**, 322 (1983).
[10] N. S. Ginzburg and N. Yu. Peskov, Zh. Tekh. Fiz. **58**, 859 (1988) [Tech. Phys. **33**, 523 (1988)].
[11] N. Yu. Peskov, S. V. Samsonov, N. S. Ginzburg, and V. L. Bratman, Nucl. Instrum. Methods Phys. Res. A **407**, 107 (1998).
[12] V. L. Bratman, G. G. Denisov, and V. L. Samsonov, in *Proceedings of the Second International Workshop on Strong Microwaves in Plasmas*, Nizhny Novgorod, Russia, 1993, Vol. 2, p. 690.
[13] N. S. Ginzburg, N. Yu. Peskov, and A. S. Sergeev, Pis'ma Zh. Tekh. Fiz. **18**(9), 23 (1992) [Sov. Tech. Phys. Lett. **18**, 285 (1992)].

Translated by R. M. Durham

Density distribution of a two-dimensional electron gas in a semiconducting heterostructure with a periodic gate electrode

Yu. A. Morozov and V. V. Popov

Institute of Radio Engineering and Electronics, Russian Academy of Sciences, Saratov Branch
(Submitted April 9, 1998)
Pis'ma Zh. Tekh. Fiz. **25**, 37–41 (January 12, 1999)

Calculations are made of the electron density distribution profiles in a layer of two-dimensional electron gas in a semiconducting heterostructure when reference and reverse potential biases are applied simultaneously to neighboring stripes of a periodic gate electrode. It is shown that for the structure parameters used experimentally the density distribution profile differs appreciably from rectangular and from sinusoidal. © *1999 American Institute of Physics.*
[S1063-7850(99)00601-1]

Periodically inhomogeneous two-dimensional electron systems in semiconducting GaAs/AlGaAs heterostructures have been studied in various experiments.[1,2] Wilkinson *et al.*[2] created a periodic electron density distribution in a two-dimensional system by applying a bias to a gate electrode fabricated as a periodic grating of metal stripes. These authors[2] interpreted the experimental data assuming a rectangular (or sinusoidal) electron density distribution profile.

Here the problem of the density distribution of a two-dimensional electron gas in a structure with a periodic gate electrode is solved using a strict electrodynamic formulation. Note that a similar approach was adopted in Ref. 3 to study how the built-in potential, created as a result of the formation of a Schottky barrier at the surface of the metal stripes of a gate electrode, influences the potential distribution in a layer of two-dimensional electron gas. Unlike Ref. 3, we shall consider a more general model, which can be used to study the case in which a reverse potential bias is applied to neighboring stripes of a gate electrode. In this case, the period of the spatial distribution of the charge in the two-dimensional electron layer is twice the period of the metal grating of the gate electrode. These structures are of particular interest because they exhibit the richest spectrum of plasma oscillations.[2]

Figure 1 shows a unit cell of this periodic structure. A grating of perfectly conducting metal stripes of width $2a$ is deposited on the surface of a dielectric layer *1* (AlGaAs) having relative permittivity ϵ_1 and thickness d. A two-dimensional electron layer is located at the interface between the dielectric *1* and a semiconducting substrate *2* (GaAs). The potential at the gate-electrode stripes A and B (relative to the potential of the two-dimensional electron layer) is defined as a superposition of the reference Φ_0 and reverse ϕ potential biases: $\Phi_A=\Phi_0+\phi$ and $\Phi_B=\Phi_0-\phi$.

The solution of the Laplace equation in the region of the unit cell $-L/2\leqslant x\leqslant 3L/2$, $0\leqslant y\leqslant d$ may be obtained as a superposition of the solutions obtained for the following values of the potentials at the grating stripes:

$$\Phi_A=\Phi_B=\Phi_0, \quad \phi=0, \tag{1}$$

$$\Phi_A=-\Phi_B=\phi, \quad \Phi_0=0. \tag{2}$$

A solution for the problem with the same potential (1) at the stripes was obtained by Davies and Larkin.[3] The reverse potential bias at the neighboring grating stripes (2) corresponds to an antisymmetric potential distribution relative to the plane $x=L/2$ for $x<L/2$ and $x>L/2$. Thus, it is sufficient to solve the problem in one of these regions, say for $x<L/2$, with the following boundary conditions:

$$\begin{aligned}&\Phi(x,0)=\phi, \quad |x|\leqslant a,\\ &\frac{\partial\Phi(x,0)}{\partial y}=0, \quad a<|x|\leqslant L/2,\\ &\Phi(x,d)=0, \quad \Phi(\pm L/2,y)=0.\end{aligned} \tag{3}$$

The second boundary condition corresponds to the absence of a normal component of the electric field at the nonmetallized surface of the dielectric *1* for $y=0$. This approximation is valid when $\epsilon\gg1$ (Ref. 3).

We shall solve the problem by using the following conformal transformation:

$$k_2\mathrm{sn}(W,k_2)=\mathrm{sn}(z/C,k_1), \tag{4}$$

which maps the region being studied in the plane $z=x+jy$ onto a rectangular region with homogeneous boundary conditions in the plane $W=\mathrm{Re}W+j\mathrm{Im}W$. The parameters k_1 and k_2 of the elliptic sine and the scale factor C are given by

$$CK(k_1)=L/2, \quad CK'(k_1)=d, \quad k_2=\mathrm{sn}(a/C,k_1). \tag{5}$$

Here $K(k_1)$ and $K'(k_1)$ are coupled complete elliptic integrals of the first kind. The solution of the Laplace equation with the set boundary conditions (3) has the form

$$\Phi(x,y)=\phi\left(1-\frac{\mathrm{Im}W(x,y)}{K'(k_2)}\right). \tag{6}$$

The charge density in the two-dimensional layer is given by

 © 1999 American Institute of Physics

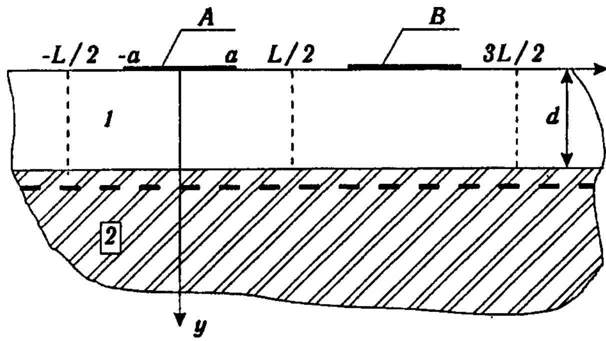

FIG. 1. Unit cell of a semiconducting heterostructure with a periodic gate electrode.

$$\sigma=\epsilon_0\epsilon_1\left(\frac{\partial\Phi}{\partial y}\bigg|_{y=d-0}-\frac{\partial\Phi}{\partial y}\bigg|_{y=d+0}\right)$$

$$=\frac{\epsilon_0\epsilon_1}{d}[\Phi_{\rm th}-\phi F(x)], \qquad (7)$$

where

$$F(x)=k_1\frac{K'(k_1)}{K'(k_2)}\sqrt{\frac{1-\mathrm{sn}^2(x/C,k_1)}{1-k_2^2k_1^2\mathrm{sn}^2(x/C,k_1)}}$$

and the real potential distribution over the depth of the surface layer in the semiconducting substrate *2* is taken into account using a phenomenological built-in threshold field $E_{\rm th}=\Phi_{\rm th}/d$. It follows from Eq. (7) that the potential $\phi\approx\Phi_{\rm th}$ corresponds to total depletion of the two-dimensional layer beneath the center of the gate-electrode stripe A $(F(0)\approx 1)$. This definition of the threshold field is used experimentally.[1,2]

Results of calculating the influence of the mark fraction of the gate-electrode grating $t=2a/L$ and the thickness d of the dielectric layer on the electron density distribution in the two-dimensional layer are plotted in Fig. 2. The data were obtained by superposing the solutions for the potentials at the grating stripes defined by conditions (1) and (2), where the continuation of the solutions into the region $x>L/2$ was made even and odd, respectively. Distribution *2* in Fig. 2a and curve *1* in Fig. 2b were obtained using values of the structure parameters corresponding to the experimental situation.[2] Note that in this case, our calculated dependence of the average charge density increment relative to its threshold on the gate voltage agrees with the experimental results obtained by Wilkinson *et al.*[2] to within graphical accuracy (see Fig. 3b from Ref. 2).

Figure 2b shows that the carrier concentration profile in the two-dimensional layer differs appreciably from the rectangular distribution defined *a priori* in Ref. 2. It can also be seen from Fig. 2a that for large t (curve *3*) depletion is observed over the entire two-dimensional layer and not only directly below the gate-electrode stripes. Even a negligible increase in the thickness of the dielectric layer d (or a decrease in the grating period L) sharply reduces the efficiency of modulation of the electron density in the plane of the two-dimensional layer (Fig. 2b). In this case, the distribution of the carrier concentration approaches sinusoidal.

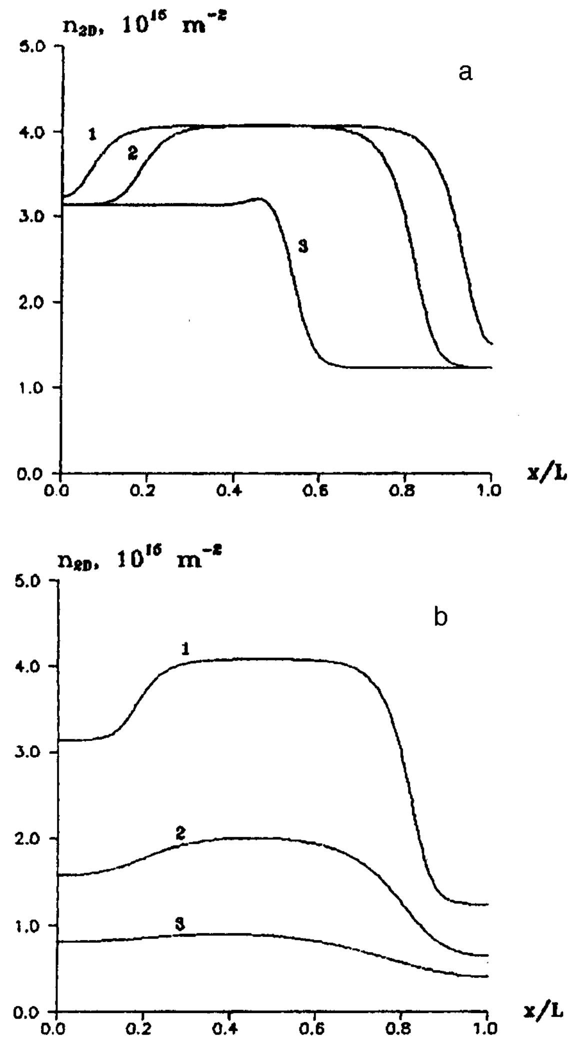

FIG. 2. Influence of the grating mark fraction (a) and dielectric layer thickness (b) on the electron density distribution profile for $L=1$ μm, $\epsilon_1=12$, $\Phi_{\rm th}=-0.43$ V, $\Phi_0=-0.2$ V and $\phi=0.1$ V: a — $d/L=0.07$; $t=0.1$ (*1*), 0.33 (*2*), 0.9 (*3*); b — $t=0.33$; $d/L=0.07$ (*1*), 0.14 (*2*), 0.28 (*3*).

This work was supported financially by the Russian Fund for Fundamental Research (Project Code 96-02-19211).

[1] J. P. Kotthaus, W. Hansen, H. Pohlmann, and M. Wassermeier, Surf. Sci. **196**, 600 (1988).
[2] R. J. Wilkinson, C. D. Ager, T. Duffield *et al.*, J. Appl. Phys. **71**, 6049 (1992).
[3] J. H. Davies and I. A. Larkin, Phys. Rev. B **49**, 4800 (1994).

Translated by R. M. Durham

Appearance of *S*-shaped sections on the current–voltage characteristics of *p–n* junction diodes exposed to microwave radiation

D. A. Usanov, A. V. Skripal', and N. V. Ugryumova

N. G. Chernyshevskiĭ State University, Saratov
(Submitted February 2, 1998; resubmitted August 5, 1998)
Pis'ma Zh. Tekh. Fiz. **25**, 42–45 (January 12, 1999)

An experimental investigation was made of the influence of microwave irradiation on the low-frequency current–voltage characteristics of *p–n* junction diodes. It is shown that when the microwave power increases to a certain level, a clearly defined *S*-shaped section appears on the current–voltage characteristic of the diode. This section becomes broader as the microwave signal increases further and then disappears when the microwave irradiation ceases. © *1999 American Institute of Physics.* [S1063-7850(99)00701-6]

The action of microwave radiation on diode structures having a *p–n* junction can qualitatively change their steady-state or low-frequency current–voltage characteristics. For instance, it has been shown[1,2] that the action of microwave radiation on a tunnel diode causes the section of negative differential resistance on its current–voltage characteristic to disappear. This behavior was attributed to lifting of the degeneracy of the electron–hole gas in the *p* and *n* regions and the appearance of a detector effect.

Here we report results of an experimental investigation of the influence of microwave radiation on the low-frequency current–voltage characteristics of 2A604 silicon planar-epitaxial multiplier diodes. These microwave diodes were inserted in a microstripe line. The diode was exposed to a 180 MHz signal fed via a controllable attenuator. The supplied power level was monitored by a power meter. In order to minimize the influence of thermal self-heating of the diode structure, the diode was supplied by a 4.5 kHz alternating voltage source connected in series via a 2 Ω resistance. The current–voltage characteristic was recorded using an oscilloscope. Figure 1 shows measured current–voltage characteristics for various microwave signal powers. It can be seen from these results that when the applied power is increased to 1500 mW, a well-defined *S*-shaped section appears on the current–voltage characteristic (curve *2*). As the power level is increased further, the voltage range in which the S-shape is observed becomes broader (curve *3*). In this case, low-frequency oscillations were observed in the supply circuit. When the microwave power was switched off, the current–voltage characteristic reverted to its initial profile, which is typical of diode structures with a nondegenerate *p–n* junction (curve *1*).

Estimates show that when a microwave power of ~ 1500 mW is supplied to a transmission line containing a diode, the amplitude of the microwave voltage at the diode does not exceed ~ 3 V bearing in mind that some of the power is reflected and some transmitted. The reverse-bias breakdown voltage for this type of diode is more than 35–40 V (Ref. 3), which eliminates effects observed during breakdown having any influence on the changes in the current–voltage characteristic accompanying the action of microwave radiation on the diode.

We note that for silicon epitaxial diodes with a Schottky barrier, the forward branch of the current–voltage characteristic has an *S*-shaped section of negative differential resistance[4] at current densities $j = 10^4 - 10^5$ A/cm^2, whose appearance is attributed to a superlinear increase in the conductivity of the epitaxial layer as the current density increases in this range of *j* values.[5,6]

For the diodes used in the experiments, the *S*-shaped sections of negative differential resistance (see Fig. 1) were observed at current densities between 2×10^2 and 4×10^2 A/cm^2, which is approximately two orders of magnitude lower than those in Ref. 4. This difference is caused by the fundamentally different physical factors responsible for the appearance of the S-shaped section of negative resistance when microwave and steady-state voltages act on the diode.

It was noted by Usanov *et al.*[1,2,7] that, unlike the experiment described in Ref. 4, the changes in the steady-state current–voltage characteristic observed when a microwave signal acts on diode structures are strongly influenced by

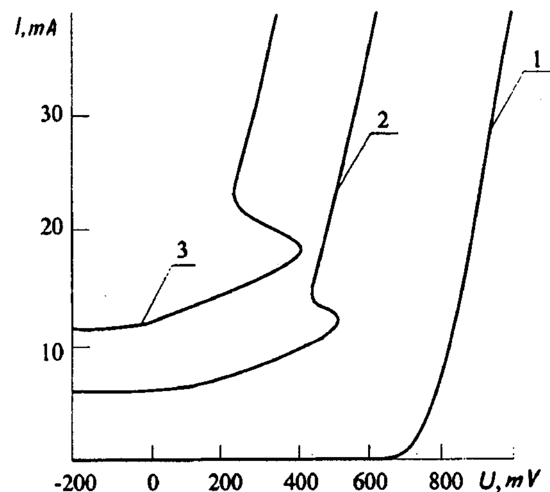

FIG. 1. Current–voltage characteristic of a *p–n* junction diode at various microwave powers; *P*, mW: *1* — 0, *2* — 1500, and *3* — 2600.

 © 1999 American Institute of Physics

changes in the position of the Fermi levels in the p and n-regions of the $p-n$ junction as a result the carriers being heated by the microwave field. Other influences are the detection effect and changes in the fraction of microwave power reflected from and absorbed by the diode as its level varies.

Additional experimental investigations carried out by us indicate that thermal heating of the array at temperatures between 300 and 400 K with and without microwave irradiation caused no qualitative changes in the current–voltage characteristics of the diode and merely shifted them toward lower applied voltages.

To conclude, it has been demonstrated experimentally for the first time that when $p-n$ junction diodes are exposed to microwave radiation at elevated powers, the current–voltage characteristics reveal an S-shaped section, i.e., a section of negative differential resistance. This effect is important for understanding the physics of the interaction between microwave radiation and semiconductor structures and for determining the operating characteristics of semiconductor devices based on structures with $p-n$ junctions.

[1] D. A. Usanov, B. N. Korotin, V. E. Orlov, and A. V. Skripal', Pis'ma Zh. Tekh. Fiz. **16**(8), 50 (1990) [Sov. Tech. Phys. Lett. **16**, 303 (1990)].
[2] D. A. Usanov, A. V. Skripal', B. N. Korotin, and V. E. Orlov, Pis'ma Zh. Tekh. Fiz. **19**(7), 81 (1993) [Tech. Phys. Lett. **19**, 220 (1993)].
[3] A. B. Nalivaĭko, A. S. Berlin, V. G. Bozhkov *et al.*, in *Handbook of Semiconductor Devices: Microwave Diodes*, edited by A. B. Nalivaĭko [in Russian], MGP ''RASKO,'' Tomsk (1992), 223 pp.
[4] Y. Yamamoto and H. Miyanaga, IEEE Trans. Electron Devices **37**, 1364 (1990).
[5] A. I. Malaĭ, Radiotekh. Elektron. **38**, 1510 (1993).
[6] A. I. Malaĭ, Mikroelektronika **23**(1), 35 (1994).
[7] D. A. Usanov, A. V. Skripal', and N. V. Ugryumova, Izv. Vyssh. Uchebn. Zaved. Ser. Élektron. No. 3–4, 48 (1997).

Translated by R. M. Durham

Behavior of total internal reflection in optical crystals

L. V. Alekseeva, I. V. Povkh, and V. I. Stroganov

Far Eastern State University of Communication Methods, Khabarovsk

(Submitted August 4, 1998)
Pis'ma Zh. Tekh. Fiz. **25**, 46–51 (January 12, 1999)

It is shown that a crystal can be cut so that one incident beam undergoing reflected from an inclined face inside the crystal excites four beams, two ordinary and two extraordinary, propagating in different directions. © *1999 American Institute of Physics.* [S1063-7850(99)00801-0]

The phenomenon of birefringence, in which a light beam in a crystal splits into two beams with mutually perpendicular polarizations, is well-known.[1–4] One of these beams is polarized in the plane of the principal cross section (the plane containing the crystal optic axis and the incident beam) and is called extraordinary (e), while the other is polarized (with the vector **E**) perpendicular to this plane and is called ordinary (o).

A type of birefringence known as double reflection has been analyzed in the literature, in which a beam splits into two, an ordinary and an extraordinary beam, while undergoing total internal reflection in a crystal.[3,5]

We shall show that a crystal can be cut so that as one incident beam is reflected from an inclined face inside the crystal it excites four beams, two ordinary and two extraordinary, propagating in different directions. This effect may be described as quadruple reflection and occurs because the planes of the principal cross sections differ for the incident and reflected beams.

An experiment was carried out using a prism cut from a uniaxial lithium niobate crystal. Figure 1a shows a top view of this prism. A ($\lambda=0.6328\,\mu$m) helium–neon laser beam *1* passes through the prism and is incident on an inclined face *2* positioned at an angle of 45° to one of the side faces *3*. Total internal reflection takes place at this face *2* and four beams *4–7* emerge from the prism, propagating in different directions. The planes of incidence and reflection of the beams lie in the plane of Fig. 1a. The angle of incidence β of beam *1* is 45°. The angles of reflection γ for the four beams are different. Two of the beams, *4* and *6*, are ordinary and two, *5* and *7*, are extraordinary. We denote the normal to the surface of reflection as *8*. The optic axis is located in the zz plane perpendicular to the direction of beam *1* and forms an angle of 45° with the plane of Fig. 1a. All the reflected beams lie in the same plane.

The spatial configuration of the reflected beams *4–7* was photographed and is shown in Fig. 1b.

The angles of reflection for beams *4–7* are denoted by

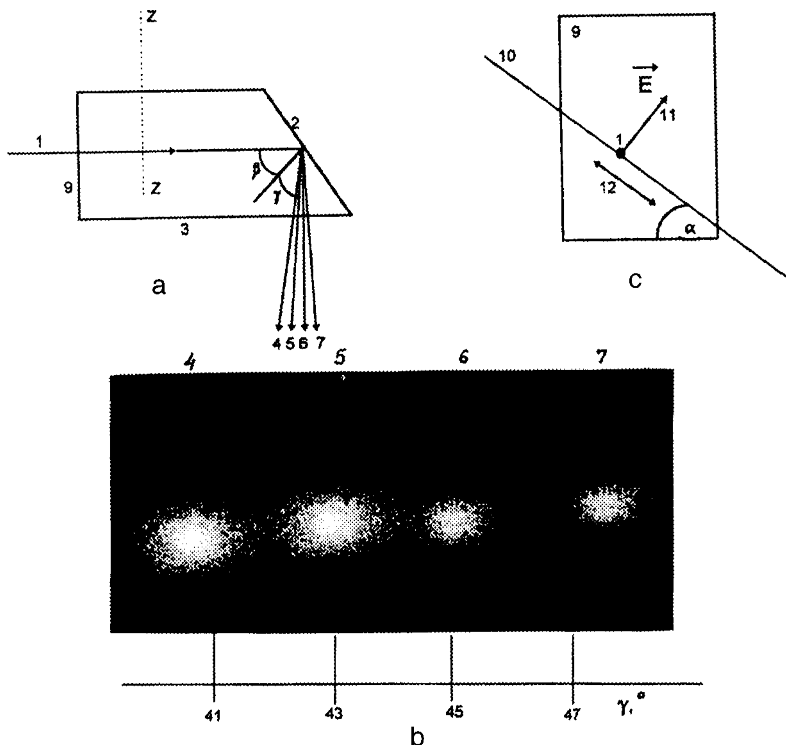

FIG. 1. Path of beams undergoing total internal reflection in an $LiIO_3$ crystal (a, c) and experimental observation of reflected beams (b): zz is the plane perpendicular to the plane of the diagram. The optic axis is located in the zz plane and is also at an angle of 45° to the plane of the diagram. *1* — laser beam, *2, 3* — crystal faces, *4–7* — reflected beams, *8* — normal to the surface of reflection, *9* — entry face of crystal, *10* — optic axis of crystal, *11* — direction of the vector **E** for the incident laser beam *1*, *12* — direction of transmission of Polaroid, β is the angle of incidence, γ is the angle of reflection, and α is the angle between the optic axis *10* and the upper or lower faces of the prism. The subscripts ''o'' and ''e'' correspond to the ordinary and extraordinary beams. The arrows indicate the direction of the electric field vector **E** for the reflected optical beams (b). Types of interaction: *4* — $e\rightarrow o$, *5* — $e\rightarrow e$, *6* — $o\rightarrow o$, *7* — $o\rightarrow e$. Angles of reflection, deg: *4* — 40.9, *5* — 42.8, *6* — 45, *7* — 47.52.

 © 1999 American Institute of Physics

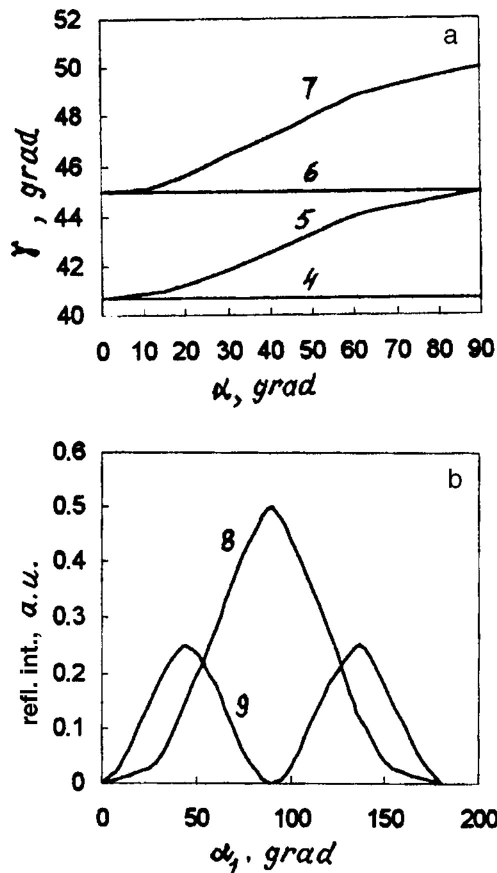

FIG. 2. Angles of reflection γ as a function of the position of the optic axis in the prism (a) and intensities of the reflected beams as a function of the direction of the vector **E** in the incident laser beam (b). Types of interaction: *4* — $e\rightarrow o$, *5* — $e\rightarrow e$, *6* — $o\rightarrow o$; *7* — $o\rightarrow e$; *8* — $e\rightarrow o$, $e\rightarrow e$, *9* — $o\rightarrow e$, $o\rightarrow o$ — experimental points. Curves *4–7* are plotted for the reflected beams *4–7*, respectively; *8* — for beams *4* and *5*; *9* — for beams *6* and *7*.

$\gamma_{eo}, \gamma_{ee}, \gamma_{oo}$, and γ_{oe}, respectively. The subscripts to the angles of reflection γ correspond to the types of interaction of the beams in the crystal. For example, for γ_{eo} the first subscript (e) indicates that beam *1* incident on the inclined face of the prism is extraordinary and the second subscript (o) indicates that the reflected beam is ordinary. That is to say, for $e\rightarrow o$ (beam *4*) and $o\rightarrow e$ (beam *7*) interactions, the beams are reflected anisotropically from the inclined face of the prism (with the plane of polarization being rotated on reflection).

The laws of reflection for beams *4–7*, respectively, can be written as follows:

$$n_e \sin\beta = n_o \sin\gamma_{eo}, \quad (1)$$

$$n_e \sin\beta = n_e(\gamma_{ee}) \sin\gamma_{ee}, \quad (2)$$

$$n_0 \sin\beta = n_o \sin\gamma_{oo}, \quad (3)$$

$$n_0 \sin\beta = n_e(\gamma_{oe}) \sin\gamma_{oe}. \quad (4)$$

In all cases, the angle of incidence is $\beta = 45°$. The refractive indices are $n_0 = 1.8830$ and $n_e = 1.7367$ ($\lambda = 0.6328$ μm) (Ref. 6).

The angles of reflection calculated using formulas (1)–(4) are plotted in Fig. 2a. It can be seen that for two types of interaction $e\rightarrow e$ and $o\rightarrow e$ the angles of reflection γ_{ee} (beam *5*) and γ_{oe} (beam *7*) depend on the position of the optic axis in the zz plane (the angle α).

We shall give the formulas for the intensity of the reflected beams. Before the entry face of the prism *9* we set a Polaroid whose direction of transmission is the same as the direction *12* (Fig. 1c). In this case, the measured angle of rotation of the Polaroid α_1 is zero. Then for beams *4–7* the intensities of the reflected beams are respectively

$$I_{eo} = 0.5I \sin^4\alpha_1, \quad (5)$$

$$I_{ee} = 0.5I \sin^4\alpha_1, \quad (6)$$

$$I_{00} = 0.25I \sin^2 2\alpha_1, \quad (7)$$

$$I_{oe} = 0.25I \sin^2 2\alpha_1. \quad (8)$$

When the laser beam *1* enters the prism, it is transformed into two beams, ordinary and extraordinary, propagating in the same direction perpendicular to the optic axis of the prism (Fig. 1a). In this case, for the beams incident on the inclined face *2* of the prism, the plane of the principal cross section is at an angle of 45° to the plane of Fig. 1a and passes through the incident beam.

For the reflected beams the plane of the principal cross section forms an angle of 90° with the plane of Fig. 1a and is also perpendicular to the plane of the principal cross section for the incident beams. With this configuration of the planes of the principal cross section, any of the beams incident on the inclined face *2* (ordinary or extraordinary) has a component of the vector **E** positioned at an angle other than 0 or 90° relative to the plane of the principal cross section for the reflected beams. This component of **E** excites two reflected beams, ordinary and extraordinary. Thus, the incident ordinary beam *1* excites two reflected beams, ordinary and extraordinary, and the incident extraordinary beam *1* also excites two beams, extraordinary and ordinary, on being reflected from the face *2*. Thus, four beams propagating in different directions emerge from the prism.

The intensity of the reflected beams is shown in Fig. 2b.

Note that this quadruple reflection effect is associated with a specific sample configuration cut from a crystal, which is unlike that usually used experimentally, where the crystal optic axis is specially positioned relative to the face of the sample, and may be observed in any anisotropic crystals, whether uniaxial or biaxial.

[1] A. F. Konstantinova, B. N. Grechushnikov, B. V. Bokut' *et al.*, *Optical Properties of Crystals* [in Russian], Nauka i Tekhnika, Minsk (1995), 302 pp.
[2] F. I. Fedorov and V. V. Filippov, *Reflection and Refraction of Light by Transparent Crystals* [in Russian], Nauka i Tekhnika, Minsk (1976) 224 pp.
[3] V. A. Kizel', Reflection of Light [in Russian], Nauka, Moscow (1973), 352 pp.
[4] M. Born and E. Wolf, *Principles of Optics*, 4th ed. (Pergamon Press, Oxford, 1969) [Russ. transl., earlier ed., Nauka, Moscow (1970), 856 pp.].
[5] V. I. Stroganov and V. I. Samarin, Kristallografiya **20**, 652 (1995).
[6] D. N. Nikogosyan and G. G. Gurzadyan, Kvant. Élektron. (Moscow) **14**, 1529 (1987) [Sov. J. Quantum Electron. **17**, 970 (1987)].

Translated by R. M. Durham

Formation of macroparticle charge in a classical Coulomb plasma

A. N. Tkachev and S. I. Yakovlenko

Institute of General Physics, Russian Academy of Sciences, Moscow
(Submitted June 23, 1998)
Pis'ma Zh. Tekh. Fiz. **25**, 52–55 (January 12, 1999)

An expression is derived for the average macroparticle charge and the electron temperature in a heated dense gas. © *1999 American Institute of Physics.* [S1063-7850(99)00901-5]

INTRODUCTION

In connection with the development of experimental investigations[1,2] of a thermal plasma containing macroparticles (dust particles) of high charge $Z_p \sim 10^2 - 10^4$, it is interesting to analyze the charging and neutralization kinetics of macroparticles in a high-temperature gas at atmospheric density. We use an average-charge model to derive simple expressions which relate the macroparticle charge and electron temperature to the macroparticle characteristics and the properties of the ambient gas. The results of our calculations agree with the experiments.

MODEL

We shall assume that macroparticles emit electrons as a result of thermal emission and, as the particle charge builds up, the electron work function increases. The electrons recombine as a result of electron–electron $(e-e)$ collisions and collisions with neutrals $(e-g)$ in the macroparticle field (three-body recombination). As a result of three-body $e-e$ recombination, the electrons cooled by collisions with neutrals undergo heating. We shall approximately assume that the plasma contains particles of the same charge Z_p (the most-represented-charge model, which is similar to the most-represented-ion model frequently used for a multiply charged ion plasma[3]). We shall assume that the macroparticle density N_p, gas density N_g, and temperature T_g are given parameters. Thus, for the electron density we have $N_e = Z_p N_p$.

Writing the balance equations for the density and temperature of the electron gas in the limits of a quasi-steady-state analysis, we obtain the following system of equations for the macroparticle charge Z_p and the electron temperature T_e:

$$\nu_{em}(Z_p,T_g)N_p = \frac{N_e}{\tau_{re}(Z_p,T_e)} + \frac{N_e}{\tau_{rg}(Z_p,T_e)},$$

$$\frac{\varepsilon_r N_e}{\tau_{re}(Z_p,T_e)} = Q_g. \qquad (1)$$

Here ν_{em} is the frequency of electron emission by a macroparticle, τ_{re} and τ_{rg} are the times for three-body $e-e$ recombination of electrons and for electron recombination as a result of the excitation of rotational degrees of freedom of the buffer gas molecules, Q_g is the electron energy losses as a result of collisions with the buffer gas, r_p is the macroparticle radius, $\varepsilon_r = Z_p e^2/r_p$ is the potential energy of an electron at the surface of a particle due to its charge, and W is the electron work function for an unexcited particle.

We shall assume that the frequency of electron emission from the surface of a macroparticle is equal to the Richardson frequency:

$$\nu_{em} = \frac{4\pi m_e T_g^2}{h^3}\exp\left[-(\varepsilon_r + W)\frac{1}{T_g}\right](4\pi r_p^2).$$

In a molecular gas with low degrees of ionization, three-body recombination as a result of the excitation of rotational degrees of freedom of the molecule is an important factor.[4,5] For the corresponding recombination time we assume:

$$\tau_{rg}^{-1} = \frac{8\sqrt{2\pi}}{3} Z_p^3 \frac{e^6}{\sqrt{m_e}} B_e \sigma_Q T_g T_e^{-9/2} N_e N_g.$$

Here B_e is the rotational constant of the molecule, T_e is the electron temperature (we shall subsequently assume that this is equal to the gas temperature $T_e = T_g$), and $\sigma_Q = (8\pi/15) Q a_0^2$ is the cross section for elastic scattering of an electron at a molecule with the quadrupole moment Q (here the quadrupole moment is in atomic units, $a_0^2 = 2.8 \times 10^{-17}\,\mathrm{cm}^2$).

For three-body $e-e$ recombination we take the following expression:[6,7]

$$\tau_{re}^{-1} = \frac{4}{5}\frac{2^{5/2}\pi^{3/2}}{9\sqrt{m_e}}\frac{e^{10} N_e^2 \Lambda}{T_e^{9/2}} Z_p^3,$$

$$\Lambda(\gamma) = (1/2)\ln(1 + 9/4\pi\gamma_e^3),$$

where $\Lambda(\gamma_e)$ is the Coulomb logarithm and $\gamma = (2e^6 N_e)^{1/3}/T_e$ is a parameter characterizing the degree of ideality of the electron gas. The cooling of the electrons by collisions with molecules is given by

$$Q_g = \sigma_Q B_e \sqrt{2T_e/m_e} N_g N_e.$$

SOLUTION OF THE EQUATIONS

We introduce the dimensionless quantities $\zeta = Z_p/Z_r$ and $\Theta = T_e/T_0$, where

$$Z_r \equiv r_p T_g / e^2,$$

$$T_0 = \left[\frac{\sqrt{2}}{6\pi^{3/2}}\frac{T_g^4 r_p^3 h^3 B_e \sigma_Q N_g N_p}{e^4 m_e^{3/2}}\exp\left(\frac{W}{T_g}\right)\right]^{-2/9}.$$

 © 1999 American Institute of Physics

The equations (1) then have the simple form

$$\zeta=\ln\left(\frac{b^{9/2}\zeta^{2/5}}{a\zeta+1}\right),\quad \Theta=b\zeta^{6/5}. \tag{2}$$

Here we have

$$a=\frac{2\pi}{15}\frac{e^4N_p\Lambda Z_r}{B_e\sigma_Q T_g N_g},\quad b=\left[\frac{16\pi^{3/2}}{45}\frac{r_p^5\Lambda T_g^6N_p^2}{\sigma_Q B_e T_0^5 N_g}\right]^{1/5}.$$

The first expression implicitly determines the dependence of the macroparticle charge on the other parameters of the macroparticle and the gas.

These formulas are valid when T_e is substantially higher than T_g. At low degrees of ionization when recombination heating can be neglected ($a=0$, $T_e=T_g$), we have $\zeta=\ln(\Theta^{9/2}/\zeta^5)$. In the range $\Theta=10-1000$, $\zeta=5-20$ the expression $\zeta=3.7\ln(0.1\Theta+2)$ is accurate to within 5%.

Note that unlike the case of complete thermodynamic equilibrium,[1] the parameters Z_p and N_e do not depend on the ionization potential of the buffer gas.

ESTIMATES

On the basis of the experimental conditions described by Fortov *et al.*[2] we take $T_e=T_g=0.146\,\mathrm{eV}$, $N_p\approx 5\times 10^7\,\mathrm{cm}^{-3}$, $N_g\approx 2.7\times 10^{18}\,\mathrm{cm}^{-3}$, and $W=2.75\,\mathrm{eV}$ (for CeO_2). For an analysis of three-body $e-g$ recombination we shall use the parameters of the nitrogen molecule: $B_e=2.5\times 10^{-4}\,\mathrm{eV}$, $\sigma_Q=4.5\times 10^{-17}\,\mathrm{cm}^2$. We then have $a=0.03$, $b=3$, $Z_r=41$, and $T_0=64.4\,\mathrm{K}$.

From this it follows that $\Theta=26.4$, $\zeta=5.7$, and hence $Z_p=230$. We attribute the difference from the value $Z_p\sim 500-1000$ reported in Ref. 2 to the rough ''corrugated'' surface of the dust particles.

This analysis holds if the electron mean free path in the gas is greater than the average distance between the macroparticles. This condition is satisfied for our particular case: $(\sigma_Q N_g)^{-1}(4\pi N_p/3)^{1/3}\approx 5$. The degree of ionization $\alpha=Z_pN_p/N_g\approx 10^{-8}$ is fairly low and this justifies the assumption that three-body recombination involving neutrals predominates.

For a simulation of the electron clouds around a charged dust particle see Ref. 8.

[1] V. E. Fortov and I. E. Yakubov, *Physics of Nonideal Plasma*, Hemisphere, New York (1990) [Russ. orig., Énergoatomizdat, Moscow (1994), 282 pp.].

[2] V. E. Fortov, A. P. Nefedov, O. F. Petrov, A. A. Samaryan, and A. V. Chernyshev, Zh. Éksp. Teor. Fiz. **111**, 467 (1997) [JETP **84**, 256 (1997)].

[3] V. I. Derzhiev, A. G. Zhidkov, and S. I. Yakovlenko, *Ion Emission in a Nonequilibrium Dense Plasma* [in Russian], Énergoatomizdat, Moscow (1986), 160 pp.

[4] F. I. Dalidchik and Yu. S. Sayasov, Zh. Éksp. Teor. Fiz. **49**, 302 (1965) [Sov. Phys. JETP **22**, 212 (1966)].

[5] L. I. Gudzenko and S. I. Yakovlenko, *Plasma Lasers* [in Russian], Atomizdat, Moscow (1978), 256 pp.

[6] A. V. Gurevich and L. P. Pitaevskiĭ, Zh. Éksp. Teor. Fiz. **46**, 1281 (1964) [Sov. Phys. JETP **19**, 870 (1964)].

[7] A. N. Tkachev and S. I. Yakovlenko, Kratk. Soobshch. Fiz. No. 7, 10 (1990).

[8] A. N. Tkachev and S. I. Yakovlenko, Preprint No. 8 [in Russian], Institute of General Physics, Russian Academy of Sciences, Moscow (1997), 20 pp.

Translated by R. M. Durham

Probing of a random phase screen by a focused spatially modulated laser beam: deflection of interference fringes

V. P. Ryabukho and A. A. Chausskiĭ

Institute of Problems in Precision Mechanics and Control, Russian Academy of Sciences, Saratov; Saratov State University

(Submitted July 28, 1998)
Pis'ma Zh. Tekh. Fiz. **25**, 56–61 (January 12, 1999)

Deflection of interference fringes in a diffraction field was investigated under conditions in which a laser beam with a regular interference structure was finely focused onto a random phase screen. It was established that the contrast of the average-intensity fringes depends analytically on the statistical parameters of the screen. © *1999 American Institute of Physics.* [S1063-7850(99)01001-0]

It has been established[1,2] that the contrast of the average-intensity interference fringes formed in a diffraction field when a moving random phase screen is illuminated by a focused, spatially modulated laser beam, depends on the statistical parameters of the screen. It was assumed that the light is diffracted at a large number of irregularities in the screen. Here we consider a different case when the size of the waist of a focused, spatially modulated laser beam on the surface of the screen is much smaller than the transverse dimensions of the irregularities in the screen, i.e., the probe beam ''resolves'' the irregularities in the screen. Such conditions are achieved when a spatially modulated laser beam is finely focused by an objective having a fairly large numerical aperture or by probing a random phase screen having large-scale irregularities. Under these conditions the diffraction field exhibits no speckle modulation and the pattern of interference fringes is almost the same as that observed in the absence of the screen. However, the position and to some extent, the shape of the fringes are determined by the parameters of the particular screen inhomogeneity situated under the focused laser beam. Transverse displacement of the screen is accompanied by deflection of the interference fringes as a result of an instantaneous change in the phase difference of the interfering waves. Thus, a slow-response photodetector records fringes of average intensity in the diffraction field whose contrast will be determined by the statistical characteristics of the random phase screen. The aim of the present study is to establish an analytical dependence of the contrast of the fringes on the statistical parameters of the random phase screen for conditions of fringe deflection.

As in Refs. 1 and 2, the spatially modulated laser beam has parallel interference fringes formed by the superposition of two Gaussian laser beams. When this beam is focused on the surface of a random phase screen, two light spots of diameter $2w_0 = 2\lambda f/\pi w$ are formed (Fig. 1) and the distance between them ρ_0 is determined by the period Λ_0 of the fringes, $\rho_0 = \lambda f/\Lambda_0$, where w is the beam radius in the aperture of the focusing objective with the focal length f. We shall assume that $2w_0$ is significantly smaller than the transverse dimensions of the irregularities $l_\phi : 2w_0 < l_\phi$.

A transverse displacement of the screen causes a random shift of the phases of each beam $\varphi_1(\boldsymbol{\rho}+\boldsymbol{\rho}_0/2)$, $\varphi_2(\boldsymbol{\rho}-\boldsymbol{\rho}_0/2)$ and a corresponding random shift $\Delta\zeta$ of the interference fringes in the diffraction field, i.e., the interference fringes are deflected. A slow-response photodetector records the average-intensity fringes whose contrast V is lower than that of the fringes of the illuminating beam V_0. We shall establish the relationship between the contrast V and the statistical parameters of the phase-screen irregularities: the variance of the phase fluctuations σ_ϕ, the inhomogeneity correlation length l_ϕ, and the inhomogeneity correlation coefficient $K_\phi(\Delta\boldsymbol{\rho})$, which reflects their mean statistical shape.

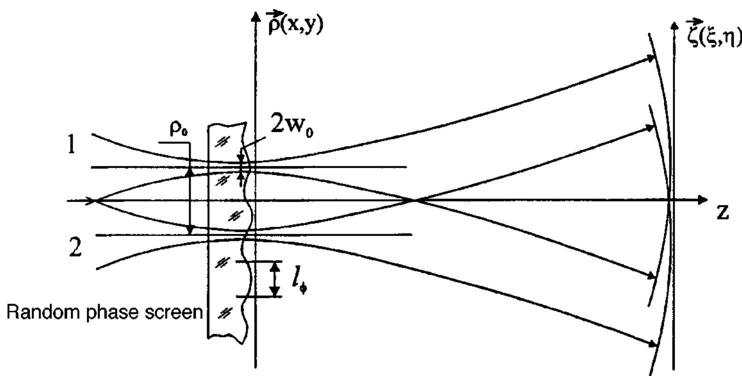

FIG. 1. Propagation of a focused spatially modulated laser beam through a random phase screen with large-scale irregularities.

In the Fresnel diffraction zone the complex amplitudes of the interfering fields $U_1(\boldsymbol{\zeta},z)$ and $U_2(\boldsymbol{\zeta},z)$ will have different amplitudes A_1 and A_2, different random phase shifts φ_1 and φ_2, and a relative deterministic phase shift $\Delta\Psi(\boldsymbol{\zeta},z)=2\pi\boldsymbol{\rho}_0\cdot\boldsymbol{\zeta}/\lambda z$ caused by the relative transverse shift ρ_0 of the constrictions of beams *1* and *2* in the plane of the screen (Fig. 1). Thus, we can write the following expression for the spatial distribution of the average intensity in the plane $(\boldsymbol{\zeta},z)$:

$$\langle I(\boldsymbol{\zeta},z)\rangle=\langle|U_1(\boldsymbol{\zeta},z)+U_2(\boldsymbol{\zeta},z)|^2\rangle$$
$$=|u(\boldsymbol{\zeta},z)|^2\Bigg\{A_1^2+A_2^2+2A_1A_2|\mu_{12}(\boldsymbol{\rho}_0)|\times\cos\left(\alpha+\frac{2\pi}{\lambda z}\boldsymbol{\rho}_0\cdot\boldsymbol{\zeta}\right)\Bigg\}, \quad (1)$$

where for a Gaussian illuminating beam we have $|u(\boldsymbol{\zeta},z)|=(w_0/w(z))\exp[-(\zeta/w(z))^2]$; $w(z)$ is the beam radius in the plane of observation $(\boldsymbol{\zeta},z)$ of the interference pattern; $\mu_{12}(\boldsymbol{\rho}_0)=\langle\exp[i\Delta\varphi_{12}(\boldsymbol{\rho}_0)]\rangle$ is the correlation coefficient of the complex amplitudes of the interfering light fields; $\alpha=\arg\mu_{12}(\boldsymbol{\rho}_0)$; $\Delta\varphi_{12}(\boldsymbol{\rho}_0)=\varphi_1(\boldsymbol{\rho}+\boldsymbol{\rho}_0/2)-\varphi_2(\boldsymbol{\rho}-\boldsymbol{\rho}_0/2)$. It follows from Eq. (1) that the contrast of the average-intensity fringes is given by

$$V=V_0|\mu_{12}(\boldsymbol{\rho}_0)|, \quad (2)$$

where $V_0=2A_1A_2/(A_1^2+A_2^2)$ is the contrast of the fringes in the absence of the random phase screen.

Assuming that the phase fluctuations $\Delta\varphi_{12}(\boldsymbol{\rho}_0)$ have Gaussian statistics, we can write the following expression[3,4] for the correlation coefficient $\mu_{12}(\boldsymbol{\rho}_0)$

$$\mu_{12}(\boldsymbol{\rho}_0)=\exp\{-\sigma_\phi^2[1-K_\phi(\boldsymbol{\rho}_0)]\}. \quad (3)$$

Thus, for the contrast of the average-intensity fringes we obtained the same dependence on the statistical parameters of the random phase screen as that obtained for the fringes in the boundary region using a broad, collimated, spatially modulated laser beam.[5] At this point, it is important to note that this dependence differs qualitatively from that obtained for the diffraction of a focused spatially modulated laser beam at a large number of screen irregularities.[2] In fact, in these two cases the contrast V of the fringes as a function of the inhomogeneity correlation length l_ϕ tends to change in opposite directions (see Fig. 2a in the present paper and Fig. 3b from Ref. 2). The decrease in V with increasing l_ϕ observed for diffraction at a large number of random phase-screen irregularities is caused by an increase in the average intensity of the scattered component relative to the intensity of the unscattered beam. The increase in V with increasing l_ϕ observed in the second case is caused by a reduction in the average amplitude of the fringe deflection. Figure 2a gives the contrast of the average-intensity fringes V/V_0 as a function of the correlation length of the screen irregularities l_ϕ under conditions of fringe deflection assuming that $K_\phi(\boldsymbol{\rho}_0)$ has the Gaussian form $K_\phi(\boldsymbol{\rho}_0)=\exp(-\boldsymbol{\rho}_0^2/l_\phi^2)$. Also plotted are the experimental data obtained for random phase screens

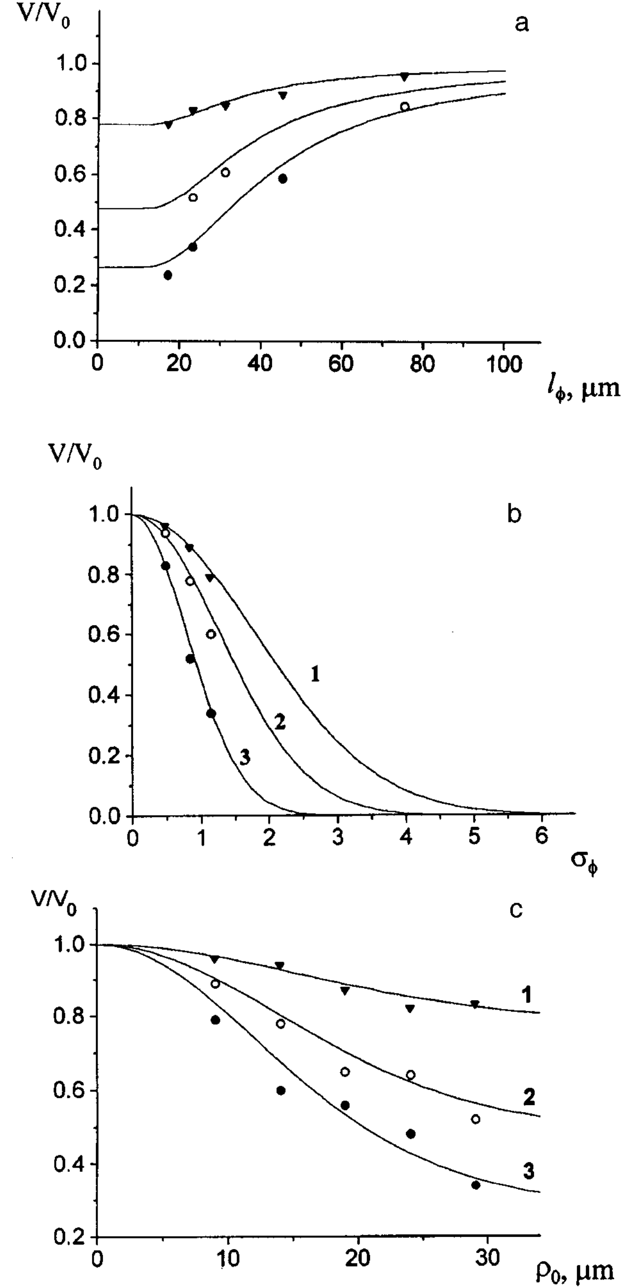

FIG. 2. Contrast of the average-intensity fringes in the fringe deflection regime, as a function of the statistical parameters of the random phase screen, showing both theoretical curves and experimental data: a — as a function of the correlation length l_ϕ of the screen irregularities for $\rho_0\approx 29$ μm: *1* — $\sigma_\phi=0.5$, *2* — $\sigma_\phi=0.86$, *3* — $\sigma_\phi=1.15$; b — as a function of σ_ϕ for $l_\phi=23$ μm: *1* — $\rho_0=9.5$ μm, *2* — $\rho_0=14$ μm, *3* — $\rho_0=29$ μm; c — as a function of ρ_0 for $l_\phi=23$ μm: *1* — $\sigma_\phi=0.5$, *2* — $\sigma_\phi=0.86$, *3* — $\sigma_\phi=1.15$.

(bleached speckle interferograms) with the statistical parameters σ_ϕ and l_ϕ predetermined using a method described by Ryabukho *et al.*[5]

The intermediate range of variation of l_ϕ corresponds to a third regime, i.e., diffraction at a small number of screen irregularities for which the incipient partially developed speckle fields have specific statistical properties.[6] The curve $V(l_\phi)$ giving the variation of the fringe contrast should be smooth over the entire range of l_ϕ with a minimum in this

third regime. The analytic expression for this dependence should include both characteristics of the illuminating beam w_0 and ρ_0 as parameters.

In both regimes an increase in σ_ϕ is accompanied by a reduction in the contrast of the fringes (Fig. 2b and Fig. 3a from Ref. 2), but this reduction obeys different laws.

An important characteristic of the deflection regime is that the contrast of the average-intensity fringes depends on the period Λ_0 of the fringes in the illuminating beam, since this determines the distance ρ_0 between the beam constrictions on the surface of the screen. Thus, by varying the period Λ_0, and therefore ρ_0, in a controlled fashion, it is possible to determine the statistical parameters of the screen from the measured dependence of the relative contrast of the fringes $V(\rho_0)/V_0$. Figure 2c gives theoretical curves of this dependence and experimental data obtained for the same samples as the data plotted in Figs. 2a and 2b.

This work was partially financed by a grant from the Russian Fund for Fundamental Research No. 96-15-96389 under the Program ''State Support for Leading Scientific Schools in the Russian Federation.''

[1] V. P. Ryabukho and A. A. Chausskiĭ, Pis'ma Zh. Tekh. Fiz. **21**(16), 57 (1995) [Tech. Phys. Lett. **21**, 658 (1995)].

[2] V. P. Ryabukho and A. A. Chausskiĭ, Pis'ma Zh. Tekh. Fiz. **23**(19), 47 (1997) [Tech. Phys. Lett. **23**, 755 (1997)].

[3] S. M. Rytov, Yu. A. Kravtsov, and B. I. Tatarskiĭ, *Principles of Statistical Radiophysics, Part 2, Random Fields*, 2nd ed., Springer-Verlag, Berlin, New York (1987); [Russ. orig. Nauka, Moscow (1978), 464 pp.].

[4] J. W. Goodman, *Statistical Optics* (Wiley, New York, 1985; Mir, Moscow, 1988, 528 pp.).

[5] V. P. Ryabukho, Yu. A. Avetisyan, and A. B. Sumanova, Opt. Spektrosk. **79**, 299 (1995) [Opt. Spectrosc. **79**, 275 (1995)].

[6] E. Jakeman, Opt. Eng. (Bellingham) **23**, 453 (1984).

Translated by R. M. Durham

Properties of micromagnetic structures in amorphous FeCuNbSiB alloys

E. E. Shalygina, L. M. Bekoeva, and A. N. Shalygin

M. V. Lomonosov State University, Moscow
(Submitted July 15, 1998)
Pis'ma Zh. Tekh. Fiz. **25**, 62–67 (January 12, 1999)

Results are presented of a magnetooptic investigation of the surface micromagnetic structure of FeCuNbSiB ribbons in the initial state and after annealing at 550 °C for 1 h. In the initial state the samples were amorphous, whereas after annealing they exhibited a nanocrystalline structure with typical grain sizes of 10–12 nm. Dispersion of the magnetic anisotropy was observed in the samples studied; this was responsible for the nonuniformity of their local magnetic properties. It was found that the linear dimension of the magnetic inhomogeneities in the initial and annealed samples was 120–150 and 50–70 μm, respectively. © *1999 American Institute of Physics.* [S1063-7850(99)01101-5]

In 1988 the first report appeared of a new iron-based alloy with composition $Fe_{73.5}Cu_1Nb_3Si_{13.5}B_9$ possessing unique magnetic properties (in particular, low hysteresis losses, high permeability, and almost zero magnetostriction).[1] The alloy was obtained by quenching from a melt in the form of an amorphous ribbon. After subsequent heat treatment at temperatures above the crystallization temperature, this material possessed a nanocrystalline structure with a grain size of $\sim$10–15 nm and exhibited supermagnetically soft properties.[2] Studies of the correlation between the structural and magnetic properties of FeCuNbSiB alloys in the initial state and after annealing have attracted attention among researchers. However, it should be noted that standard methods measure the bulk magnetic properties of magnetic materials, whereas we know[3] that the surface magnetic properties of amorphous materials can strongly influence their bulk magnetic characteristics.

Here we report results of a magnetooptic investigation of the surface micromagnetic structure of $Fe_{76.5}Cu_1Nb_3Si_{13.5}B_6$ ribbons in the initial state and after annealing at 550 °C for 1 h.

An $Fe_{76.5}Cu_1Nb_3Si_{13.5}B_6$ alloy was prepared by quenching from a melt in the form of amorphous ribbons 10 mm wide and 20 μm thick. In the initial state the ribbons were x-ray amorphous, whereas after annealing at 550 °C for 1 h they had a nanocrystalline structure with a grain size of $\sim$10–12 nm. Nanocrystallites were present in the residual amorphous matrix, occupying approximately 20% of the total volume. The ribbons were cut into pieces 15 mm long.

The micromagnetic structure of the ribbons was studied using a magnetooptic micromagnetometer having a surface sensitivity (depth of penetration) of $\sim$10 nm and a spatial resolution of up to 0.3 μm (Ref. 4). All the results described subsequently were obtained using the equatorial Kerr effect δ. In this method, an external magnetic field H is applied parallel to the surface of the sample and perpendicular to the plane of incidence of the light. The magnetization distribution $\delta(L)/\delta_s \sim M(L)/M_s$ and the local hysteresis characteristics $\delta(H)/\delta_s \sim M(H)/M_s$ were measured on both the contact and free sides of the ribbon samples. Here δ_s is the value of δ for $M = M_s$, where M_s is the saturation magnetization and L is the coordinate in the direction of the sample length. The measurement error for δ was less than 5%.

Figure 1a shows typical local magnetization curves measured for different sections of the contact side of the initial sample in a magnetic field H applied successively parallel and perpendicular to the ribbon length L (solid and dashed curves, respectively). In this case, the diameter of the light spot D on the surface of the sample was 1 mm. The local hysteresis loops were also measured and a typical one is shown in the inset to Fig. 1a. Figure 1b shows typical local magnetization curves obtained for the same sample in the field H parallel to L for $D = 20$ μm. Typical distributions of the magnetization in fields $H = 1$ and 2 kA/m are shown in Fig. 2a. In this case, the light spot ($D = 20$ μm) was moved along the central line over the sample length.

Clearly, this set of curves can be used to obtain the topography of the planar magnetization components and thus provide information on the surface micromagnetic structure of the ribbon. Figure 1c shows typical local magnetization curves measured on the contact side of an annealed sample in a field H applied successively parallel and perpendicular to the length of the ribbon (solid and dashed curves respectively). In this case, the diameter of the light spot D on the surface of the sample was 20 μm. A typical local hysteresis loop is shown in the inset to Fig. 2c. Typical distributions of the magnetization obtained for an annealed sample with $H = 0.5$ and 1 kA/m are shown in Fig. 2b. Similar measurements were made on the free side of the samples.

An analysis of these data yielded the following conclusions. The magnetization curves of the initial sample in the field H parallel and perpendicular to the length of the ribbon differ, which may be attributed to the existence of in-plane magnetic anisotropy. The easy axis of magnetization is parallel to the ribbon length L. The form of the local magnetization curves changes substantially on transition from one section to another (both for $D = 1$ mm and for $D = 20$ μm), as can be seen from Figs. 1a and 1b, and the magnetization distribution curves are irregular (Fig. 2a). These results indi-

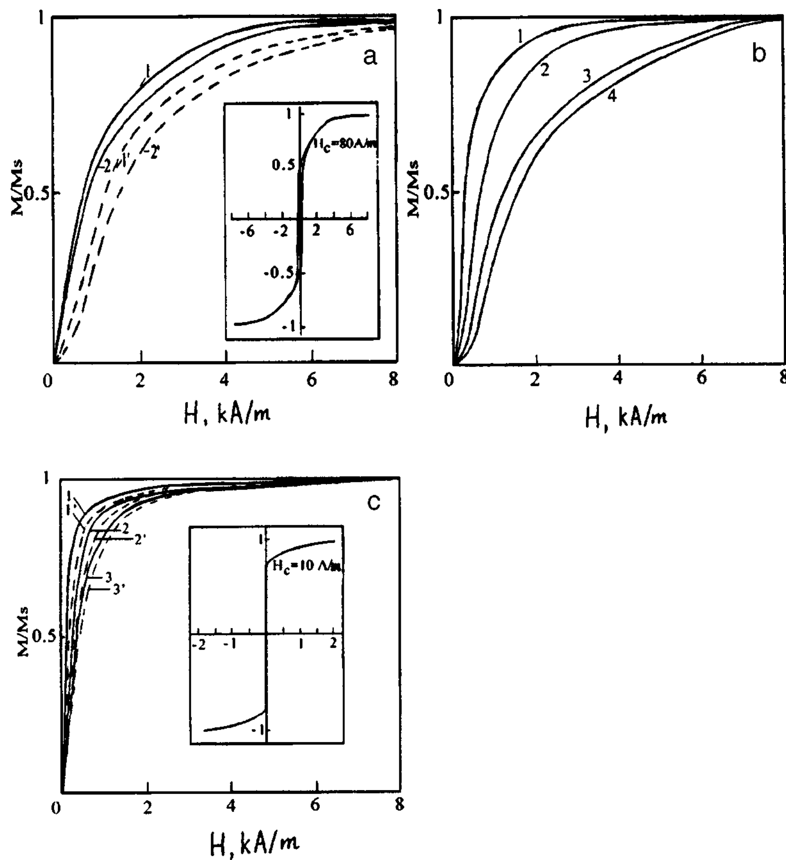

FIG. 1. Typical local magnetization curves of FeCuNbSiB amorphous ribbon in the initial (a, b) and annealed (c) states in a field H applied parallel (solid curves) and perpendicular (dashed curves) to the sample length. The insets show typical local hysteresis loops. The light spot diameter D on the sample was 1 mm (a) and 20 μm (b, c).

cate that the local surface magnetic properties of the initial sample are nonuniform at both the macroscopic and microscopic level, which may be caused by the dispersion of the magnetic anisotropy. It can be seen from Fig. 2a that the linear dimension of the magnetic inhomogeneities is 120–150 μm.

It was established that in the initial sample the local values of the saturation field and the coercive force H_C differ substantially. In particular, the minimum and maximum values of H_C are 0.08 and 0.2 kV/m. It should be noted that when similar measurements were made on the free side of the ribbon, we observed substantial changes in the values of H_C compared with those on the contact side. The value of H_C on the free side was approximately half that on the contact side and we also established that the value of H_C at the surface of the ribbons was ~6–8 times higher than the bulk value. The first factor can probably be attributed to differences in the morphology on the contact and free sides of the ribbon, while the second factor can be ascribed to the existence of defects (surface roughness and microcrystallites) typical of the surface layers of materials obtained by quenching from a melt.

The magnetization curves of the annealed sample in the field H parallel and perpendicular to the ribbon length differ negligibly, which indicates that the in-plane magnetic anisotropy is reduced (Fig. 2c). The difference between the local

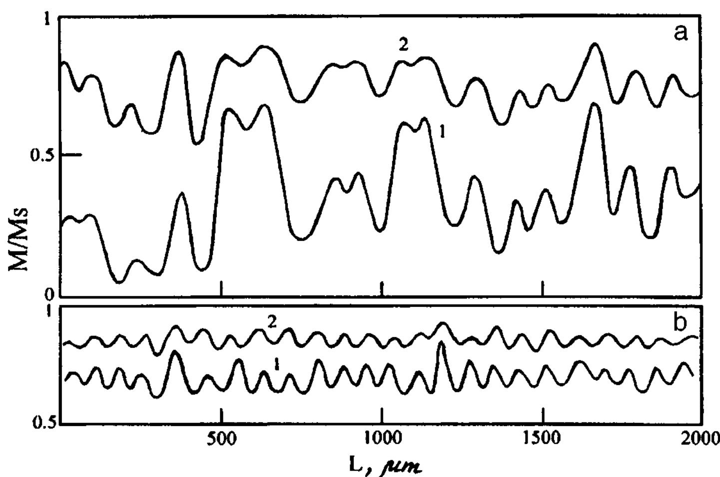

FIG. 2. Typical magnetization distributions for the initial sample for H=1 and 2 kA/m (a) and for the annealed sample for H=0.5 and 1 kA/m (b) (curves *1* and *2*, respectively) (D=20 μm).

magnetization curves even for $D=20\ \mu$m is also significantly reduced. Figure 2b shows that the linear dimension of the magnetic inhomogeneities in this sample is 50–70 μm. It was observed that the coercive force in the annealed sample is approximately ten times lower than that in the initial sample and the difference between the local values of H_C is less than 20%. Finally a comparison of the magnetization curves in Figs. 1a and 1c reveals that the initial magnetic permeability of the annealed sample is approximately five times higher than that of the initial sample.

To sum up, magnetooptic investigations of the micromagnetic structure of $Fe_{6.5}Cu_1Nb_3Si_{13.5}B_6$ amorphous ribbons having a nanocrystalline structure with grain sizes of 10–12 nm after annealing have shown that this material possesses dispersion of the magnetic anisotropy at both the macroscopic and microscopic level, which is responsible for the nonuniformity of the local magnetic properties. It was observed that after the ribbons had been heat-treated, the linear dimension of the magnetic inhomogeneities is approximately halved, the local values of the coercive force are reduced approximately tenfold, and the initial magnetic permeability is increased approximately fivefold compared with the same characteristics for the initial sample. It was established that in the annealed sample the difference between the local magnetic properties is less than 20%. Thus, we have observed that the structure of the amorphous material strongly influences its local surface magnetic properties.

[1] Y. Yoshizawa, S. Oguma, and K. Yamauchi, J. Appl. Phys. **64**, 6044 (1988).
[2] G. Herzer, IEEE Trans. Magn. **25**, 3327 (1989).
[3] G. S. Krinchik, E. E. Chepurova (Shalygina), B. K. Ponomarev *et al.*, Fiz. Tverd. Tela. (Leningrad) **28**, 2862 (1987) [Sov. Phys. Solid State **28**, 1605 (1986)].
[4] G. S. Krinchik, A. V. Shtaĭn, and E. E. Chepurova, Zh. Éksp. Teor. Fiz. **87**, 2014 (1984) [Sov. Phys. JETP **60**, 1161 (1984)].

Translated by R. M. Durham

Drag of an object in a supersonic flow with an isobaric region of energy release in front of the object

G. A. Luk'yanov

Institute of High-Performance Computations and Databases, St. Petersburg

(Submitted July 27, 1998)
Pis'ma Zh. Tekh. Fiz. **25**, 68–74 (January 12, 1999)

The problem of interaction between a steady-state supersonic flow and a planar isobaric region of energy release is solved. The solution is used to investigate the drag of an object in the wake behind the region of energy release. Conditions are determined for which the drag of the object can be reduced appreciably. The energy efficiency of this method of reducing the drag is studied. © *1999 American Institute of Physics.* [S1063-7850(99)01201-X]

The present paper is a further development of the author's earlier studies[1,2] of the drag and heat exchange of an object in a supersonic flow when a planar energy source (a gasdynamic discontinuity with a given energy release) is positioned in front of the object. Here a treatment is given of the two-dimensional steady-state problem of bulk isobaric energy release in a supersonic flow and the drag of an object located in the wake behind this region of energy release. The analysis is made using a model of non-viscous flow of a perfect gas.

The flow is shown schematically in Fig. 1. At a planar discontinuity *1* a unit mass of gas flowing through the discontinuity acquires energy q_1. This supply of energy leads to an increase in the temperature T and gas pressure p behind the discontinuity *1*. An analysis is made of the range of conditions corresponding to weak detonation.[3] In the flow region *2* (where b_1, b_2, and b_i are the initial, an arbitrary, and the final transverse dimensions of the region *2*) bulk energy supply takes place. The energy supply law ensures that isobaric flow takes place in region *2*. In what follows we assume that this planar isobaric region is a trapezium.

Interaction between the supersonic stream and the stream of expanding heated gas leads to the formation of an oblique shock wave with an angle of inclination φ relative to the incoming stream. The line k is a contact discontinuity separating the streams of heated and cold gas. Within the energy supply region, the angle of inclination of the line k with respect to the direction of the incoming stream is θ_i. The pressure in the shock layer *3* is equal to the pressure in region *2* ($p_2=p_3$). The isobaric region *2* is followed by a region *4* (near-wake region) in which the pressure p_4 is higher than that of the unperturbed flow p_∞. Thus, the heated gas continues to expand behind the region of energy release. The flow structure in region *4* depends strongly on the Mach number in the cross section $x=x_i$. For Mach numbers $M_i>1$ supersonic expansion takes place in region *4*, whereas for $M_i<1$ a closed subsonic flow region forms behind the region of energy release.

An object *5* having the characteristic transverse dimension b_m may be positioned in the wake region *4*. Heating and expansion of the gas in the energy release region together with expansion of the gas behind this region lead to a drop in the dynamic pressure $p_D=\rho u^2/2$ (where ρ and u are the density and velocity of the gas). This drop in p_D reduces the drag of an object moving in the wake behind this energy source.

The parameters behind the planar discontinuity *1* in the supersonic flow are determined from the mass, momentum, and energy conservation laws, supplemented by the equation of state. In this steady-state regime (weak detonation regime), the parameters p_1, ρ_1, u_1, and T_1 are determined by the parameters of the unperturbed stream and the heating parameter $\beta_1=q_1/c_pT_{0\infty}$, where $T_{0\infty}$ is the initial temperature of the unperturbed stream.[1–3] An upper bound is imposed on the limiting value of β_1 for steady-state energy supply conditions. The highest value of β_1 corresponds to Mach number 1 behind the discontinuity.

Using a quasi-one-dimensional description we find that the steady-state flow parameters of a nonviscous ideal gas in a region of bulk energy release are described by the following system of equations:

$$\rho_1u_1S_1=\rho_2u_2S_2,\quad \rho_2u_2\frac{du_2}{dx}=-\frac{dp_2}{dx},$$

$$\rho_2u_2S_2\left(\frac{u_2^2}{2}+c_pT_2\right)=\rho_1u_1S_1\left(\frac{u_1^2}{2}+c_pT_1\right)+Q,$$

$$p_2=\rho_2RT_2. \tag{1}$$

Here S is the cross-sectional area of the region of energy release, $Q=q_2\rho_1u_1S_1$ is the energy supplied to the flow per unit time during the bulk release of energy in the interval $0<x<x_2$, and q_2 is the energy supplied to this interval per unit mass.

For the case of isobaric flow in the region of energy release we find $p_2=p_1$, and it follows from Eqs. (1) that

$$u=u_1,\quad c_pT_2=c_pT_1+q_2,\quad \rho_2/\rho_1=T_1/T_2=S_1/S_2, \tag{2}$$

$$M_2/M_1=(T_1/T_2)^{1/2}=(1+q_2/c_pT_1)^{-1/2}. \tag{3}$$

In the isobaric region of energy release, the Mach number decreases monotonically with increasing x and a continu-

 © 1999 American Institute of Physics

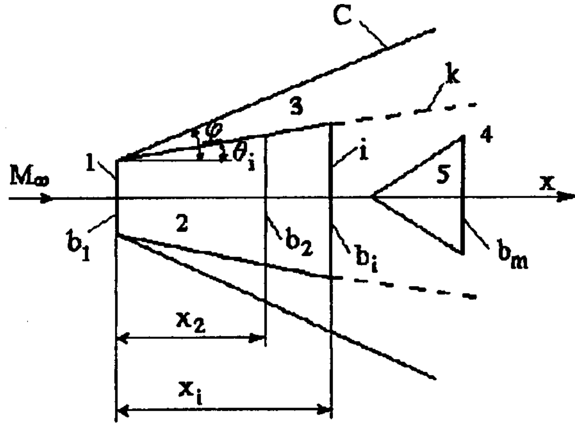

FIG. 1. Gasdynamic flow diagram.

ous transition may take place from supersonic to subsonic flow. This last factor is a fundamentally important advantage of this system of energy acting on a supersonic flow.

Two-dimensional isobaric flow is achieved in the region of energy release if this region has a trapezoidal geometry with $S_2 \sim b_2 \sim x_2$ (θ_i=const). For $p_2 = p_1 = p_3$ the relationship between p_2, M_∞, and θ_i is determined by the familiar relations for an oblique shock wave,

$$\frac{p_2 - p_\infty}{p_\infty} = \frac{2\gamma}{\gamma+1}(M_\infty^2 \sin^2\varphi - 1),$$

$$\tan\theta_i = 2\cot\varphi \frac{M_\infty^2 \sin^2\varphi - 1}{M_\infty^2(\gamma + \cos 2\varphi) + 2}. \quad (4)$$

Here γ is the specific heat ratio.

The parameters directly behind the region of energy release in the cross section $x = x_i$ are given by[4]

$$w_i = \frac{u_i}{u_\infty} = \frac{\lambda_1}{\lambda_\infty}(1+\beta_1)^{1/2}, \quad k_i = \frac{\rho_i}{\rho_\infty} = \frac{\lambda_\infty}{\lambda_1 \tau_2}(1+\beta_1)^{-1/2},$$

$$d_i = \frac{p_{D_i}}{p_D} = \frac{\rho_i u_i^2}{\rho_\infty u_\infty} = \frac{\lambda_1}{\lambda_\infty \tau_2}(1+\beta_1)^{1/2},$$

$$\tau_i = \frac{T_i}{T_\infty} = \frac{1-\lambda_1^2 \varepsilon}{1-\lambda_\infty^2/\varepsilon}(1+\beta_1)\tau_2, \quad (5)$$

$$n_i = \frac{p_i}{p_\infty} = \frac{\lambda_\infty}{\lambda_1}(1+\beta_1)^{1/2}\frac{1-\lambda_1^2/\varepsilon}{1-\lambda_\infty^2/\varepsilon}(1+\beta_1)\tau_2,$$

where $\tau_2 = T_i/T_1$, $\varepsilon = (\gamma+1)/(\gamma-1)$.

Of particular interest in terms of reducing the drag of an object moving in the wake behind this particular energy source is the region where the Mach numbers satisfy $M_\infty \gg 1$, and the heating parameter is $\beta_1 \ll 1$ (Ref. 4). In this region supplying energy to the gas at the discontinuity *1* heats the gas and increases the pressure, but has very little influence on the velocity and density. Thus, the following approximations[4] can be used to determine the parameters behind the discontinuity *1*

$$w_1 = u_1/u_\infty \approx 1, \quad k_1 = \rho_1/\rho_\infty \approx 1,$$

$$\tau_1 = T_1/T_\infty \approx \beta_1\left(1 + \frac{\gamma-1}{2}M_\infty^2\right) + 1,$$

$$n_1 = p_1/p_\infty \approx \tau_1, \quad M_i \approx M_\infty/\tau^{1/2}. \quad (6)$$

Under these conditions and with allowance for the relations (6), the formulas (5) have the form

$$w_i \approx 1, \quad k_i \approx \tau_2^{-1}, \quad d_i \approx \tau_2^{-1},$$

$$\tau_i \approx \tau_1\tau_2, \quad n_i \approx \tau_1, \quad M_i \approx M_\infty/\tau_i^{1/2}. \quad (7)$$

The drag of an object moving in the wake behind the energy source (Fig. 1) is formally given by

$$F = C_x \frac{\rho u^2}{2} S_m \quad (8)$$

and depends on the shape of the object, its position behind the region of energy release, and the parameters of the incoming stream (C_x is the drag coefficient and S_m is the area of the midsection of the object). The parameters of the stream behind the energy source vary, since $p_i > p_\infty$ holds. Numerical calculations in some formulation are required to make an accurate determination of F.

With a view to drawing some fundamental conclusions, we shall confine ourselves to some approximate estimates. The ratio of the drag of an object in the wake behind an isobaric bulk energy source to the drag of this object in an unperturbed external flow is given by

$$\omega = F/F_\infty = (C_x/C_{x\infty})(\rho u^2/\rho_\infty u_\infty^2). \quad (9)$$

When $M \gg 1$ and $\beta_1 \ll 1$ hold, we have $b_m = b_i$ for a moderately long object positioned directly behind the cross section $x = x_i$, and we can assume the approximation $\rho u^2 \approx \rho_i u_i^2$. Then, taking into account the relations (7), we obtain

$$\omega = (C_x/C_{x\infty})/\tau_2. \quad (10)$$

In this range of parameters, the possibilities for reducing the drag of the object are determined by the possibilities for obtaining high τ_2 values and the dependence of the drag coefficient C_x on the parameters behind the energy source.

The most interesting regimes for this system of reducing the drag of an object are those corresponding to hypersonic ($M_i \geq 3$) and subsonic ($M_i \leq 0.8$) flow regimes behind the energy source. The lowest drag can be achieved for subsonic values of M_i, fairly large τ_2, and objects having low values of C_x for subsonic flow, such as teardrop-shaped objects. For $M_i < 1$ the drag decreases monotonically with increasing τ_2.

When supersonic flow regimes are established behind the energy source, tapered objects have the lowest drag. Two flow regimes may be established for $M_i > 1$: flow with the bow shock attached to the nose of the object and flow with the shock wave detached from the object. By way of example, Fig. 2a gives the results of approximate calculations of the dependence of ω on τ_2 for various values of τ_1 for nonviscous flow of a gas with $M_\infty = 10$ and $\gamma = 1.4$ around a wedge with the expansion half-angle $\theta = 20°$. The point of the wedge is located in the cross section $x = x_i$, $b_m = b_1$. The calculations were made for conditions where an oblique

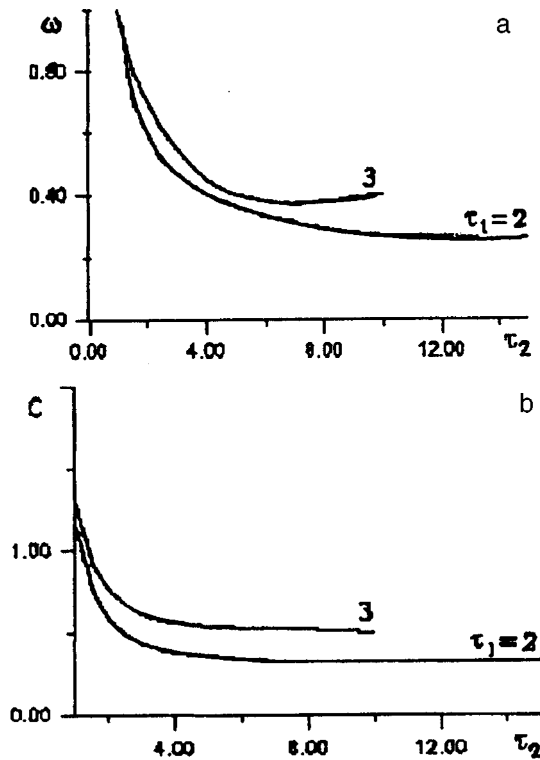

FIG. 2. Dependences of ω and C on τ_2 for $M_\infty = 10$, $\gamma = 1.4$, and various values of τ_1.

shock is attached to the front of the wedge ($M_i \geqslant 1.85, \tau_i = \tau_1 \tau_2 = T_i / T_\infty < 30$). For simplicity, it was assumed that the flow in region *4* behind the energy source is uniform and plane-parallel, and this pressure is zero.

The results plotted in Fig. 2a show that the reduction in the drag depends strongly on the values of τ_1 and τ_2. An increase in τ_1 narrows the range of variation of τ_2 (provided that $M \geqslant 1.85$). The reduction in drag is appreciable for small τ_1 and large τ_2. These conditions correspond to small angles θ_i and large ratios b_i / b_1. For low values of τ_1 there is a weakly defined minimum of ω at $\tau_2 = 20$–25 when the Mach number is $M_i = 2$–2.5. This minimum value of ω is 0.37 for $\tau_1 = 2$ and 0.26 for $\tau_1 = 3$.

Note in particular that in the range of parameters where the drag is reduced appreciably the thermal loads on the object are also reduced, since isobaric heating of the gas leads to a reduction in the dynamic pressure and the enthalpy flow per unit transverse area. A more detailed analysis of the thermal aspects is outside the scope of the present study.

We shall estimate the energy efficiency of this method of reducing the drag of an object. We confine our analysis to the most interesting range of parameters where $M_\infty \gg 1$ and $\beta_1 \ll 1$. The total energy dissipated in the uniform motion of an object in the presence of an energy source is $E = E_x + E_i = C_x \rho u^3 S_m / 2 + \rho_\infty u_\infty S_1 (T_i - T_\infty)$. When $E_i = 0$, the energy $E_\infty = C_{x\infty} \rho_\infty u_\infty^3 S_m / 2$ is expended in moving the object. To estimate the energy efficiency of this system we introduce the parameter

$$C = \frac{E_x + E_i}{E_\infty} = \omega + (\tau_i - 1) / C_{x\infty} \frac{\gamma - 1}{2} M_\infty^2 \frac{S_m}{S_1}. \tag{11}$$

For $\rho u^3 = \rho_i u_i^3$ and $S_m = S_i$ relation (11) has the form

$$C = (C_x / C_{x\infty}) / \tau_2 + (\tau_1 \tau_2 - 1) / C_{x\infty} \frac{\gamma - 1}{2} M_\infty^2 \tau_2. \tag{12}$$

For $\tau_2 \gg 1$ we have

$$C = (C_x / C_{x\infty}) / \tau_2 + \tau_1 / C_{x\infty} \frac{\gamma - 1}{2} M_\infty^2. \tag{13}$$

Figure 2b gives the parameter C as a function of τ_2 for various values of τ_1 for a gas with $M_\infty = 10$ and $\gamma = 1.4$ flowing around a wedge, corresponding to the values of ω plotted in Fig. 2a. A high energy efficiency is achieved for low τ_1 and fairly high τ_2. For $\tau_1 < 3$ in the range $\tau_2 \geqslant 5$ the value of C varies negligibly. A comparison between the energy efficiency of this system and a system with energy supply from a planar source[1] shows that isobaric energy supply is considerably more efficient.

[1] G. A. Luk'yanov, Pis'ma Zh. Tekh. Fiz. **24**(24), 76 (1998) [Tech. Phys. Lett. **24**, 980 (1998)].
[2] G. A. Luk'yanov, Preprint No. 04–98 [in Russian], Institute of High-Performance Computations and Databases, St. Petersburg (1998), 19 pp.
[3] G. G. Chernyĭ, *Gasdynamics* [in Russian], Nauka, Moscow (1988), 424 pp.
[4] G. A. Luk'yanov, Preprint No. 05–98 [in Russian], Institute of High-Performance Computations and Databases, St. Petersburg (1998), 20 pp.

Translated by R. M. Durham

Regular relief on a silicon surface as a structural defect getter

L. S. Berman, I. V. Grekhov, L. S. Kostina, E. I. Belyakova, E. D. Kim, and S. C. Kim

A. F. Ioffe Physicotechnical Institute, Russian Academy of Sciences, St. Petersburg

(Submitted July 24, 1998)
Pis'ma Zh. Tekh. Fiz. **25**, 75–80 (January 12, 1999)

An investigation was made to determine how a regular relief on the silicon surface influences gettering in silicon–silicon-dioxide structures. The regular relief was created by a photolithographic technique before oxidation and comprised an orthogonal network of overlapping bands. The gettering was determined from the isothermal relaxation of the capacitance of a silicon–silicon-dioxide structure after switching from strong inversion to even stronger inversion. It is shown that a regular relief at the silicon–silicon-dioxide interface is an effective getter at a depth of several hundred micron. © *1999 American Institute of Physics.*
[S1063-7850(99)01301-4]

Gettering is widely used in semiconductor technology to remove metal impurities and/or other structural defects from the electrically active region of a device. External gettering is accomplished by creating defects on the back side of the wafer, which act as sinks for undesirable defects. Various methods of external gettering exist.[1]

In our previous studies[2,3] we showed that a regular relief at the interface of as-grown silicon structures substantially reduces the density of boundary dislocations and the concentration of deep-level centers. This increases the minority carrier lifetime by more than an order of magnitude.

Here we study how a regular relief on the silicon surface influences the gettering in silicon–silicon-dioxide structures. We know that at a silicon–silicon-dioxide interface there is a thin defect transition layer which is itself a sink for deep-level centers (see Refs. 4 and 5, for example). Thus, we compared the gettering in silicon–silicon-dioxide structures with and without a regular relief.

SAMPLES

The samples were fabricated using n–Si⟨111⟩Cz with $\rho=15\,\Omega\cdot$cm and a wafer thickness of 300 μm. A regular relief was created by a conventional photolithographic method before oxidation, consisting of an orthogonal network of overlapping bands 50 μm wide, 0.2–0.3 μm deep, and 200 μm apart. The samples were oxidized in a dry and moist oxygen atmosphere at 1000 °C in the following sequence: 10 min dry O_2+100 min moist O_2+10 min dry O_2, giving an oxide thickness of 0.7 μm. After oxidation, the wafers were cooled to 600 °C for 50 min in the furnace. Aluminum contacts having diameters of 1–2 mm were deposited on the SiO_2 layer in vacuum. A vanadium silicide/aluminum ohmic contact to the silicon was made on the back.

Three groups of samples were fabricated: group 1 without a regular relief, group 2 with a regular relief on the back, and group 3 with a regular relief on the working surface.

MEASUREMENT METHOD

The gettering of deep-level centers was determined from the isothermal relaxation of the capacitance after switching the voltage from strong inversion to even stronger inversion. This method can detect deep-level centers in the upper and lower half of the band gap and can also estimate the contribution made by the semiconductor surface and the space charge region to the generation current j_g.

When $N_t \ll N_d$ holds (where N_t and N_d are the concentrations of deep-level centers and dopant, respectively), the additional formation of the inversion layer takes place considerably more slowly than the relaxation of the population of deep-level centers.[6] Thus, we can assume that these two processes take place successively rather than simultaneously. When the space-charge region contains identical deep-level centers, the time dependence of the capacitance $C(t)$ during the additional formation of the inversion layer is described by (see Ref. 7, Appendix 1):

$$\frac{q\varepsilon N_d C_i}{C^3(t)}\left[\frac{dC(t)}{dt}\right]=j_g=j_{\mathrm{gs}}+\frac{qN_t}{\tau_{\mathrm{th}}}[h(t)-h_{\mathrm{st}}], \tag{1}$$

where q is the electron charge, ε is the permittivity of the semiconductor, C_i is the capacitance of the insulator, j_{gs} is the generation current at the surface, τ_{th} is the thermal emission time, and $h(t)$ and h_{st} are the thickness of the space charge region and its steady-state value, respectively. The second term on the right-hand side of Eq. (1) is the generation current in the space charge region j_{gdl}. The values of the capacitance and the currents are given per unit area. The dependence of C and h on t is not shown below.

Expression (1) is a generalization of the Zerbst method[8] for the case when the level of the majority generation center is not situated at the center of the band gap. A theoretical analysis[9] shows that the expression for j_{gdl} is valid for $h-h_{\mathrm{st}} \gg L_D$, where $L_D=\sqrt{\varepsilon\kappa T/q^2 N_d}$ is the Debye length, κ is the Boltzmann constant, and T is the temperature.

 © 1999 American Institute of Physics

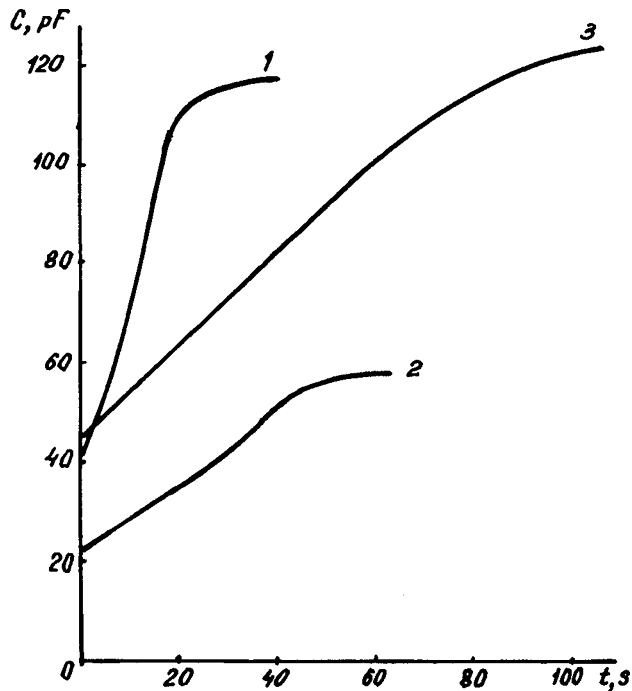

FIG. 1. Time dependence of the capacitance $C(t)$ after switching from -50 to -70 V, $T=253$ K: *1* — group 1, $C_0=44$ pF, $C_{st}=118.3$ pF, $t_{rel}=20.5$ s; *2* — group 2, $C_0=24$ pF, $C_{st}=59.3$ pF, $t_{rel}=47$ s; *3* — group 3, $C_0=46$ pF, $C_{st}=125$ pF, $t_{rel}=82$ s.

At the initial stage of the transition process, the inequality $j_{gdl} \gg j_{gs}$ is usually satisfied so that j_{gs} can be approximated by a constant component.

Expression (1) is then a straight line when plotted in terms of the coordinates $(q\varepsilon N_d C_i/C^3)(dC/dt)$ versus $h-h_{st}$; the slope of this line is qN_t/τ_{th}, and it intersects the y axis at j_{gs}.

In the presence of a concentration profile of deep-level centers $N_t(x)=N_{to}\cdot f(x)$ (where N_{to} is the value of N_t for the initial thickness of the space charge region after switching), $N_t(h-h_{st})$ in Eq. (1) is replaced by

$$N_{to}\int_{h_{st}}^{h} f(x)dx,$$

and then the derivative of (1) with respect to h is $qN_{to} \times f(h)\tau_{th}=qN_t(h)/\tau_{th}$.

RESULTS OF MEASUREMENTS AND DISCUSSION

These results are averaged over the surface of the MIS structures, since the diameter of the MIS structures is much greater than the distance between the bands. Figure 1 gives $C(t)$ for the three groups of samples after switching from $V=-50$ V (strong inversion) to $V=-70$ V ($T=253$ K). These curves were used to determine the time t_{rel} taken for the capacitance to increase from its initial value C_0 to $C_0+0.9(C_{st}-C_0)$, where C_{st} is the steady-state capacitance. A comparison of these curves reveals that group 1 samples (without a regular relief) have the lowest value of t_{rel} (i.e., the highest concentration of deep-level centers), while group 3 samples with a regular relief on the working surface have the highest value of t_{rel}. Thus, a regular relief is an effective getter. When the regular relief is applied to the back of the wafer (group 2), gettering takes place via both surfaces. A comparison of the curves $C(t)$ for groups 1, 2, and 3 also indicates that the regular relief getters over the entire thickness of the wafer (300 μm), although the gettering becomes weaker with thickness.

Figure 2 gives the generation current $j_g=j_{gs}-j_{gdl}$ as a function of the thickness of the space charge region for the same samples after the same switching processes. These curves were calculated from Eq. (1) using the experimental dependence $C(t)$. For these samples at $T=253$ K we have $L_d\approx 0.2$ μm. Thus, the dependence of j_{gdl} on $h-h_{st}$ is valid for $h-h_{st}>1.0-1.5$ μm. The highest generation current

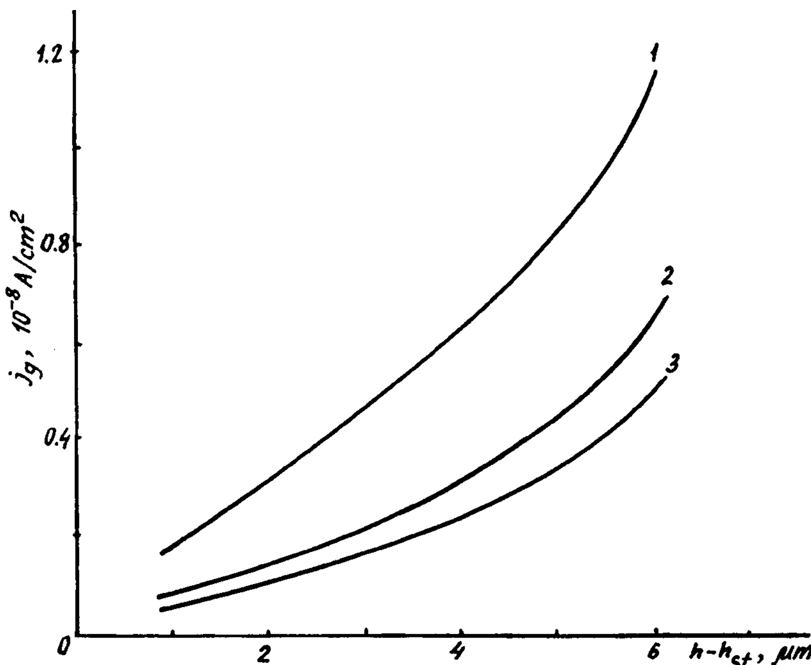

FIG. 2. Generation current versus thickness of space charge region after the same switching process: *1* — group 1, *2* — group 2, and *3* — group 3.

(and the highest concentration of deep-level centers) was obtained for samples without a regular relief and the lowest was obtained for those with a regular relief on the working surface, with an intermediate current being obtained for those samples with a regular relief on the back of the wafer. For all three groups of samples the derivative dj_g/dh increases with increasing h, i.e., the concentration of deep-level centers increases from the working surface toward the inside of the wafer. A comparison of the dependence of j_g on $h-h_{st}$ confirms the reasoning put forward earlier that a silicon–silicon-dioxide interface without a regular relief is also a getter, albeit a weaker one than an interface with a regular relief. It can be seen from the dependence of j_g on $h-h_{st}$ that the inequality $j_{gdl} \gg j_{gs}$ is satisfied at the beginning of the additional formation of the inversion layer (for the highest values of $h-h_{st}$). This result confirms the reasoning put forward above.

Our investigations have shown that a regular relief at a silicon–silicon-dioxide interface is an effective getter at depths of several hundred micron. Optimizing the parameters of the regular relief is a problem for further study.

This work was supported financially by the Russian Fund for Fundamental Research, Grant No. 98-02-18250.

[1] J. S. Kang and D. K. Schroder, J. Appl. Phys. **65**, 2974 (1989).
[2] E. D. Kim, S. C. Kim, J. M. Park, I. V. Grekhov *et al.*, J. Electrochem. Soc. **144**, 622 (1997).
[3] I. V. Grekhov, L. S. Berman, L. S. Kostina *et al.*, Pis'ma Zh. Tekh. Fiz. **22**(23), 14 (1996) [Tech. Phys. Lett. **22**, 956 (1996)].
[4] L. S. Berman, K. P. Abdurakhmanov, S. I. Vlasov *et al.*, Izv. Akad. Nauk Uz. SSR. Ser. Fiz-Mat. Nauk No. 5, 55 (1980).
[5] L. S. Berman and S. I. Vlasov, Mikroélektronika **18**, 374 (1989).
[6] C. T. Sah and H. S. Fu, Phys. Status Solidi A **11**, 297 (1972).
[7] L. S. Berman and A. A. Lebedev, *Capacitive Spectroscopy of Deep Centers in Semiconductors* [in Russian], Nauka, Leningrad (1981), 176 pp.
[8] M. Zerbst, Z. Angew. Phys. **22**, 30 (1996).
[9] A. K. Zakharow and I. G. Neizvestni, Phys. Status Solidi A **30**, 419 (1975).

Translated by R. M. Durham

Dynamic structural transition

G. E. Skvortsov

St. Petersburg State University

(Submitted August 3, 1998)
Pis'ma Zh. Tekh. Fiz. **25**, 81–86 (January 12, 1999)

The phenomenon of dynamic structural transition is discussed. Its main characteristics and dependences are noted together with various effects and applications. © *1999 American Institute of Physics.* [S1063-7850(99)01401-9]

Structural transition is the main form of qualitative change in systems exposed to various influences. The phenomenon of structural transition was analyzed in terms of the laws governing nonequilibrium processes[1,2] for conditions of weak dynamism in Refs. 3 and 4. Of particular interest are dynamic structural transitions demonstrated by an extremely wide range of different structures. Many of these may form or already do forming the basis of effective technologies (such as high-temperature superconductors and nanostructures, photosynthesizing metal complexes, and so on).

Nonequilibrium transitions have given rise to numerous investigations based on the synergetic approach[5] and impressive results have been obtained. However, no general picture of the phenomenon of dynamic structural transition has yet emerged and many relevant problems remained unanswered.

The present paper examines the general laws governing dynamic structural transition and discusses various effects involving dynamic structural transition and their applications.

1. We shall characterize structural transition by supplementing the indicators and properties given in Ref. 3 to allow for nonequilibrium.

1.1. The structure-kinetic elements of the structural transition process are flucons which acquire increasing activity as the action increases.

If there is an adequate flux (input or output) of energy or another resource, the fluctons concentrate the resource, are suitably transformed, and then deactivate abruptly. Having in mind the activation property, we shall describe the fluctons of dynamic structural transition as ''axions.'' Examples of axions include growing clusters, transition complexes in chemical reactions, combustion centers, and dilatons.[6]

These three stages of axion conversion are responsible for three stages of structural transition which are observed in some particular form for different transitions.[7–9] In general, dynamic structural transitions can have more than three stages; for example, six stages were observed during the combustion of titanium in nitrogen.[10]

1.2. The determining classification characteristics of structural transitions were given in Ref. 3. The corresponding degrees of nonequilibrium have the form

$$A_{12}=\left|\frac{a_{n2}-a_{n1}}{a_{n1}}\right|,\quad E=\left|\frac{e-e_0}{\mathcal{E}_s}\right|,\quad P=\left|\frac{\dot{e}-\dot{e}_0}{\dot{\mathcal{E}}_s}\right|,$$

$$\mathrm{res}=\left[1+k_n^{\pm}\left|\frac{a_n-a_{nc}}{a_{nc}}\right|^{\gamma\pm}\right]^{-1}; \tag{1}$$

$$H=\tau_s|\partial_t \ln A|,\quad L=\lambda_s|\partial_x \ln A|, \tag{2}$$

where $a_{n1,2}$ are the values of the determining quantities at the boundary points of the structural transition, e is the specific energy of implementation of the transition, e_0 is the quasi-equilibrium value, $\mathcal{E}_s$ is the average internal energy of a flucton, $\dot{e}$, $\dot{e}_0$, and $\dot{\mathcal{E}}_s$ are the corresponding powers, a_{nc} are the values at the boundary point of the transition stage, and τ_s, and λ_s are the characteristic average time and flucton size.

1.3. Structural transitions whose results depend strongly on the values of P, H, and L may be regarded as dynamic; experience shows that their values should exceed 0.2 for this to apply.

The dependence of the boundaries and results of the structural transition on the velocity H and the scale ratio L has been demonstrated for different types of transitions: martensitic transformations,[11] premelting,[8] detonation,[12], vitrification,[13] and anomalous relaxation.[14]

An increase in the rate usually increases the boundary of the structural transition g_c, which may be reflected by the simple relationships

$$(g_c-g_{co})/\tau_s=\partial_t g_c,\quad \tau_s=\tau_s(g,s), \tag{3}$$

$$g_s\frac{\partial F}{\partial g}=k_F(F_c-F_{co}),\quad F=F(g,\Pi), \tag{4}$$

where ∂_{co} and F_{co} are the boundary values at low velocity, and τ_s is the axion transformation time.

1.4. An increase in the departure from equilibrium reveals the three-level nature of the dynamic structural transition. The micro-, meso- and macrolevels of flucton evolution are consistent with their energy stages and are related to the stages of dynamic structural transition. For instance, the anomalous relaxation in a shock wave considered as a dynamic structural transition takes place in the sequence macro, micro, meso, macro, which corresponds to activation, transformation, and deactivation.

1.5. An important characteristic of structural transition is the relation between the direct and reverse transitions (a direct transition corresponds to energy input and a reverse transition corresponds to energy output).

 © 1999 American Institute of Physics

The quasi-equilibrium Clausius–Clapeyron relations and the Maxwell rule cease to hold as the nonequilibrium increases and the direct and reverse transitions become increasingly asymmetric. The qualitative relation between them can be identified by using the law governing the change in the number of degrees of freedom for a structural transition (see below).

2. We shall indicate the main laws governing dynamic structural transition and some of their consequences.

2.1. All the laws of action[1–3] hold completely for the structural transition process.

The quality boundaries are the measures of action $g_{1,2}$ corresponding to the beginning and end of the structural transition[3] and also the point of inflection $g_3 \approx (g_1+g_2)/2$, which corresponds to the axion transformation stage.

The law of abnormality[1] for this boundary will be found relative to the first derivative of the determining quantity. The law of alternating nonequilibrium[2] is observed as an oscillatory regime near g_1 (Refs. 7 and 15).

2.2. Following Section 1.1, we can assume that a law of energy transformation applies to dynamic structural transition.

This law states that the transformation of fluctons in a dynamic structural transition takes place in three stages; the first two involve activation and the third involves deactivation.

Activation includes the localization and absorption of energy and is accompanied by flucton growth. The accumulation of energy includes the deposited energy, released structural energy, and also the external field energy.

Since we know that broadly speaking, this external field energy is orders of magnitude higher than the free energy of the mass form of a material, there is some justification for the observation of excess energy in processes including dynamic structural transition. An example may be a special regime for the electrolysis of water.[16]

It may be hypothesized that the sources of the Chizhevskiĭ phenomenon are of this type, i.e., the influence of space on living objects. It is sufficient to bear in mind the structural transition nature of life processes.

2.3. One of the main laws governing the structural transition process is an abrupt increase in the number of degrees of freedom during structural transition and an ultimate increase or decrease in these degrees of freedom accompanying the input or output of energy.

This dependence explains the substantial increase in specific heat, sound damping, and dielectric losses, increase and decrease in electrical conductivity, reduction in the velocity of sound, and so on during and corresponding changes in these parameters at the end of a direct or reverse structural transition.

The change in the number of degrees of freedom Δn_f can be determined by using a proportional quantity, i.e., the change in the velocity of sound v_s

$$\frac{\Delta n_f}{n_f} = k\frac{\Delta v_s}{v_s} \approx \frac{k}{v_s}\frac{\partial v_s}{\partial g}\Delta g. \tag{5}$$

Expressing v_s in terms of the equation of state, we obtain a structural transition criterion similar to the gasdynamic criterion for anomalous relaxation.[14]

From the standpoint of this dependence, it is natural to use a dynamic-structural-transition erosion discharge[15] for efficient absorption of the energy of high-power electrical pulses (S. E. Emelin).

2.4. An important dependence of dynamic structural transition is the asymmetry of the direct and reverse transitions. This asymmetry increases as a function of the departuer from equilibrium and can be quantified by the relative area of the hysteresis loop.

For example, for an isothermal vapor (1), (2)–liquid (3), (4)–vapor (1) cycle using the van der Waals equation of state, the asymmetry as is approximately given by

$$as \approx (V_1 - V_4)(p_2 - p_1)/p_2 V_1, \quad p = p_{BB}(V), \tag{6}$$

from Eqs. (3) and (4) we find $p_2 > p_{\rm M} > p_1$, $V_2 < V_{\rm M1}$, $V_4 > V_{\rm M2}$; $p_{\rm M}$ and $V_{\rm M1,2}$ are the values ascribed to the Maxwell rule.

The asymmetry of a dynamic structural transition has very diverse manifestations: for combustion, fracture, and so on, obviously no reverse structural transitions take place; for martensitic transitions plasticity and strong acoustic emission are observed during cooling, while a shape memory effect and weaker emission are observed during heating.[11,17]

Note that sufficiently far from equilibrium and with suitable implementation, dynamic structural transition cycles offer the possibility of efficiently converting and producing energy. An original method of this type was proposed by Skornyakov.[18]

2.5. When two or more structural transition factors are acting, a ''radical'' law is observed which is responsible for the instability characteristic of structural transition.

This law contains two statements which refer to two cases: small actions compared with the main action and structural transition factors of similar magnitude. In the first case, the structural transition process and its result vary significantly (predictably). In the second case, the result of the dynamic structural transition differs radically from the ''components'' of the structural transition and can be predicted with some particular probability.

Examples of ''weak radicality'' include effects of the influence of noise on structural transition, chemical catalysis, intensification and quenching of flames by an electric field, the influence of impurities on the anomalous relaxation phenomenon, and elimination of fluctons by a field.[19] Studies of two- and three-factor structural transitions are extremely promising (although the ''indeterminacy of the result'' must be overcome). Existing experiments confirm this.

Two observations may be made in conclusion. The laws described here have numerous productive consequences and applications. Their applications to the aforementioned dynamic structural transition processes reveal new aspects. By using these laws, it will be possible to form a very general model of dynamic structural transition.

[1] G. E. Skvortsov, Pis'ma Zh. Tekh. Fiz. **23**(7), 23 (1997) [Tech. Phys. Lett. **23**, 261 (1997)].
[2] G. E. Skvortsov, Pis'ma Zh. Tekh. Fiz. **23**(10), 17 (1997) [Tech. Phys. Lett. **23**, 383 (1997)].
[3] G. E. Skvortsov, Pis'ma Zh. Tekh. Fiz. **24**(3), 80 (1998) [Tech. Phys. Lett. **24**, 80 (1998)].
[4] G. E. Skvortsov, Pis'ma Zh. Tekh. Fiz. **24**(19), 7 (1998) [Tech. Phys. Lett. **24**, 749 (1998)].
[5] G. Nicolis and I. Prigogine, *Self-Organization in Nonequilibrium Systems* (Wiley, New York, 1977; Mir, Moscow, 1979, 512 pp.).
[6] V. I. Vettegren', I. I. Novak, A. T. Tokhmetov, S. A. Poretskiĭ, and Yu. I. Yakimenko, in *Nonlinear Effects in Fracture Kinetics* [in Russian], Leningrad, (1988), p. 106.
[7] A. P. Smirnov, in *Systems of Singular Temperature Points of Solids* [in Russian], Nauka, Moscow (1986), p. 210.
[8] L. A. Bityutskaya and E. S. Mashkina, Pis'ma Zh. Tekh. Fiz. **22**(21), 1 (1996) [Tech. Phys. Lett. **22**, 863 (1996)].
[9] L. B. Zuev, V. I. Danilov, and V. V. Gorbatenko, Zh. Tekh. Fiz. **65**(5), 91 (1995) [Tech. Phys. **40**, 456 (1995)].
[10] I. O. Khomenko, A. S. Mukas'yan, and A. G. Merzhanov, Dokl. Akad. Nauk SSSR **326**, 673 (1992).
[11] V. A. Likhachev, S. L. Kuz'min, and Z. P. Kamentseva, *Shape Memory Effect* [in Russian], Leningrad (1987) 216 pp.
[12] S. A. Balankin, A. A. Lyubomudrov, and I. G. Sevryukov, Zh. Tekh. Fiz. **59**(12), 102 (1989) [Sov. Phys. Tech. Phys. **34**, 1431 (1989)].
[13] R. N. Siney, in T. Riste and D. Sherrington (Eds.), *Phase Transitions and Relaxation in Systems with Competing Energy Scales*, Kluwer Academic, Boston (1993), p. 259.
[14] G. I. Mishin, A. P. Bedin, N. I. Yushchenkova, G. E. Skvortsov, and A. P. Ryazin, Zh. Tekh. Fiz. **51**, 2315 (1981) [Sov. Phys. Tech. Phys. **26**, 1361 (1981)].
[15] S. E. Emelin, A. L. Pirozerskiĭ, V. S. Semenov, and G. E. Skvortsov, Pis'ma Zh. Tekh. Fiz. **23**(19), 54 (1997) [Tech. Phys. Lett. **23**, 758 (1997)].
[16] B. F. Lyakhov, Zh. Fiz. Khim. **72**, 765 (1998).
[17] V. A. Plotnikov, Pis'ma Zh. Tekh. Fiz. **24**(1), 31 (1998) [Tech. Phys. Lett. **24**, 14 (1998)].
[18] G. V. Skornyakov, Zh. Tekh. Fiz. **65**(1), 35 (1995) [Tech. Phys. **40**, 18 (1995)].
[19] Ya. B. Zel'dovich and A. S. Mikhaĭlov, JETP Lett. **46**, 83 (1987).

Translated by R. M. Durham

Efficiency of cooling of laser diode arrays in contact with a porous permeable wall

V. V. Apollonov, S. I. Derzhavin, V. V. Kuz'minov, D. A. Mashkovskiĭ, V. N. Timoshkin, and V. A. Filonenko

Institute of General Physics, Russian Academy of Sciences, Moscow
(Submitted August 18, 1998)
Pis'ma Zh. Tekh. Fiz. **25**, 87–94 (January 12, 1999)

It has been suggested that heat transfer from a porous permeable material using a liquid coolant may be used to improve heat exchange in powerful laser-diode emitters [V. V. Apollonov, A. I. Barchukov, A. M. Prokhorov *et al.*, Metal Laser Mirror with a Cooled Optical Surface, FIAN Report (1977); V. V. Apollonov, P. I. Bystrov, and V. F. Goncharov, Sov. J. Quantum Electron. **9**, 1499 (1979)]. An analysis of typical values of the thermal loads and their dependence on the parameters of the material and the liquid using a one-dimensional model of steady-state heat exchange shows that thermal fluxes in excess of 1 kW/cm^2 can be removed. © *1999 American Institute of Physics.*
[S1063-7850(99)01501-3]

1. As a result of the critical temperature dependence of the radiation characteristics of laser diode arrays, the cw lasing power can only be increased by improving the heat transfer away from the active region.[3,4] The problem involves removing appreciable thermal fluxes (>1 kW/cm^2) with a low temperature difference (~ 10 K). Here we analyze the possibility of solving this problem by means of heat transfer across the surface of a layer of an open porous structure with a matrix made of a highly heat-conducting material (porometal) washed with a liquid coolant. The high efficiency of this method produced by the intensive exchange absorption of heat was demonstrated earlier for the cooling of power optics elements but with a larger temperature difference (≈ 100 K) (Refs. 1 and 2).

We shall analyze the case in which the thermal conductivity κ_p of the matrix is much higher than that of the liquid coolant, κ_1, so that we can assume that the entire heat flux across the contact surface is transferred to the bulk of the porous layer (Fig. 1) only via the matrix.[5,6] The latter is described using the conventional approximation of an effective continuous homogeneous medium having the thermal conductivity $\kappa_p = \kappa_p^{(0)} f(\Pi)$, where $\kappa_p^{(0)}$ is the thermal conductivity of the matrix material in the compact state, $f(\Pi)$ is a function of the average porosity of the medium Π whose form depends on the structure of the matrix, $f(\Pi) < 1$ (Refs. 7 and 8).

Calculations of the heat exchange in a laser diode array (cw radiation) and a cooling layer of porometal which together form a multilayer medium (Fig. 1) were made using a one-dimensional steady-state model:

$$\kappa_i \partial_x^2 T_i + q_i = 0, \quad \partial_x^2 T_p - \Lambda^{-2} T_p = 0,$$

$$\partial_x^2 T_j = 0, \quad \Lambda^2 = \kappa_p / \alpha_V,$$

where T_i, T_p, and T_j are the temperatures in the layers of the array and the electrodes, the temperature of the matrix in the porous layer, and the temperature in all other layers, respectively, q_i is the density of the bulk sources of Joule heat, $\alpha\nu$ is the bulk coefficient of heat transfer, which characterizes the rate of heat exchange between the matrix and the liquid, and Λ is the characteristic depth of heat absorption in the porous layer. The temperatures are measured from the coolant temperature on entry to the porous layer. The active layer is considered to be a planar heat source at the interface between layers B and I with a constant density of the released heat flux Q. The conditions at the boundary $x=0$ are then written as

$$T_B^{(a)} = T_I^{(a)}, \quad \kappa_B^{(a)} \partial_x T_B^{(a)} = \kappa_I^{(a)} \partial_x T_I^{(a)} + Q,$$

where the index (a) indicates the layers of B and I directly adjacent to the active layer. The coupling conditions at all the other internal boundaries are

$$T_n = T_{n+1}, \quad \kappa_n \partial_x T_n = \kappa_{n+1} \partial_x T_{n+1},$$

where κ_n is the thermal conductivity of the layers. At the external surfaces, which are assumed to be thermally insulated, we have

$$x = -l_0, \quad \partial_x T_B^{\text{ex}} = 0, \quad x = l_3, \quad \partial_x T_I = 0,$$

where $T_B^{(\text{ex})}$ is the cathode temperature (the upper layer of B).

In the approximation $q_i = 0$ (which is permissible for pump currents up to 100 A, as has been shown by estimates for a standard AlGaAs array used experimentally[9,10]) the density of the heat flux removed from the laser diode array by the porous layer is Q and is related to the temperature in the active layer T_a by

$$\frac{T_a}{Q} = \sum_{(I)} \frac{l_i}{\kappa_i} + \frac{\Lambda}{\kappa_p} \coth\left(\frac{L_p}{\Lambda}\right), \quad L_p = l_2 - l_1, \tag{1}$$

where summation in the first term is performed over all layers forming part of layer I. Generalizing this model to the case of pulse-periodic operation of a laser diode array, we can easily show that for rectangular pulses of duration τ_p and inverse duty cycle ν, the average temperature is $\langle T_a \rangle = \nu \tau_p T_a$.

 © 1999 American Institute of Physics

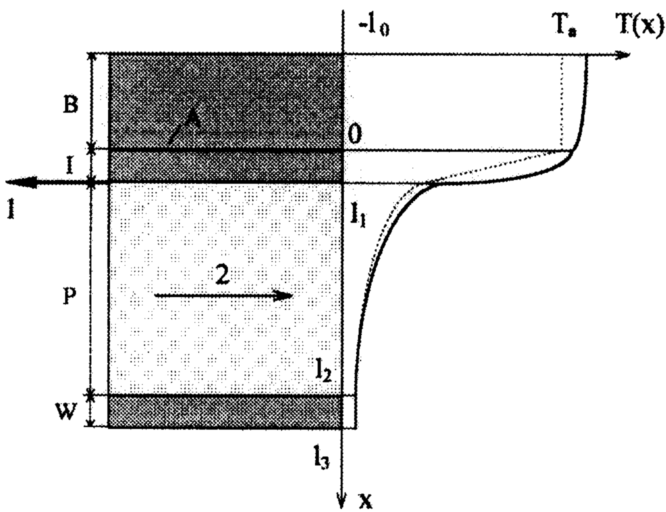

FIG. 1. Schematic to calculate the temperature distribution. Layers: *B* — film cathode and multilayer component of *n*-type array; *A* — active layer, *I* — multilayer component of *p*-type array, film anode, solder layer, *P* — cooled porous layer, *W* — enclosing wall. Directions: *1* — radiation out, *2* — liquid flow. The solid line on the $T(x)$ graph gives the accurate solution of the model and the dashed line corresponds to the approximation $q_1=0$.

2. The limiting heat fluxes Q^* which can be removed by the porous layer are determined from Eq. (1) for $T_a=T_a^*$, i.e., the permissible overheating of the active layer (the corresponding radiation power is $Q^*\xi/(1-\xi)$, where ξ is the efficiency of the array). The calculations were made for an AlGaAs laser diode array[9,10] for which $T_a^*=15\,\mathrm{K}$ (room-temperature coolant). The following values were used for the terms of the sum on the right-hand side of Eq. (1): *p* layer of array — $l_1=1.5\,\mu\mathrm{m}$, $\kappa_1=0.46\,\mathrm{W/cm\cdot K}$; gold anode — $l_2=10\,\mu\mathrm{m}$, $\kappa_2=3.17\,\mathrm{W/cm\cdot K}$; indium solder — $l_3=5\,\mu\mathrm{m}$, $\kappa_3=0.82\,\mathrm{W/cm\cdot K}$.

The volume coefficient of heat transfer α_v that regulates the value of Q^* is calculated using the Nusselt number Nu, which depends very strongly on the structure of the porous material and the type of structure-forming elements. Calculations of $Q^*(d,\Pi)$ were made for a large sample of empirical expressions for Nu taken from those given in Refs. 7 and 8. Typical data are plotted in Fig. 2 and correspond to the generalized relation Nu = 0.004 Pe proposed in Ref. 7, where Pe is the Peclet number. This is an extrapolation of a considerable number of particular relationships for Nu and can be applied within permissible error when $0.2<\Pi<0.65$. It corresponds to $\alpha_v=\kappa_1\mathrm{Nu}(a/b)^2$, $\mathrm{Pe}=\mathrm{Vb}/(\chi a)$, where χ is the thermal diffusivity of the liquid, *V* is its rate of filtration through the porous layer, and *a* and *b* are the viscous and inertial coefficients of the Darcy–Reynolds–Forschheimer (DRF) equation,[7,8] which we used in the lin-

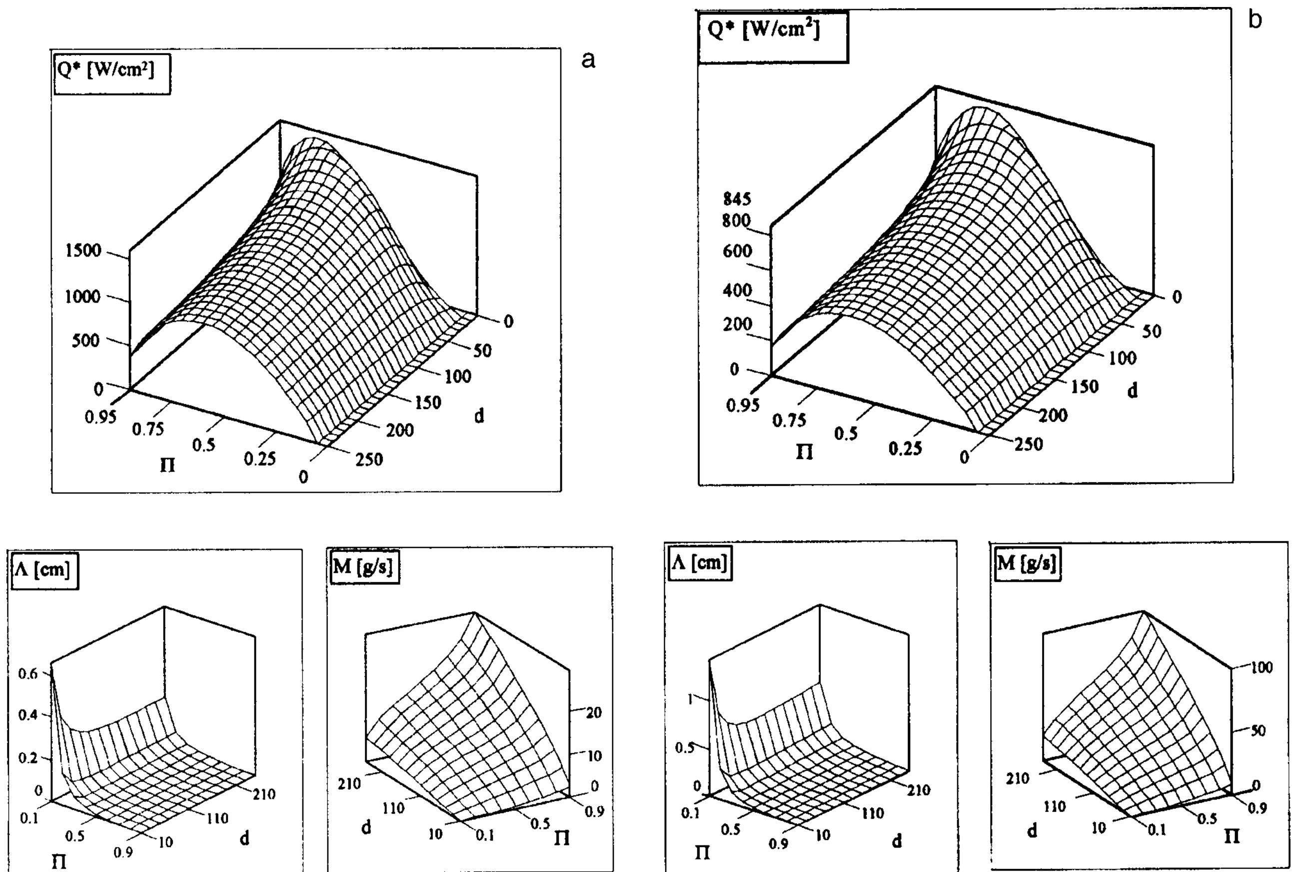

FIG. 2. Limiting heat fluxes Q^* removed from the active layer by a layer of porometal, characteristic heat absorption length Λ, and coolant mass flow *M* as a function of wire diameter $d\,[\mu\mathrm{m}]$ and average porosity Π for a — water, b — eutectic Na–K–Cs mixture.

earized form $p/H = a\eta V + b\rho V^2$, where p is the downstream pressure drop in a section of length H, and η and ρ are the dynamic viscosity and the liquid density. In order to achieve maximum uniformity in the heating of the array and minimize the influence of heating of the liquid, the liquid flux should be directed perpendicular to the longitudinal axis of the array so that H is equal to the array width of 0.5 mm and the typical value of 1 atm was used for p. The following values were taken for the coefficients of the DRF equation[8]

$$a = 6\times 10^9 (1-\Pi)^2 \Pi^{-3} d^{-2} \quad [\mathrm{cm}^{-2}],$$

$$b = 9.23\times 10^3 (1-\Pi)\Pi^{-3.73} d^{-1} \quad [\mathrm{cm}^{-1}], \quad [d] = \mu\mathrm{m},$$

which refer to wire porous structures, which are considered to be the most effective type of matrix for removing intensive heat fluxes, where d is the average diameter of the wire. The matrix was assumed to be made of copper and the form $f(\Pi) = (1-\Pi)/(1+\Pi)$ was used for the thermal conductivity.[8] The values of $Q^*(d,\Pi)$ in Fig. 2 were calculated for $L_p = 3\Lambda$, which minimize the heat resistance of the porous layer ($\coth(L_p/\Lambda)\approx 1$ for $L_p/\Lambda \geqslant 3$). Also plotted in Fig. 2 are the dependence $\Lambda(d,\Pi)$ corresponding to these parameters and the liquid mass flow $M(d,\Pi) = 3\rho V\Lambda$, calculated using the DRF equation (for an array length of 1 cm).

The coolant was taken to be water (high specific heat; Fig. 2a) and an Na–K–Cs liquid-metal eutectic mixture (high thermal conductivity) (Fig. 2b) whose characteristics were taken from Ref. 11. The higher values of Q^* for water can be explained by noting that χ is almost ten times lower than that for Na–K–Cs and the selected Nusselt number is $\mathrm{Nu}\sim\mathrm{Pe}\sim\chi^{-1}$. When highly porous materials with $0.7<\Pi<0.9$ are used,[6,12] the situation changes and the higher values of Q^* are obtained for the eutectic mixture. For example, for Nu from Ref. 12 the maximum heat fluxes Q^* calculated for the values given above are $\approx 1.1\ \mathrm{kW/cm^2}$ for the eutectic mixture and $0.92\ \mathrm{kW/cm^2}$ for water.

The calculated results broadly show that heat exchange may be intensified primarily by optimizing the structure of the porometal for the particular coolant. This is based on creating conditions for increased turbulence of the liquid flow in the pores. The highest values of α_v correspond to $\Pi = 0.5-0.7$ for $d<(50-70)\ \mu$m, which shows good agreement with the results of other studies.[1,2] To a lesser extent, the limiting fluxes depend on increasing the pressure: for example, for the curves plotted in Fig. 2 the maximum heat flux Q^* is doubled when p is increased ten times.

3. As a result, we can conclude that heat exchange of a laser diode array with a porometal layer can provide effective cooling of the active region under cw lasing conditions with intensive heat fluxes in excess of $1\ \mathrm{kW/cm^2}$. The fact that these values were obtained using a one-dimensional model implies that these fluxes can be removed by a porous heat exchanger commensurate with the array in the plane of contact. Combined with the low values of Λ, this may provide the basis for developing compact microheat exchangers.

The use of these heat exchangers in laser diode arrays[13] could substantially increase the packing density of the arrays and thus the average flux density of the radiation. Bilateral heat transfer from the thick low-heat-conducting n-layer of the array to B, which separates the wall $x = -l_0$ from the active layer, cannot substantially improve the efficiency of this cooling method. An appreciable effect may be achieved either by precooling the coolant or by using a coolant with a low boiling point, either under normal conditions or under low-pressure conditions achieved by creating a negative pressure at the channel exit (vapotron effect).[14]

[1] V. V. Apollonov, A. I. Barchukov, A. M. Prokhorov *et al.*, *Metal Laser Mirror with a Cooled Optical Surface* [in Russian], FIAN Report (1977).
[2] V. V. Apollonov, P. I. Bystrov, and V. F. Goncharov, Kvantovaya Élektron. (Moscow) **6**, 2533 (1979) [Sov. J. Quantum Electron. **9**, 1499 (1979)].
[3] N. C. Gasey, Jr. and M. B. Panise, *Heterostructure Lasers*, Part A (Academic Press, New York, 1978; Vol. 1, Mir, Moscow, 1981).
[4] I. S. Baĭkov and V. V. Bezotosnyĭ, Prikl. Fiz. No. 2, 3 (1995).
[5] A. A. Plakseev and V. V. Kharitonov, Inzh.-Fiz. Zh. **56**, 36 (1989).
[6] V. V. Kharitonov, *Heat Physics of Laser Mirrors* [in Russian], Moscow Engineering Physics Institute Press, Moscow (1993), 152 pp.
[7] V. M. Polyaev, V. A. Maĭorov, and L. L. Vasil'ev, *Hydrodynamics and Heat Exchange in Porous Structural Elements of Aircraft* [in Russian], Mashinostroenie, Moscow (1988), 168 pp.
[8] *Porous Permeable Materials*, edited by S. V. Belov [in Russian], Nauka, Moscow (1987), 340 pp.
[9] V. V. Bezotosnyĭ, Yu. P. Koval', N. V. Markova *et al.*, Kvant. Élektron. (Moscow) **22**(2), 101 (1995).
[10] V. V. Apollonov, S. I. Derzhavin, V. V. Kuz'minov *et al.*, Kvant. Élektron. (Moscow) **24**, 869 (1997).
[11] P. I. Bystrov, D. N. Kagan, G. A. Krechetova *et al.*, *Liquid-Metal Coolants for Heat Pipes and Power Installations* [in Russian], Nauka, Moscow (1988), 263 pp.
[12] Yu. F. Gortyshov, G. B. Murav'ev, and I. N. Nadyrov, Inzh.-Fiz. Zh. **53**(3), 357 (1987).
[13] D. Mundinger, R. Beach, W. J. Benett *et al.*, Appl. Phys. Lett. **53**, 1030 (1988).
[14] V. V. Apollonov, A. I. Barchukov, A. M. Prokhorov *et al.*, *Water-Cooled Mirror Operated as a Hypervapotron* [in Russian], FIAN Report (1977); V. V. Apollonov, A. M. Prokhorov, V. Yu. Khomich, and E. V. Khristyan, Pis'ma Zh. Tekh. Fiz. **4**(4), 433 (1978) [Sov. Tech. Phys. Lett. **4**, 174 (1978)].

Translated by R. M. Durham

New efficient low-pressure gas-discharge source of optical radiation using hydroxyl OH

A. Ya. Vul', S. V. Kidalov, V. M. Milenin, N. A. Timofeev, and M. A. Khodorkovskiĭ

St. Petersburg State University;
A. F. Ioffe Physicotechnical Institute, Russian Academy of Sciences, St. Petersburg;
Russian Scientific Center of Applied Chemistry, St. Petersburg
(Submitted July 24, 1998)
Pis'ma Zh. Tekh. Fiz. **25**, 10–16 (January 12, 1999)

An experimental investigation was made of the possibility of developing a new efficient gas-discharge source of optical radiation based on an OH hydroxyl molecular additive. It is shown that under certain discharge conditions, the luminous efficiency of a positive discharge column in a rare gas–hydroxyl mixture is similar to that of a mercury discharge. The results suggest that it may be possible to develop a new ecologically innocuous source of optical radiation which may in future replace mercury luminescence light sources. © *1999 American Institute of Physics.* [S1063-7850(99)00201-3]

Modern low-pressure gas-discharge sources of optical radiation are based on mixtures of buffer gas and an easily ionized emitting additive.[1] Although the concentration of emitting additive atoms is low compared with the buffer gas, the relatively low excitation and ionization potential of these atoms makes it comparatively easy to create discharge conditions where the emitting properties and the electron energy balance in the positive discharge column are determined by the additive atoms, while the buffer gas atoms are barely excited, are not ionized, and merely determine the particle transport processes in the discharge (except for resonant photons from the low concentration of emitting additive atoms). This means that electrical energy can be converted into radiation with an extremely high efficiency, with most of the energy deposited in the positive discharge column being emitted as resonance radiation from the additive atoms. For example, in mercury and low-pressure sodium luminescence light sources, the resonance radiation of the mercury and sodium atoms accounts for 70–80% of the total energy balance of the positive discharge column.

Examples of these optical radiation sources include mercury luminescence lamps and low-pressure sodium lamps among others. Rare gases (Ar, Ne) are most frequently used as the buffer gas with alkaline-earth elements (Hg, Cd, Zn), alkali metals (Na, K, Rb), and various other metals (Cu, Tl) being used as emitting additives.[1]

The seemingly broad choice of emitting additives is severely limited by additional constraints imposed on the elements forming part of the discharge radiation source. First, it is desirable that the resonance radiation of additive atoms or molecules should lie in the 200–400 nm range. For shorter-wavelength radiation it is difficult to produce an efficient, long-lived, cheap phosphor capable of converting ultraviolet radiation into the visible part of the spectrum. Second, the concentration of emitting additive atoms or molecules should be sufficient to obtain the required radiation brightness at reasonable discharge-envelope temperatures (up to approximately 1000 °C). In addition, the additive should be stable under discharge conditions, it should be neutral to the materials used in the radiation source, and preferably it should also be ecologically innocuous.

Hardly any of the materials currently used as easily ionized additives satisfy this complete set of requirements. One of the constraints most difficult to satisfy is that this additive should be ecologically innocuous.

The aim of the present paper is to investigate the possibility of creating a new efficient source of optical radiation in which OH molecules are used as the emitting additive.[2,3]

Figure 1a gives a simplified level diagram of the OH molecule which shows the main processes which may be responsible for deactivating the levels (only the electronic states are shown and the vibrational–rotational structure is not given). The $^2\Sigma^+(A)$ lower resonance state of the OH molecule with an excitation energy of 4.06 eV gives a 306.4 nm emission band. This radiation can be converted to visible using a phosphor and also used without conversion, since it coincides with the maximum of the absorption band of biological objects for ultraviolet radiation. However, the ionization potential of the OH molecule is 12.1 eV, which is appreciably lower than that of light rare gases (He, Ne, Ar).

We investigated a discharge in He, Ne, Ar, and Xe rare gases with added OH molecules. The rare gas pressure was varied between 3 and 30 Torr and the concentration of the molecular additive was 10^{14}–$10^{16}\,\mathrm{cm}^{-3}$. We used quartz discharge tubes of radius 1 cm and length around 10 cm, and a discharge current of 100–600 mA. The parameters measured were the plasma emission spectrum between 200 and 800 nm for various discharge conditions and plasma compositions, and the power deposited per unit length of the positive discharge column. Comparative experiments were also carried out where different phosphors were excited by a discharge containing OH molecules and by a mercury luminescence lamp to estimate the luminous efficiency of this discharge.

Our investigations revealed that the addition of OH molecules to a rare-gas discharge substantially changes the electrical and optical properties of the plasma. Figure 1b gives the emission spectra of a positive discharge column using a

 © 1999 American Institute of Physics

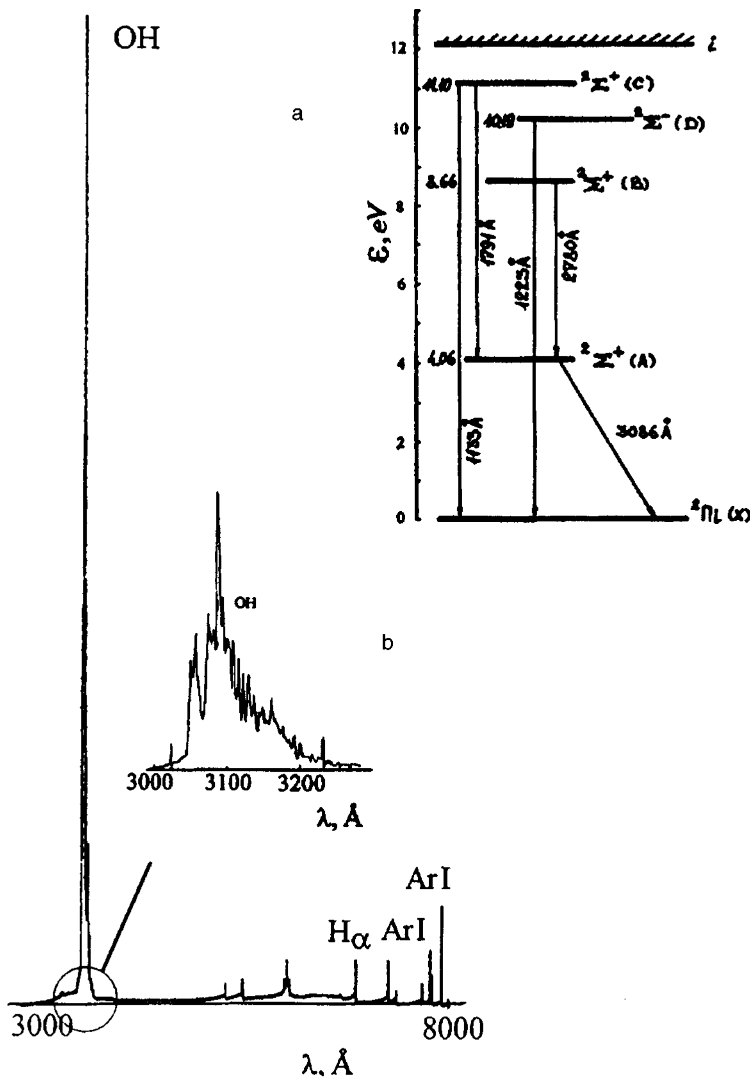

FIG. 1. a — Simplified level diagram of the OH molecule. The arrows indicate the main processes which may cause deactivation of the levels (only the electronic states are shown, not the vibrational–rotational structure); b — emission spectrum of a positive discharge column in a mixture of argon and OH molecules.

mixture of argon and OH molecules. It can be seen that the presence of OH in the discharge almost completely suppresses the rare-gas radiation in this part of the spectrum. Emission of the 306.4 nm OH band is observed at an extremely high intensity. This suggests that most of the energy deposited in the positive discharge column is dissipated in exciting hydroxyl resonance radiation. Similar results were obtained for mixtures of OH with the other rare gases noted above. Note that the spectrum reveals no appreciable emission from atomic hydrogen (by selecting the discharge conditions it was possible to achieve an intensity ratio of the H_α line to the 306.4 nm OH band of the order of 10^{-2}) and absolutely no oxygen emission that could result from the dissociation of water molecules in the discharge and emission from these water molecules themselves.

Figure 2 gives the intensity I of the OH band (306.4 nm), the electrode voltage U, and the luminous efficiency η of a discharge in a hydroxyl–argon mixture, plotted as a function of the discharge current i. These curves are qualitatively similar to those observed in low-pressure mercury luminescence lamps for which the resonance radiation intensity increases linearly with increasing current, the electrode voltage decreases, and the luminous efficiency increases.[4,5] This pro-

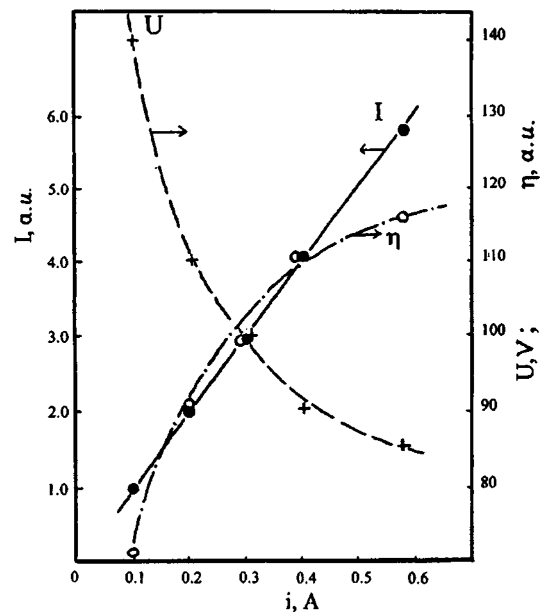

FIG. 2. Intensity I of the 306.4 nm OH band, electrode voltage U, and luminous efficiency η of a hydroxyl–argon discharge as a function of the discharge current i.

vides indirect evidence of the similarity between the processes determining the properties of the plasma in this discharge and the plasma in mercury luminescence lamps.

An estimate of the absolute value of the luminous efficiency for a hydroxyl–rare gas discharge, made using comparative measurements of the radiation intensity of an external phosphor excited by this discharge and by a standard mercury luminescence lamp, showed that under certain discharge conditions, the luminous efficiency of a positive discharge column in a rare-gas–OH mixture is close to that of a mercury discharge.

In order to assess the interaction processes between the discharge products and the walls of the discharge tube, we analyzed the inner surface of the lamp after operation for 100 h. The inner surface was analyzed at five points, at the center of the tube, near the anode and the cathode (dark dusty side), and also directly at the anode and the cathode. We used an ESCA-5400 x-ray photoelectron spectrometer with magnesium radiation. The results of an atomic analysis are plotted in Fig. 3. The dark deposit formed near the electrodes is caused by metals, especially tungsten, sputtered from the electrodes. The metals on the surface of the tube are mainly in the metallic state, the oxide fraction accounting for less than 15–20%. Exceptions to this are barium, which is probably mainly in the oxide form and tungsten near the anode, where the fraction of tungsten oxide reaches 40%. The central part of the tube has the strongest oxygen deficiency relative to SiO_2 stoichiometry, which may indicate that $Si(OH)_4$ compounds are formed at the surface of the quartz tube. Near the anode the oxygen deficiency is negligible.

Preliminary investigations of the effect of OH molecules on various phosphors deposited on the inner surface of the glass discharge tube have shown that the plasma components have no adverse influence on them. However, this aspect together with the interaction between OH molecules and the electrode material requires further investigations.

Thus, these results suggest that it is quite feasible to develop a new ecologically innocuous source of optical radiation which may in future replace mercury luminescence light sources.

The authors are grateful to A. L. Shakhmin for making various measurements.

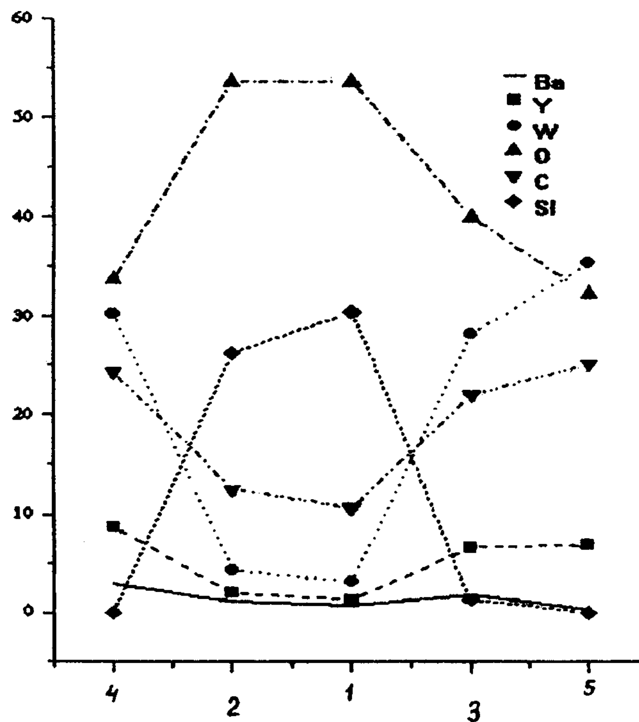

FIG. 3. Results of an atomic analysis of the inner surface of the discharge tube at five points — at the center (*1*), near the anode (*2*) and cathode (*3*) (dark dusty side), and also directly at the anode (*4*) and cathode (*5*); *C* is the concentration.

[1] G. N. Rokhlin, *Discharge Light Sources* [in Russian] Énergoizdat, Moscow (1991), 720 pp.

[2] N. L. Bashlov, A. Ya. Vul', S. V. Kidalov, S. V. Kozyrev, V. M. Milenin, and N. A. Timofeev, Russian Patent No. 2074454 *A Method of Producing Optical Radiation and a Discharge Lamp for this Purpose*, priority date 01.08.95, International Claim Ref. PCT/RU96/00203 (WO97/05646).

[3] V. M. Milenin, N. A. Timofeev, S. V. Kidalov, S. V. Kozyrev, and A. Ya. Vul', in *Proceedings of the International Conference on Phenomena in Ionized Gases*, Toulouse, France, 1997, Vol. III, p. III–56.

[4] J. F. Waymouth and F.-J. Bitter, Appl. Phys. **27**(2), 122 (1956).

[5] V. M. Milenin and N. A. Timofeev, *Plasma of Low-Pressure Gas-Discharge Light Sources* [in Russian], Leningrad University Press, Leningrad (1991), 240 pp.

Translated by R. M. Durham

Influence of viscosity relaxation on the growth rate of the Tonks–Frenkel instability

S. O. Shiryaeva and O. A. Grigor'ev

P. G. Demidov State University, Yaroslavl

(Submitted April 20, 1998)
Pis'ma Zh. Tekh. Fiz. **25**, 1–4 (January 26, 1999)

A numerical analysis of the dispersion equation for the capillary motion of a viscoelastic liquid is used to show that the growth rate of the instability of a charged free liquid surface increases substantially as the characteristic time for the relaxation of viscous stresses and the Tonks–Frenkel parameter increase. This instability is achieved in a bounded range of wave numbers whose width is also determined by the Tonks–Frenkel parameter. © *1999 American Institute of Physics.* [S1063-7850(99)01601-8]

Previous analyses[1–3] of the influence of viscosity relaxation on the laws governing the establishment of capillary motion of a liquid with a charged free surface are mainly qualitative, since they were made either using asymptotic methods or numerical techniques based on identifying qualitative behavior. In this last case, we are talking of methods of nondimensionalizing the dispersion equation prior to making numerical calculations. In the numerical treatments reported in Refs. 1–3 the frequency, growth rates, and damping rates of the capillary motion of a liquid were nondimensionalized either in terms of the frequency of the wave motion in an ideal liquid with a charged free surface or in terms of the characteristic damping rate of the capillary waves. In both cases, the goal was the same—to reduce the number of dimensionless physical parameters characterizing the capillary motion of the liquid in this system.

The variable argument of the unknown complex frequencies was a dimensionless parameter that depends on the wave number, capillary pressure, and electric field pressure at the free surface of the liquid, which themselves depend on the physical characteristics of the liquid, that is to say, the density, capillary constant, surface tension, and coefficient of viscosity, and on the surface electric charge density. This factor has made it difficult for numerical analyses[1–3] to identify the specific dependence of the characteristics of the capillary liquid motion on quantities such as the wave number k and the Tonks–Frenkel parameter W. In the following analysis we shall examine how the wave number k, the Tonks–Frenkel parameter W, and the characteristic time t_0 for relaxation of the viscous stresses in a liquid influence the growth rate of the Tonks–Frenkel instability.

We shall calculate the spectrum of capillary motion in a perfectly conducting viscoelastic liquid of infinite depth, situated in a gravitational field $\mathbf{g}$ and an electrostatic field $\mathbf{E}$ normal to the free surface, which induces a uniformly distributed surface charge with surface density $\varkappa$ at the planar free surface of the liquid. We assume that the liquid has the density ρ, kinematic viscosity ν, and surface tension σ.

Taking the viscosity to be a function obeying the Maxwell formula[4] $\nu=\nu_0/(1-i\omega t_0)$, where ω is the complex frequency, and repeating the reasoning put forward in Refs. 1–3, we can easily obtain the dispersion equation for the capillary motion of a viscoelastic liquid with a charged free surface in the dimensional form[1–3]

$$\left(\omega+\frac{\nu_0 2ik^2}{(1-i\omega t_0)}\right)^2+\frac{4\nu_0^2k^4}{(1-i\omega t_0)^2}\sqrt{1-\frac{i\omega(1-i\omega t_0)}{\nu_0 k^2}}=\omega_0^2;$$

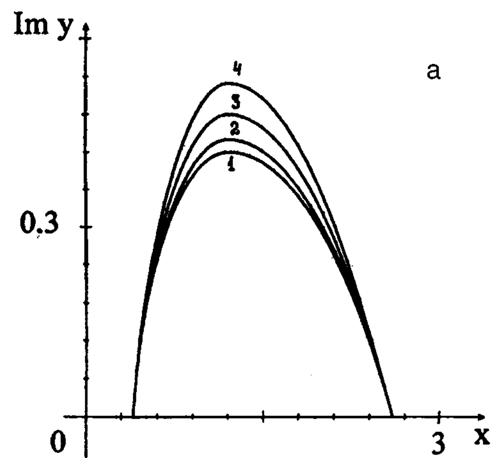

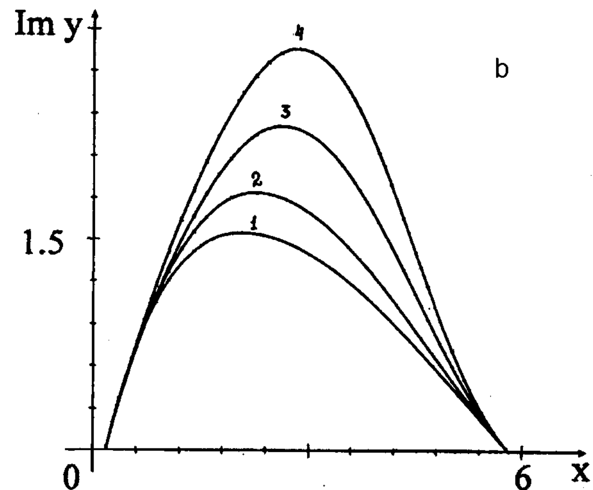

FIG. 1. a — Dependence of the dimensionless instability growth rate of a charged free surface of viscoelastic liquid as a function of the dimensionless wave number calculated for $W=3$, $\beta=1$, and various typical relaxation times for the elastic stresses: *1* — $\tau=0.11$, *2* — $\tau=0.3$, *3* — $\tau=0.6$, *4* — $\tau=1$; b — the same dependence as in Fig. 1a calculated for $W=6$.

 © 1999 American Institute of Physics

$$\omega_0^2=\frac{k}{\rho}(g\rho+\sigma k^2-4\pi\varkappa^2 k).$$

Introducing the dimensionless variables

$$x=ka;\quad a=\sqrt{\sigma/\rho g},\quad y=\frac{\omega a^2}{\nu_0},$$

$$\tau=\frac{t_0\nu_0}{a^2},\quad \beta=\frac{\sigma a}{\rho\nu_0^2},\quad W=\frac{4\pi\varkappa^2 a}{\sigma},$$

we can rewrite the dispersion equation as

$$[y(1-iy\tau)+2ix^2]^2+4x^4\sqrt{1-\frac{iy(1-iy\tau)}{x^2}}=\beta x[1+x^2-Wx](1-iy\tau)^2. \quad (1)$$

Unlike the methods of nondimensionalization used previously,[1–3] the dispersion equation (1) nondimensionalized by this method contains the parameters W, τ, and the wave number x in explicit form and not combined in more complicated parameters, so that the instability growth rate of the free liquid surface can be investigated directly as a function of these parameters.

The behavior of the instability growth rates, determined by the imaginary positive component of the dimensionless frequency as a function of the dimensionless wave number x, calculated using formula (1) for $\beta=1$ and various values of the characteristic time τ for relaxation of the viscous stresses in the liquid, is plotted in Figs. 1a ($W=3$) and 1b ($W=6$). It is easy to see that in this range of values of the characteristic dimensionless viscosity relaxation time τ, $0.11\geqslant\tau\geqslant 1$ this dependence is very appreciable and for $W=6$ a 100% increase in growth rate is observed as τ increases from 0.11 to 1. The range of wave numbers x in which instability occurs does not depend on the characteristic relaxation time τ of the viscous stresses and is determined only by the Tonks–Frenkel parameter W, expanding toward higher wave numbers (into the capillary wave range) and toward lower wave numbers (into the gravitational wave range) as this parameter increases.

[1] S. O. Shiryaeva and O. A. Grigor'ev, Pis'ma Zh. Tekh. Fiz. **21**(9), 67 (1995) [Tech. Phys. Lett. **21**, 346 (1995)].
[2] O. A. Grigor'ev and S. O. Shiryaeva, Izv. Ross. Akad. Nauk Ser. Mekh. Zhidk. Gaza No. 98–105 (1996).
[3] S. O. Shiryaeva, O. A. Grigor'ev, M. I. Munichev, and A. I. Grigor'ev, Zh. Tekh. Fiz. **66**(10), 47 (1996) [Tech. Phys. **41**, 997 (1996)].
[4] Yu. A. Bykovskiĭ, É. A. Manykin, I. E. Nakhutin *et al.*, Zh. Tekh. Fiz. **46**, 2211 (1976) [Sov. Phys. Tech. Phys. **21**, 1302 (1976)].

Translated by R. M. Durham

Broadening of the particle resonance drift trajectory and tritium injection into a fusion reactor with an $l=3$ helical winding

A. A. Shishkin, O. Motojima, and É. I. Polunovskiĭ

Institute of Plasma Physics, ''Kharkov Physicotechnical Institute'' National Science Center, Kharkov 108, Ukraine; National Institute for Fusion Science, Tokyo 509-5292, Japan; Kharkov State University, Kharkov 77, Ukraine

(Submitted April 7, 1998)
Pis'ma Zh. Tekh. Fiz. **25**, 5–13 (January 26, 1999)

Two fusion reactor problems, removal of helium ash and fuel (tritium) injection, can be solved using the concept of ''drift island motion.'' The motion of a drift island is an indicator of the broadening of the resonant trajectory of a charged particle guiding center. This trajectory broadening occurs if two conditions are satisfied. First, the drift pitch angle of the particle is equal to the resonance values $i^*=n/m$, where n and m are the ''wave numbers'' of the perturbing magnetic field. Second, the drift pitch angle $i^*=n/m$ ''moves'' over the plasma cross section as the particle moves. This displacement is caused by a slow change in the helical magnetic field with time as the particle moves. It is shown that this effect may occur in a fusion reactor with an $l=3$ helical winding and may be used for tritium ion injection.
© *1999 American Institute of Physics.* [S1063-7850(99)01701-2]

1. INTRODUCTION

We shall first explain the essential features of the physical effect. It is well-known that on a rational magnetic surface with the rotational transform angle $l=n/m$ a chain of m magnetic islands forms under the action of a magnetic perturbing field with the ''wave'' numbers n and m. This behavior is a manifestation of the resonance property of the magnetic field line. These magnetic islands can be seen by collecting the field line traces in the meridional cross sections of the torus. In magnetic traps with helical current coils the position of the magnetic islands in the cross section of the magnetic configuration can be controlled by varying the helical magnetic field. For stronger helical fields the magnetic islands form closer to the center of the plasma and for weaker fields they form closer to the periphery.

A free particle with the drift pitch angle $i^*=n/m$ can also form islands under the action of the same magnetic perturbing field; these are called ''drift islands.'' The drift island is displaced relative to the magnetic one. This displacement depends on the particle energy W and on the ratio of the longitudinal velocity (relative to the magnetic field) to the total particle velocity $V_\parallel/V$ (pitch velocity). The position of the drift island can also be varied by varying the helical magnetic field.

A fundamentally important characteristic for our investigation is the variation of the helical magnetic field with time during the plasma pulse. By varying the helical magnetic field during the particle motion and conserving the drift resonance condition, we can force a charged particle such as a cooled α-particle (helium ash) to drift from the center of the plasma toward the edge or inject a tritium ion from the edge into the center of the plasma.

In a tokamak a similar mechanism can be achieved if the perturbing magnetic field is helical and time-dependent and the perturbation frequency is also a function of time.[1] In a magnetic trap with helical conductors motion of a drift island can be achieved by varying the fundamental magnetic field with time.[2] Drift resonances with $m=1$, $n=1$ and $m=2$, $n=1$ can be used in an $l=2$ magnetic system.[2] Here we examine how this mechanism could take place in an $l=3$ magnetic system, which is viewed[3,4] as the possible basis for a fusion reactor with a strong magnetic field (12 T). An $l=3$ system has the advantage that the electrodynamic forces between the helical conductors can be reduced, so that the technically attainable magnetic field can be increased.

A specific feature of an $l=3$ magnetic configuration is the lower rotational transform angle compared with the $l=2$ case and the higher shear. Here we show that in a steady-state fusion reactor based on a magnetic system with $l=3$ helical windings, the resonance of the drift pitch angle $i^*=1/3$ and a magnetic perturbation with the wave numbers $m=3$, $n=1$ can be successfully utilized.

2. BASIC EQUATIONS AND MAGNETIC FIELD MODEL

For our analysis we shall use the equations of particle motion in the drift approximation[5]

$$\frac{d\mathbf{r}}{dt}=V_\parallel\frac{\mathbf{B}}{B}+\frac{M_jc(2V_\parallel^2+V_\perp^2)}{2eB^3}\mathbf{B}\times\nabla B,$$

$$\frac{dW}{dt}=\frac{M_jV_\perp^2}{2B}\frac{\partial B}{\partial t},\quad \frac{d\mu}{dt}=0. \tag{1}$$

Here W is the particle kinetic energy, $V_\parallel$ and $V_\perp$ are the parallel and perpendicular components of the particle velocity, M_j and e_j are the particle mass and charge, $\mathbf{B}$ is the

 © 1999 American Institute of Physics

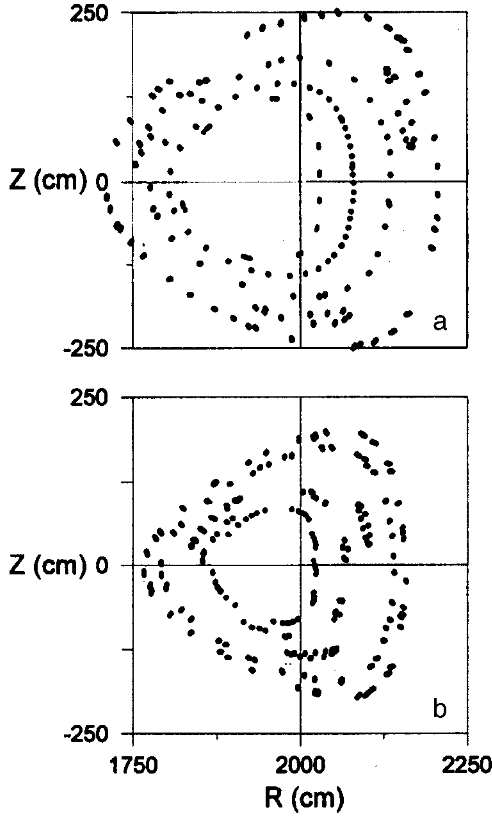

FIG. 1. Drift surfaces of a free tritium ion with the initial starting points $r_0=30.5$, 82.5, 142.5, 172.5, 212.5 cm, $\vartheta_0=\pi/10$, $\varphi_0=0$ for $\varepsilon_{3,18}=0.38$ (a) and $r_0=20.5$, 75.5, 105.5, 145.5, 162.5 cm, $\vartheta_0=\pi/10$, $\varphi_0=0$ for $\varepsilon_{3,18}=0.64$ (b) in the meridional cross section drawn at the beginning of the period of the perturbing magnetic field.

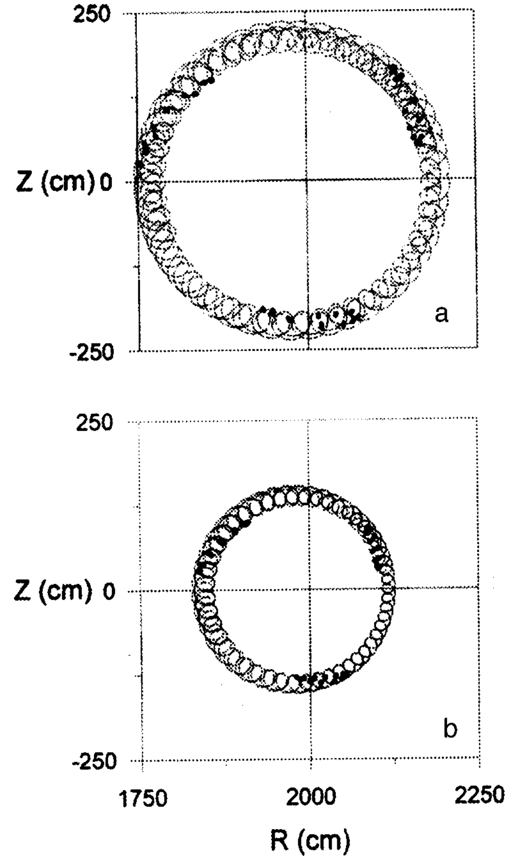

FIG. 2. Projection of a tritium ion trajectory with the initial starting point $r_0=172.5$ cm, $\vartheta_0=\pi/10$, $\varphi_0=0$ for $\varepsilon_{3,18}=0.38$ (a) and $r_0=105.5$ cm, $\vartheta_0=\pi/10$, $\varphi_0=0$ for $\varepsilon_{3,18}=0.64$ (b) in the meridional cross section (solid line) and corresponding drift islands (points).

magnetic field vector, μ is the transverse adiabatic invariant of the particle ($\mu=M_j V_\perp^2/2B$), and $\mathbf{r}$ is the position vector of the particle guiding center.

The fundamental magnetic field ($\mathbf{B}=\nabla\Phi$) is modeled using the scalar potential

$$\Phi=B_0\left[R\varphi-\frac{R}{m}\sum_n \varepsilon_{n,m}(r/a_h)^n\sin(n\vartheta-m\varphi)+\varepsilon_{1,0}\, r\sin\vartheta\right], \tag{2}$$

where B_0 is the magnetic field on the circular axis of the torus, R and a_h are the major and minor radii of the torus on whose surface lie the helical conductors, r, ϑ, φ are the coordinates of the observation point relative to the circular axis of the torus, r is the radial distance between the circular axis of the torus and the observation point, ϑ and φ are the angular displacements in the direction of the torus minor and major circumferences, and ϑ is measured from the direction opposite to the principal normal to the circular axis of the torus; the metric coefficients of the coordinates are as follows: $h_r=1$, $h_\vartheta=r$, $h_\varphi=R+r\cos\vartheta$; the summation index m is equal to m_h, which is the number of magnetic field periods over the length of the torus, and in our case this summation index is equal to l, where l is the number of poles of the helical winding, and $\varepsilon_{n,m}$ are the coefficients at the magnetic field harmonics.

For our investigation we used the parameters $l=3$, $m_h=18$, $R=20$ m, $a_h=3.3$ m, and $B_0=12$ T. The coefficients of the helical harmonics are given as

$$\varepsilon_{n,m}=\varepsilon_{n,m,0}+\varepsilon_{n,m,1}\sin(\Omega_{n,m}t+\delta_{n,m}), \tag{3}$$

we take $\varepsilon_{3,18,0}=0.51$, $\varepsilon_{3,18,1}=0.13$, and assume that the remaining coefficients $\varepsilon_{n,m}$ are zero. The phase is $\delta_{3,18}=-\pi/2$, $\varepsilon_{1,0}=0.003$, which corresponds to the presence of a transverse magnetic field whose magnitude is 0.3% of the fundamental longitudinal field. This transverse magnetic field produces a magnetic configuration with the magnetic axis shifted inside the torus, which provides better α-particle confinement.[4] The magnetic field frequency $\Omega_{3,18}$ is zero when the amplitude of the helical field does not vary with time and is 950 rad/s when the drift resonance is controlled dynamically.

The perturbing magnetic field is described in terms of the potential

$$\Phi_p=B_0 a_h\frac{\varepsilon_{n,m,p}}{m}(r/a_h)^m\sin(m\vartheta-n\varphi). \tag{4}$$

In our case, the wave numbers of the perturbing magnetic field are $m=3$, $n=1$ and its amplitude is $\varepsilon_{1,3,p}=0.001$.

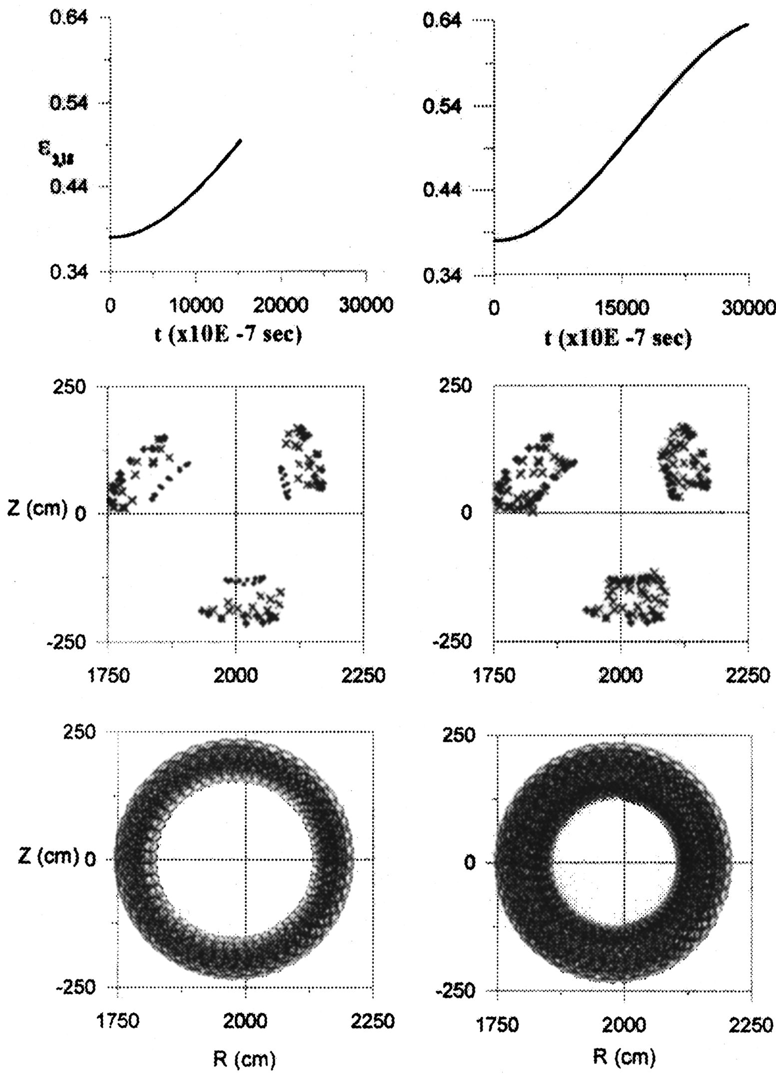

FIG. 3. Variation of the magnetic field amplitude with time (top diagram), motion of a drift island (middle diagram), and broadening of the resonance trajectory (bottom diagram) after $\tau = 1.5\times10^{-3}$ s (left) and 3.0×10^{-3} s (right).

3. TRITIUM ION INJECTION

We shall show how the resonance of the drift pitch angle with the perturbing magnetic field can be used to regulate the trajectory of a tritium ion with $W=350\,\mathrm{keV}$ and $V_\parallel/V=0.9$. If the amplitude of the helical field is kept constant at $\varepsilon_{3,18}=0.38$, three drift islands are formed by a trajectory with the initial coordinates $r_0=172.5\,\mathrm{cm}$, $\vartheta_0=\pi/10$, and $\varphi_0=0$ (Fig. 1a).

If the amplitude of the helical field is kept constant at $\varepsilon_{3,18}=0.64$, the family of drift surfaces (Fig. 1b) also has three significant islands at the site of the drift surface with $r^*=1/3$. These drift islands are formed by a particle trajectory whose starting point has the coordinates $r_0=105.5\,\mathrm{cm}$, $\vartheta_0=\pi/10$, and $\varphi_0=0$. These islands appear under the action of a perturbation with the wave numbers $m=3$, $n=1$. Chains of five islands formed by a trajectory with initial coordinates $r_0=75.5\,\mathrm{cm}$, $\vartheta_0=\pi/10$, $\varphi_0=0$, and also seven small islands formed by a trajectory with the initial coordinates $r_0=20.5\,\mathrm{cm}$, $\vartheta_0=\pi/10$, $\vartheta_0=0$, appear at the drift surfaces with $i^*=1/5$ and $i^*=1/7$, respectively, as satellite resonances.

The width of the resonance trajectory corresponds to the size of the drift island, as shown in Fig. 2.

Figures 1 and 2 show the drift surfaces, in particular the islands in the meridional cross section passing through the beginning of the period of the perturbing magnetic field. A similar pattern, but shifted with respect to ϑ, is found in other $\varphi=\mathrm{const}$ cross sections.

When the amplitude of the helical magnetic field changes from $\varepsilon_{3,18}=0.38$ to $\varepsilon_{3,18}=0.64$ (Fig. 3—top diagram), the drift island moves (Fig. 3—middle diagram) and the resonance trajectory becomes broadened (Fig. 3—bottom diagram). In Fig. 3 (middle diagram) the trajectory traces left by a particle during variation of the helical field and indicated by the $(\times)$ sign are superposed on the drift islands taken from Fig. 2. The drift islands for $\varepsilon_{3,18}=0.38$ are indicated $(+)$, and those for $\varepsilon_{3,18}=0.64$ are denoted by $(\cdot)$. Thus the pattern of drift island motion is clearer.

The choice of frequency $\Omega_{n,m}$ is a very important factor. The period of variation of the helical magnetic field amplitude should be comparable with but greater than the time taken for formation of the drift island. The time taken for formation of an island is taken to be the time during which the trajectory traces have time to ''circumnavigate'' each of the islands once.[2] This is the shortest time in which the particle trajectory traces delineate each of the chain of islands

once. After this time, the particle trajectory traces fill each of the islands with a large number of additional points.

Thus, tritium ions can be injected from the edge and moved into the center of the magnetic configuration.

4. DISCUSSION

We note the following points.

4.1. By varying the amplitude of the helical field from a larger value of $\varepsilon_{n,m}$ to a smaller value, we can move a particle with a specific energy W and ratio of longitudinal velocity to total velocity $V_{\parallel}/V$ from the center to the periphery. This can be used to remove helium ash from the center of an $l=3$ reactor. It should be borne in mind that by varying the drift pitch angle, we can regulate the motion of a free particle with a comparatively large ratio $V_{\parallel}/V$. A trapped particle can drift from the confinement volume under the action of a magnetic field gradient, whereas a free particle, forming a drift surface can only leave the confinement volume if this surface intersects the limiter. Thus, a free particle must be removed by using active methods of influencing it.

4.2. This transport mechanism has a selective property. Particles having values of W and $V_{\parallel}/V$ for which the drift pitch angle i^* is close to the resonance value come under control.[1,2]

4.3. Collisions between a mobile particle and plasma particles may affect the process and thus the influence of collisions on the conservation of drift resonance is currently being studied.

4.4. In practice, the helical field can be varied during the plasma pulse process. This has been achieved in Wendelstein 7A, a classical $l=2$ stellarator, in order to prevent the rotational transform angle from decreasing when the Ohmic heating current was switched off.[6] It is also planned to vary the field during the discharge process in the Large Helical Device (LHD),[2] where the pulse duration should be 1000 s.

5. CONCLUSIONS

This analysis of the drift motion of a charged particle, i.e., a tritium ion, in the magnetic configuration of a fusion reactor with an $l=3$ helical winding yields the following conclusions.

By using the resonance between the drift pitch angle $l^*=1/3$ and a perturbing magnetic field with the wave numbers $m=3$, $n=1$ and varying the helical magnetic field with time, it is possible to alter the particle trajectory so that the tritium moves from the edge into the center of the magnetic volume.

The variation of the magnetic field is slow and only half the period of variation of the helical magnetic field is used.

Thus, fuel can be injected into a fusion reactor.

The same physical mechanism and the same drift resonance can be used to remove helium ash from the center of the confinement volume to the edge.

[1] H. E. Mynick and N. Pomphrey, Nucl. Fusion **34**, 1277 (1994).
[2] O. Motojima and A. A. Shishkin, Plasma Phys. Contr. Nucl. Fusion (in press).
[3] O. Motojima *et al.*, in *Proceedings of the 23rd European Physics Society Conference on Controlled Fusion and Plasma Physics*, Kiev, 1996.
[4] O. A. Shishkin, Pis'ma Zh. Tekh. Fiz. **23**(22), (1997) [Tech. Phys. Lett. **23**, 895 (1997)].
[5] A. I. Morozov and L. S. Solov'ev, in *Reviews of Plasma Physics*, Vol. 2, edited by M. L. Leontovich (Consultants Bureau, New York, 1966), pp. 201–297.
[6] D. V. Bartlett *et al.*, in *Proceedings of the Eighth IAEA International Conference on Plasma Physics and Controlled Fusion Research*, Brussels, 1980, Vol. 1, p. 185.

Translated by R. M. Durham

Possibility of fabricating an inductive high-speed detector for electromagnetic radiation using thin $YBa_2Cu_3O_{7-\delta}$ films

I. G. Gogidze, P. B. Kuminov, A. V. Sergeev, and E. M. Gershenzon

Moscow State Pedagogical University

(Submitted September 1, 1997; resubmitted May 13, 1998)
Pis'ma Zh. Tekh. Fiz. **25**, 14–19 (January 26, 1999)

It is shown that an inductive high-speed nonequilibrium detector for electromagnetic radiation can be fabricated using thin YBaCuO films. An electronic detection regime has been obtained for the first time using a low-temperature inductive YBaCuO detector in the measuring frequency band $\Delta f = 1-50$ MHz and it has been shown that no bolometric detection regime exists at operating temperatures far below the superconducting transition. The time constant of the low-temperature inductive YBaCuO detector in the electronic regime is determined only by the electron–phonon interaction time in the nodal regions τ^d_{e-ph}. The detector has the following limiting characteristics: when the operating temperature is reduced from 10 to 1 K, the time constant τ_D varies between 10 and 100 ps and the sensitivity D^* improves substantially from 10^9 to 4×10^{12} W^{-1} cm Hz$^{1/2}$. © *1999 American Institute of Physics.* [S1063-7850(99)01801-7]

The use of the nonequilibrium response of high-temperature superconducting films as high-speed detectors is of particular interest. Recently, much work has been done on studying the resistive response, i.e., the change in the resistance under the action of radiation near the superconducting transition. The resistive response of YBaCuO films which we observed consists of two components. The first, picosecond, nonequilibrium component is caused by the electron–phonon relaxation while the second, nanosecond, component is ascribed to bolometric heating of the superconducting film, which relaxes as a result of phonon drift across the boundary.[1,2] The presence of bolometric ''tails'' is an important negative factor which limits almost all the applications of the nonequilibrium picosecond response of high-temperature superconducting (HTSC) films. For instance, the parameters of terahertz hot-electron mixers using HTSC films are several orders of magnitude inferior to those of similar mixers using conventional superconductors.[3] Lowering the operating temperature and going over to the purely superconducting state can suppress the bolometric effect; in our view this is a promising method of achieving good parameters for electronic detectors and mixers.

Despite the enormous interest being shown in high-temperature superconductors and the extensive investigations carried out so far, nonequilibrium effects in the superconducting state of these materials have been little studied. Few data are available on the quasiparticle relaxation and recombination times and the dynamics of the order parameter. Given this state of affairs, it is impossible to make detailed calculations of the parameters of an inductive detector at the present time. Sergeev and Reizer[4] reported a theoretical analysis of the kinetics of HTSC films using a *d*-pairing model which is supported by many experiments, including our results. In our view, such an analysis can provide a qualitatively accurate description of the characteristics of HTSC materials, the main one being the existence of nodal regions in the quasiparticle spectrum.

Studies of the electron kinetics in HTSC materials are complicated mainly because of the structure of the order parameter. The existence of nodal regions where the superconducting gap is small qualitatively changes the electron scattering processes compared with those in conventional superconductors. As a result, the characteristic times in HTSC materials are substantially shorter, which makes the nonequilibrium effects in these materials more difficult to record, but is more promising for applications in high-speed (picosecond) electronics.

In high-temperature superconductors at low temperatures the quasiparticles are concentrated in nodal regions, so the recombination and relaxation times only differ by the coherence factors and are of the same order. Both these times increase only exponentially with decreasing temperature. The electron relaxation time in the resistive state near the superconducting transition in YBaCuO films was measured at $\simeq 2$ ps in Ref. 5. Thus, even at liquid helium temperatures, the predicted characteristic electron times are less than 100 ps.

Experimental investigations of the inductive response near the superconducting transition show that the electron kinetics differ very little from the processes in the resistive state.[6] In this temperature range two-time relaxation is observed, in which the picosecond processes are caused by electron–phonon interaction and the nanosecond processes are caused by phonon drift across the HTSC film–substrate interface (bolometric effect). By reducing the temperature and using thinner films, it is possible to avoid the bolometric effect.

The results of recent experiments to study microwave response, NMR, and photoemission uniquely demonstrate the existence of low-energy excitations in nodal regions.[7] An

 © 1999 American Institute of Physics

investigation of the phase coherence of edge SQUIDs confirms the idea of *d*-pairing,[8] and *d*-symmetry is also deduced from a model in which pairing is caused by exchange of antiferromagnetic spin fluctuations.[9] As a result of the presence of nodal lines, the low-temperature behavior of a superconductor is very sensitive to impurities. Without electron–impurity scattering the density of states of the quasiparticles is a linear function of energy near the Fermi surface. Even low impurity concentrations lead to a constant density of quasiparticle states which depends on the electron–impurity potential.[10]

As a result of the absence of any singularity in the density of states, the quasiparticle recombination time does not increase exponentially at low temperatures. Thus, the photoresponse cannot be described using the Owen–Scalapino model.[11] It has been noted that experiments near the transition reveal very strong interelectron interaction. Having assumed that the electron–electron interaction also predominates over the electron–phonon interaction in the superconducting state, we can use a kinetic scheme with a nonequilibrium electron temperature.

In the experiments we recorded the ac voltage ΔU at a sample inserted in a dc circuit of current I, formed under the action of modulated near-infrared radiation. The radiation source was a 788 nm semiconductor laser diode. The signal from the sample at frequencies up to 50 MHz was recorded using a phase-sensitive EGG-502 device.

At the beginning of the measurements we determined the maximum permissible radiation power for which the concentration of photoexcited quasiparticles was equal to the concentration of equilibrium particles, i.e., when the number of nonequilibrium quasiparticles generated by the radiation was approximately equal to the number of thermal quasiparticles. The sample displacement current was substantially below the critical level.

The amplitude–frequency characteristics of the inductive signal obtained at two different operating temperatures ($T_1 = 4.2$ K and $T_2 = 25$ K) are shown in Fig. 1. It can be seen that at $T = 4.2$ K the signal amplitude increases linearly as the modulation frequency of the incident laser radiation power increases over the entire band of measuring frequencies (see Fig. 1a). As the operating temperature increases ($T = 25$ K), the amplitude–frequency characteristic of the signal reveals a plateau after the modulation frequency $f = 30.8$ MHz with a characteristic time $\tau \simeq 5.2$ ns (see Fig. 1b).

Low-temperature investigations of samples with $\tau_{es} \simeq 5.2 \pm 0.2$ ns (Ref. 12) revealed that at $T = 4.2$ K the sample has an ascending amplitude–frequency characteristic as far as modulation frequencies $f = 50$ MHz (instrumental time $\tau = 3.18$ ns), i.e., the signal amplitude is directly proportional to the modulation frequency of the incident laser radiation power. If the relaxation of the response were to have two components, we would observe a plateau on the amplitude-frequency characteristic at $f = 30.8$ MHz in our band of measurement frequencies ($\Delta f = 50$ MHz).

Our experimental results confirm that the HTSC has a purely nonequilibrium response at low temperatures, i.e., no bolometric effect is observed at operating temperatures far below the superconducting transition, and they suggest that a

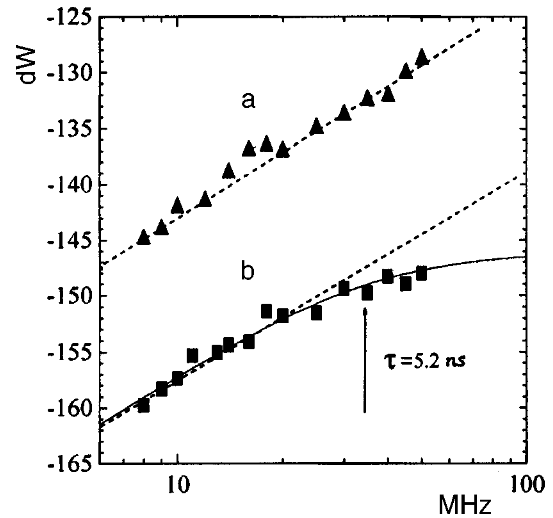

FIG. 1. Amplitude–frequency characteristics of the inductive signal of a $YBa_2Cu_2O_{7-\delta}$ detector (film thickness 500 Å, $LaAlO_3$ substrate) with a displacement current of 5 mA and an incident modulated laser radiation power of 7 dW at various temperatures: a — 4.2 K and b — 25 K.

nonequilibrium inductive high-speed detector can be fabricated using YBaCuO thin films.

We now discuss the basic parameters of a YBaCuO inductive detector such as the time constant τ_d and the sensitivity D^*. A kinetic scheme with a nonequilibrium electron temperature in HTSC films far from the superconducting transition presupposes that the time constant of the YBaCuO detector is equal to the electron–phonon relaxation time in the nodal regions τ^d_{e-ph}. At $T = 4.2$ K we find $\tau^d_{e-ph} \simeq 15$ ps (Ref. 5). At temperatures around $T = 10$ K the time constant of a nonequilibrium inductive YBaCuO detector is then $\tau_D \simeq 10$ ps.

Following Ref. 4, the sensitivity of a nonequilibrium inductive HTSC detector is

$$D^* = \sqrt{\frac{\tau^d_{e-ph}}{4T^2 c_q d}}, \tag{1}$$

where c_q is the quasiparticle concentration in the nodal regions which can be estimated using the formula

$$\frac{c_q(T)}{c_e(T_c)} \approx 1.54 \left(\frac{T}{T_c} \right)^2, \quad T \ll \Delta. \tag{2}$$

At $T = 10$ K we find $c_q \simeq 4 \times 10^{-5}$ J cm^{-3} K^{-1} and thus the sensitivity of an inductive YBaCuO detector is $D^* = 10^9$ W^{-1} cm Hz$^{1/2}$. When the temperature is reduced to $T = 1$ K the sensitivity improves by more than three orders of magnitude to $D^* = 4 \times 10^{12}$ W^{-1} cm Hz$^{1/2}$, while the detector time constant is only two orders of magnitude inferior at $\tau_D = 100$ ps. It can be seen that an inductive nonequilibrium detector possesses a high detection sensitivity because of the low quasiparticle concentration and the extremely high speed. A disadvantage of this detector is the low current–power sensitivity which leads to fairly stringent constraints on the amplifier used in the recording regime.

This work is supported by the ''Superconductivity'' topic of the State Program ''Topical Problems in the Physics of

Condensed Media,'' under Project No. 96128 and by the Russian Fund for Fundamental Research, Project No. 1-068/4.

[1] E. M. Gershenzon, G. N. Gol'tsman, I. G. Goghidze *et al.*, Physica C **185–189**, 1371 (1991).
[2] E. M. Gershenzon, I. G. Gogidze, G. N. Gol'tsman *et al.*, Pis'ma Zh. Tekh. Fiz. **17**(22), 6 (1991) [Sov. Tech. Phys. Lett. **17**, 786 (1991)].
[3] E. M. Gershenzon, G. N. Gol'tsman, I. G. Gogidze *et al.*, Sverkhprovodimost' KIAE **3**, 1711 (1990).
[4] A. V. Sergeev and M. Yu. Reizer, Int. J. Mod. Phys. B **10**, 635 (1996).
[5] É. E. Aksaev, E. M. Gershenzon, G. N. Gol'tsman *et al.*, Sverkhprovodimost' KIAE **3**, 1928 (1990).
[6] G. N. Gol'tsman, P. B. Kouminov, I. G. Goghidze, and E. M. Gershenzon, IEEE Trans. Appl. Supercond. **5**, 2591 (1995).
[7] K. Kitazawa, Physica C **235–240**, xxiii (1994).
[8] D. A. Wollman, D. J. Van Harlingen, W. C. Lee *et al.*, Phys. Rev. Lett. **71**, 2134 (1993).
[9] D. Pines, Physica B **199–200**, 300 (1994).
[10] Ye Sun and K. Maki, Phys. Rev. B **51**, 6059 (1995).
[11] C. S. Owen and D. J. Scalapino, Phys. Rev. Lett. **28**, 1559 (1972).
[12] A. V. Sergeev, A. D. Semenov, P. B. Kouminov *et al.*, Phys. Rev. B **49**, 9091 (1994).

Translated by R. M. Durham

Damage to an electric double layer by a weak shock acoustic wave

G. N. Sankin and V. S. Teslenko

Institute of Hydrodynamics, Siberian Branch of the Russian Academy of Sciences, Novosibirsk
(Submitted June 18, 1998)
Pis'ma Zh. Tekh. Fiz. **25**, 20–23 (January 26, 1999)

Results are presented of experimental investigations of the dynamics of the electrical conductivity of an electrolyte when one of the electrodes is exposed to a weak shock pulse. It is shown that the electrical conductivity in the cell increases as a result of damage to the electric double layer. © *1999 American Institute of Physics.* [S1063-7850(99)01901-1]

A method of measuring the electrical conductivity in cells containing different solid and liquid media is widely used in shock wave physics.[1,2] The familiar approaches mainly apply to fairly strong shock waves ($\geqslant 10$ MPa). Here we demonstrate that changes in the electrical conductivity may be recorded for weak (less than a few megapascal) shock acoustic waves and their relaxation characteristics may be studied in the near-electrode layer.

The kinetics of the electrical conductivity in shock waves is usually measured with ac voltages applied to the cell. This is to eliminate the formation of an electrical double layer at the electrodes. As a result, for ac voltages when a shock wave propagates through the cell, changes in the electrical conductivity are recorded in the bulk of the measuring cell.

Unlike existing systems, we used a dc voltage applied to the cell.

For the main series of experiments we used a 16 mm diameter cylindrical Teflon cell with 5 mm thick planar electrodes 10 mm apart. Platinum, stainless steel, brass, and also carbon electrodes were tested. The results presented for this cell refer to the case of platinum electrodes. The cell was filled with aqueous solutions of NaCl at different concentrations at temperatures of 295–300 K. The pulsed source was a metal plunger dropped onto one of the electrodes. The pulse duration depended on the length of the plunger and was 7 μm for the results presented here. The pressure in the acoustic wave was determined from the plunger velocity[3] and varied depending on the drop height of the plunger. In the experiments the current was measured by a bridge method and was recorded using a computerized digital oscilloscope. The time resolution was 1.5 s, depending on the measuring system used. The current variation was measured with an error of less than 10%.

Figures 1 and 2 give the results of measuring the increase in current when the positive electrode was exposed to the shock action.

Figure 1a shows an oscilloscope trace of the relative increase in current for a 0.25 M NaCl solution (pressure in wave 2.8 MPa). The relaxation time during which the current variation decreases $e \approx 2.7$ times was $\tau = 21$ s for this trace.

It was established that the amplitude of the current increase is proportional to the amplitude of the pressure pulse generated (Fig. 1b). The threshold pressure at which the effect begins to be observed (determined by extrapolating the curve until it intersects the coordinate axis) is (0.5 ± 0.1) MPa.

For a pressure pulse of 3.1 MPa measurements were made of the increase in current as a function of the voltage between the electrodes for various NaCl concentrations. Figure 2 gives the results for two concentrations: (*1*) — 2M NaCl and (*2*) — 0.2 M NaCl.

The amplitude of the current variation as a function of voltage has a local maximum at 0.9 V. At all the voltages used, the amplitude of the current variation was larger for the more concentrated solution (2M NaCl) (Fig. 2a). The relative current variation at the maximum point was 3.6% for 2M NaCl and 14% for 0.2M NaCl. Figure 2b gives the relative change in current as a function of the voltage.

Experiments were carried out using a *U*-shaped cell with carbon electrodes in order to identify the role of the electrode polarity. The cell was made from a curved *U*-shaped polyethylene tube of 4 mm inner diameter and 70 mm length, with carbon electrodes at the ends. In this setup the shock acoustic wave was significantly attenuated when it reached the second electrode. As a result, it was established that the processes at the anode predominate (when the cathode and the anode are exposed to the same action). The amplitude of the current variation was between five and six times greater for action on the positive electrode compared with that on the negative electrode.

In order to identify the role of the electrolyte polarization, we carried out experiments to record the change in the electrical conductivity in these systems when an ac voltage of 1 V was applied at frequencies of 100 Hz and 1 kHz. As was shown by the ac measurements, the amplitude of the acoustic pulses used (up to 3.5 MPa) was insufficient to excite processes causing a change in the electrical conductivity in the bulk of the electrolyte. The current remained constant to within $\leqslant 0.5\%$.

To conclude, it has been found that 1) when a weak shock wave acts on a cell containing an electrolyte, an increase in electrical conductivity is only observed when a dc current is used; 2) after a shock pulse a fairly long time ($\tau \approx 20$ s) is required to restore the electrical conductivity at the cell, and 3) the current variation differs when the positive and negative electrodes are exposed to the action. These results confirm that damage to the electric double layer is the

 © 1999 American Institute of Physics

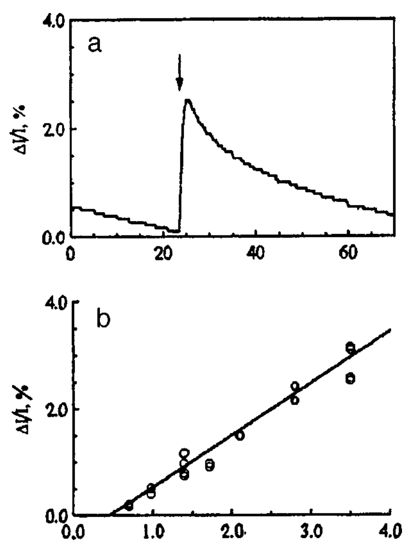

FIG. 1. Relative variation of the current through the cell under acoustic shock as a function of time, the time of impact being indicated by the arrow (a) and as a function of the acoustic wave pressure (b) for a 0.25M NaCl solution.

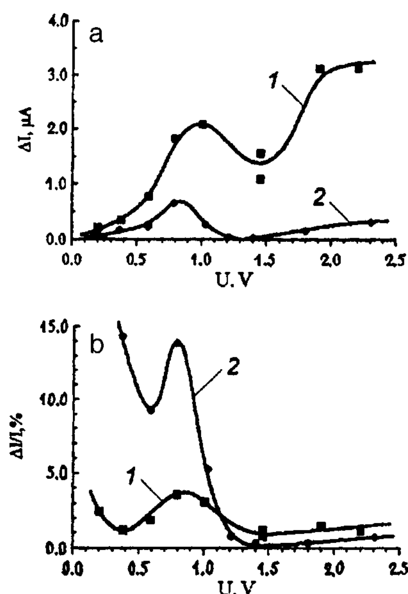

FIG. 2. Absolute (a) and relative (b) changes in current as a function of cell voltage at a pressure of 3.1 MPa for various electrolyte concentrations: *1* — 2M and *2* — 0.2M NaCl solution.

main factor responsible for increasing the current when a shock wave acts on the cell. The different amplitude of the current variation when the electrodes of different polarity are exposed to the action indicates that the effect depends on the structure of the double layer (particle composition and concentration, binding energy).

This effect may be used to develop new methods in shock wave physics and polarography.

The authors are grateful to V. V. Mitrofanov for useful discussions of this work. This work was partially supported by the Russian Fund for Fundamental Research (Grant No. 96-02-19329).

[1] H. Hoffman and E. Yeager, Rev. Sci. Instrum. **39**, 1151 (1968).
[2] A. C. Mitchell and R. N. Keeler, Rev. Sci. Instrum. **39**, 513 (1968).
[3] V. I. Laptev and Yu. A. Trishin, Prikl. Mekh. Tekh. Fiz. No. 6, 128 (1974).

Translated by R. M. Durham

Fiber ring laser with locked relaxation oscillations

V. I. Belotitskiĭ and M. P. Petrov

A. F. Ioffe Physicotechnical Institute, Russian Academy of Sciences, St. Petersburg
(Submitted September 13, 1998)
Pis'ma Zh. Tekh. Fiz. **25**, 24–28 (January 26, 1999)

An investigation is made of the locking of the relaxation oscillations in a fiber ring laser with an active medium of phosphorus aluminosilicate glass doped with erbium and ytterbium ions. It is shown that stable pulse-periodic emission in the 1.5 μm range can be achieved at a pulse repetition frequency between 80 and 160 kHz with a pulse length of 2–3 μs. A single-mode model is used to determine the laser parameters (the pumping rate and the photon lifetime in the cavity). © *1999 American Institute of Physics.* [S1063-7850(99)02001-7]

Stable emission of a sequence of micro- and submicrosecond pulses can be achieved in solid-state lasers by locking the relaxation oscillations. In studies known to us low-frequency modulation of the pump radiation has been used to lock the relaxation oscillations in fiber lasers.[1–3] Fiber lasers with modulated pumping near relaxation frequencies have also exhibited more complex nonlinear behavior (double- and quadruple-period modulation) as well as a chaotic response.[2] Here we report locking of the relaxation oscillations of a fiber ring laser when pulse-periodic optical radiation from a semiconductor laser, whose wavelength lies in the gain band of the activated fiber, was injected into the fiber laser.

The experimental configuration of the fiber ring laser is shown schematically in Fig. 1. The active medium was a single-mode section of 1.5 μm optical fiber, whose properties and characteristics were similar to those of the fibers described by Townsend *et al.*[4] The length of the activated fiber was 3.5 m. The fiber core, made of phosphorus aluminosilicate glass was doped with erbium and ytterbium ions (erbium doping level around 500 ppm, Er:Yb ion ratio 1:20, $NA \sim 0.16$). The losses in the fiber were less than 0.16 dB/m. The additional ytterbium doping allowed us to use a 1064 nm cw Nd:YAC laser as the pump laser. The average maximum pump power in the activated fiber was less than 500 mW.

This ytterbium–erbium glass fiber ring laser also incorporated a wave demultiplexer, which combined the signal radiation and the 1064 nm pump radiation and fed them to the active fiber, a polarization-insensitive magnetooptic isolator, and a 1:10 coupler, which was used to couple out the fiber laser radiation and couple in the semiconductor laser radiation. The length of the fiber laser corresponded to an intermode beat frequency of 16 MHz. The emission wavelength of the ring laser was 1535 nm and the average maximum radiation power was less than 30 mW and remained almost constant both when running under synchronized relaxation oscillations and when free running.

Semiconductor lasers whose wavelength fell within the gain band of the Yb–Er fiber were used to lock the relaxation oscillations. The average semiconductor laser power coupled into the ring laser was less than 100–500 μW. The semiconductor lasers were modulated by rectangular current pulses whose repetition frequency could be varied widely.

The free-running regime was investigated using pulsed and cw pumping. When the ring laser shown in Fig. 1 was pumped by rectangular pulses (pulse length around 2 ms, switchon–switchoff time less than 40 μs, pulse repetition frequency 50 Hz), damped oscillations were observed, which reached a steady state typical of solid-state lasers. The characteristic damping time of the transient oscillations depended on the pump power, and at the pumping rates noted above the shortest time observed by us was around 70 μs.

Under cw pumping the emission from the cw fiber ring laser was also cw. The rf spectrum in the relaxation oscillation range had a clearly defined noise character and the position of the maximum depended on the pumping.

When the fiber ring laser was pumped by a 1064 nm cw

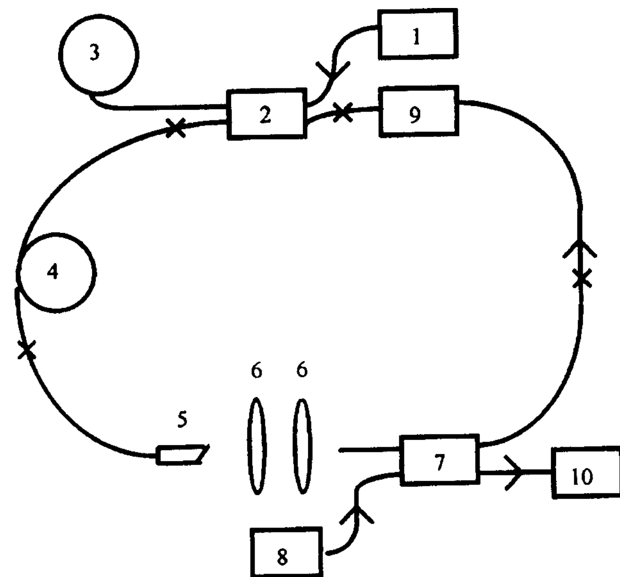

FIG. 1. Schematic of Er:Yb fiber ring laser: *1* — pump laser, *2* — wave demultiplexer, *3* — silicon photodiode to indicate pump power, *4* — Er:Yb fiber, *5* — optical fiber with end polished at an angle of 10°, *6* — microscope objectives for coupling light from fiber to fiber, *7* — 1:10 optical coupler, *8* — semiconductor laser used to lock the relaxation oscillations, *9* — optical isolator, *10* — germanium photodiode to record output radiation from ring laser. The crosses indicate the splicing points and the arrows indicate the directions of propagation of the radiation.

 © 1999 American Institute of Physics

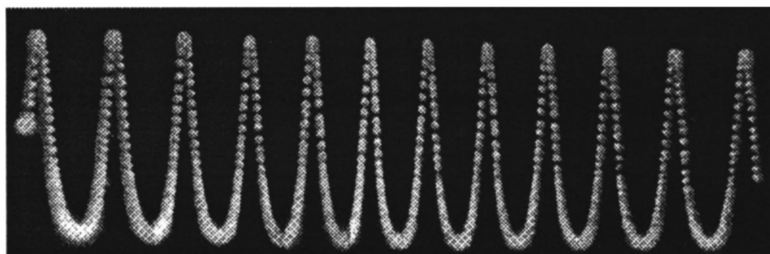

FIG. 2. Oscilloscope trace of radiation from fiber ring laser when the relaxation oscillations are locked by injecting semiconductor laser radiation into the ring laser.

signal and radiation from a semiconductor laser pumped by rectangular current pulses was also injected into the fiber laser, the emission from the ring laser changed substantially when the pulse repetition frequency was close to the frequency of the relaxation oscillations and the semiconductor laser wavelength was in the gain band of the fiber laser. In particular, the ring laser radiation was of a pulsed-cw nature (the ratio of the peak power of the pulsed signal to the minimum signal between pulses was greater than 100, Fig. 2) and the rf spectrum in the relaxation oscillation range was no longer noise-like.

Stable locking of the relaxation oscillations was observed in the range of 80–160 kHz with a pulse length less than 3 μs. The optimum pulse length of the semiconductor laser was half the period of the locking radiation.

It should be noted that the optimum locking frequency is determined by the pump power in this range of relaxation oscillation frequencies. The frequency of the relaxation oscillations (and thus the optimum locking frequency) is directly proportional to the square root of the pump power.

These results can be used to determine various parameters of this laser if we use a single-mode model described by rate equations.[5] The model indicates that the decay law of the spike amplitude under free-running with pulsed pumping is given by

$$m_{\max}=m^0_{\max}\exp(-2\alpha t/3T_1), \tag{1}$$

where $m_{\max}$ is the maximum amplitude of the spikes for damped transient oscillations, α is the pump parameter, and T_1 is the relaxation time of the population difference (in our case $T_1=10\,\mathrm{ms}$). The experimental results from studies of transient pulsations and formula (1) yielded the pump parameter $\alpha=100$. The same pump power was used to measure the optimum locking frequency of the relaxation oscillations (or the frequency of the relaxation oscillations), which corresponded to 111 kHz. In this model, the frequency of the relaxation oscillations is given by

$$F=(1/2\pi)\sqrt{(\alpha-1)/T_1T_c}, \tag{2}$$

where T_c is the photon lifetime in the cavity. These results of calculating α and the experimental data for F yield the photon lifetime in the cavity $T_c=2\times10^{-8}$ s.

To conclude, we have shown that the relaxation oscillations of an ytterbium–erbium fiber ring laser can be locked by external pulse-periodic radiation from a semiconductor laser whose wavelength is close to the free-running wavelength of the fiber laser. This opens up possibilities for achieving stable periodic emission from fiber lasers.

The authors are grateful to E. L. Portnoĭ and G. B. Venus for supplying the semiconductor lasers.

[1] O. G. Okhotnikov and J. R. Salcedo, IEEE Photonics Technol. Lett. **6**, 367 (1994).
[2] E. Lacot, F. Stoeckel, and M. Chenevier, Phys. Rev. A **49**, 3997 (1994).
[3] S. I. Ionov and R. A. Reeder, Appl. Opt. **35**, 2580 (1996).
[4] J. E. Townsend, W. L. Barnes, K. P. Jedrzejewski, and S. G. Grubb, Electron. Lett. **27**, 1958 (1991).
[5] Ya. I. Khanin, *Dynamics of Quantum Oscillators (Quantum Radio Physics)* [in Russian], Sovet-skoe Radio, Moscow (1975), 496 pp.

Translated by R. M. Durham

Gallium telluride heterojunctions

V. N. Katerinchuk and M. Z. Kovalyuk

Institute of Problems in Material Science, National Academy of Sciences of Ukraine, Chernovtsy
(Submitted May 22, 1998)
Pis'ma Zh. Tekh. Fiz. **25**, 29–33 (January 26, 1999)

The photoelectric properties of In_2O_3–GaTe and GaTe–InSe heterojunctions were investigated. Their characteristics were described using a diffusion model of the heterojunction. Some deviation of the characteristics from ideal was observed for In_2O_3–GaTe heterojunctions as a result of the presence of a thin dielectric layer at the heteroboundary. Qualitative energy band diagrams were constructed for the heterojunction and their photosensitivity was determined in the range 0.33–1.0 μm. © *1999 American Institute of Physics.* [S1063-7850(99)02101-1]

Gallium telluride belongs to the group of layered III–V semiconductors and differs from most of the other compounds in this group in that single crystals can be obtained with relatively low resistivities. As a result of this property, it is possible to fabricate heterojunctions with negligible series resistance.

Here we study the photoelectric characteristics of two types of GaTe heterojunctions: n^+-In_2O_3–p-GaTe fabricated by pyrolysis of chemical solutions deposited on heated gallium telluride substrates to produce indium oxide,[1] and p-GaTe–n-InSe fabricated by fitting suitable semiconductors onto an optical contact.[2] An analysis of the literature[3,4] reveals that attempts have been made to develop similar heterojunctions, but in these studies attention was primarily focused on studying the spectral characteristics of the heterojunctions rather than their diode properties.

1. n^+-In_2O_3–p-GaTe. Plane-parallel gallium telluride substrates measuring $5\times5\times0.2$ mm were prepared from single-crystal ingots. No additional treatment was applied to the surface of the substrates, since this was already specular. An oxide film $\sim0.1\ \mu$m thick was formed by pulverizing an alcohol solution of indium chloride on the GaTe substrates heated to 400 °C. Indium was used for the contacts to the fabricated structure. The majority carrier concentrations in the p-GaTe and n^+-In_2O_3, determined from measurements of the Hall effect, were 10^{16} and $10^{20}\ cm^{-3}$, respectively. For the investigations we selected heterojunctions having the highest idle voltages, ~0.3 V, on exposure to ~100 mW/cm^2 light.

2. p-GaTe–n-InSe. Unlike the previous heterojunction, here the gallium telluride plays the role of the front-facing semiconductor. Since the majority carrier concentration in n-InSe is $\sim10^{14}\ cm^{-3}$, GaTe satisfies the requirements imposed on a front-facing semiconductor:[5] it does not impede the propagation of photons of lower energy than its band gap and it results in the formation of a p–n junction predominantly in the substrate, where the photogenerated carriers are absorbed and separated. Since contact between the semiconductors and the natural surfaces takes place in air at room temperature, the formation of an intermediate layer at the heteroboundary is almost eliminated.

RESULTS AND DISCUSSION

An investigation of the forward branches of the current–voltage characteristics of In_2O_3–GaTe heterojunctions revealed that, when plotted in semilogarithmic coordinates, their slope differs for different samples, i.e., the diode coefficient of the current–voltage characteristic may vary between 1.3 and 1.5. Figure 1 shows the current–voltage characteristics for two different forward-biased heterojunctions (curves *1* and *2*). The similar slope of the characteristic is most likely attributable to the influence of an intermediate dielectric layer[6] formed as a result of oxidation of the substrate prior to deposition of the In_2O_3.

It is difficult to avoid the formation of oxide, since it was observed that when GaTe substrates are heated, they very rapidly acquire a bright golden color. Intentional oxidation of the GaTe improves the diode coefficient but causes some deterioration in the photoelectric parameters of the heterojunction. Figure 1 also shows the forward branch of the current–voltage characteristic of a GaTe–InSe heterojunction (curve *3*) for which the slope is close to unity at 1.07. Temperature measurements in the range 210–300 K indicate that the diode coefficient remains the same. Thus, values of the diode coefficient close to unity indicate first, that the p–n junctions are of high quality and second, that the mechanism for carrier transport across the barriers of these heterojunctions is determined by diffusion.

If we bear in mind that the band gaps of InSe, GaTe, and In_2O_3 are 1.2, 1.7, and 3.7 eV, respectively,[7] these values should be reflected in the spectral photosensitivity of the heterojunctions. Figure 2 gives spectra of the relative quantum efficiency of these heterojunctions. These have the form of bands bounded on both sides and corresponding to the absorption of photons in the appropriate semiconductors. A characteristic feature is that the quantum efficiency increases with increasing photon energy.

Figure 3 shows qualitative energy band diagrams for the heterojunctions, which were constructed using data on the physical parameters of the semiconductors,[7] the majority carrier concentrations, and the band bending values. The capacitance–voltage characteristics were investigated in order to determine the diffusion potential φ_0 at the heterojunc-

 © 1999 American Institute of Physics

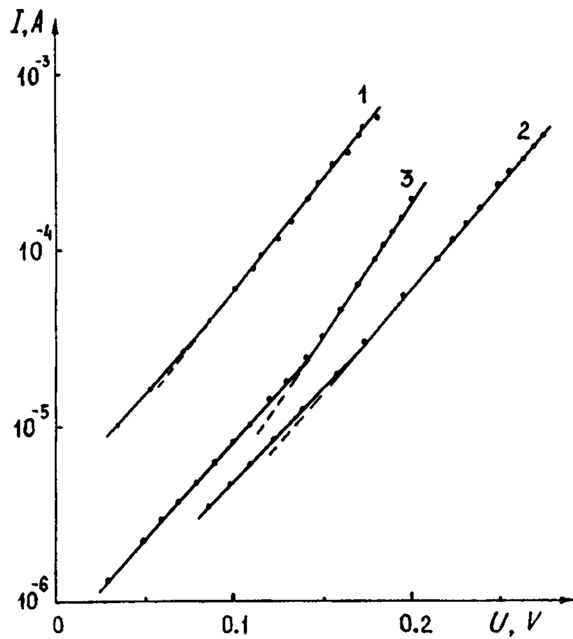

FIG. 1. Forward branches of the current–voltage characteristic of In_2O_3–GaTe (curves *1* and *2*) and GaTe–InSe heterojunctions (curve *3*) at room temperature.

tions. A method[8] whereby the capacitive cutoff voltage on the frequency dependent C^2-U plots was approximated by the value at zero frequency was used to obtain an accurate determination of φ_0. The value of φ_0 was 0.3 and 0.25 eV for the first and second heterojunctions, respectively. It can be seen from these diagrams that the forward current through the $p-n$ junction is determined in one case by the electrons (a) and in the other by the holes (b).

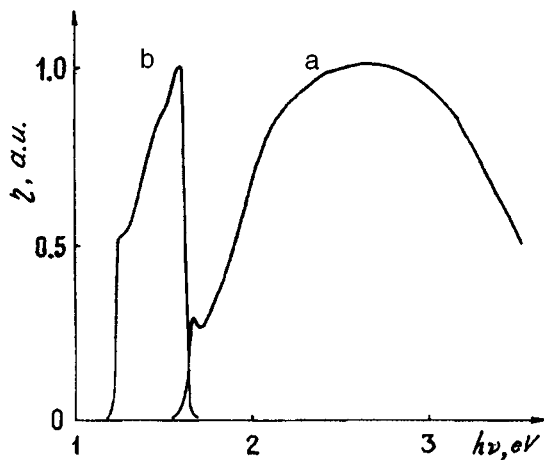

FIG. 2. Spectral dependence of the relative quantum efficiency of In_2O_3–GaTe (a) and GaTe–InSe (b) heterojunctions at $T=295$ K.

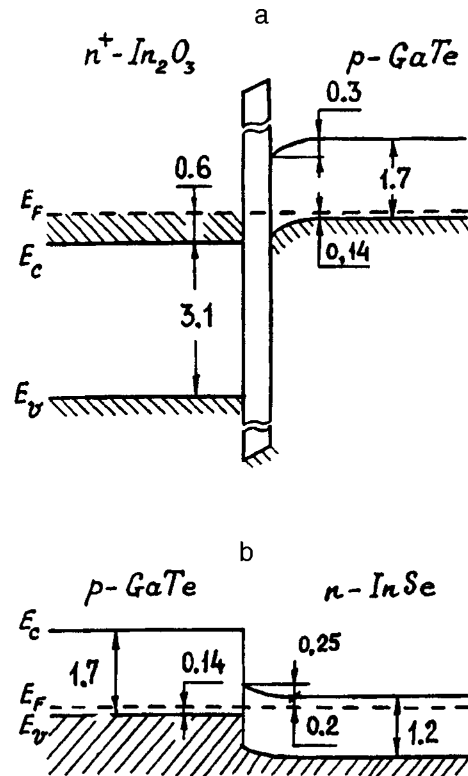

FIG. 3. Band diagrams of a In_2O_3–GaTe heterojunction with a thin dielectric (a) and GaTe–InSe (b) under equilibrium conditions; all the values are given in electronvolts.

Thus, these investigations have shown that the heterojunctions exhibit good diode properties with reproducible characteristics and photosensitivity in the wavelength range 0.33–1.0 μm. An important factor for In_2O_3–GaTe heterojunctions is that the intermediate oxide layer influences the photoelectric parameters. Because these heterojunctions are easy to fabricate, they can be used as the basis for inexpensive photodetector devices.

[1] A. L. Dawar and J. C. Joshi, J. Mater. Sci. **19**, 1 (1984).
[2] V. L. Bakumenko and V. F. Chishko, Fiz. Tekh. Poluprovodn. **11**, 2000 (1977) [Sov. Phys. Semicond. **11**, 1171 (1977)].
[3] A. I. Malik, V. B. Baranyuk, and Z. D. Kovalyuk, Fiz. Tekh. Poluprovodn. **14**, 409 (1980) [Sov. Phys. Semicond. **14**, 241 (1980)].
[4] K. Dovletov and F. Ragimov, Fiz. Tekh. Poluprovodn. **16**, 1631 (1982) [Sov. Phys. Semicond. **16**, 1041 (1982)].
[5] A. G. Milnes and D. L. Feucht, *Heterojunctions and Metal–Semiconductor Junctions* (Academic Press, New York, 1972; Mir, Moscow, 1975, 432 pp.).
[6] H. C. Card, Solid-State Electron. **20**, 971 (1977).
[7] *Landolt-Börnstein Numerical Data and Functional Relationships in Science and Technology, New Series Group III: Crystal and Solid State Physics* Vol. 17, edited by O. Madelung (Springer-Verlag, Berlin,1983, 562 p.)
[8] Yu. A. Gol'dberg, O. V. Ivanova, T. V. L'vova, and B. V. Tsarenkov, Fiz. Tekh. Poluprovodn. **18**, 1472 (1984) [Sov. Phys. Semicond. **18**, 919 (1984)].

Translated by R. M. Durham

Fractal characteristics of the deformation surfaces of a composite material and their correlation with the structure

I. N. Sevost'yanova and S. N. Kul'kov

Institute of Strength Physics and Materials Science, Siberian Branch of the Russian Academy of Sciences, Tomsk

(Submitted July 20, 1998)
Pis'ma Zh. Tekh. Fiz. **25**, 34–38 (January 26, 1999)

An investigation was made of the deformation relief formed at the surface of a solid under active deformation, and its fractal properties were determined. A correlation was established between the fractal dimension of the surface profile and the parameters of the fine crystalline structure of the material. © *1999 American Institute of Physics.* [S1063-7850(99)02201-6]

It is known that when materials undergo deformation, a deformation relief appears on the surface which is the result of changes taking place at different structural levels,[1] and which may be characterized by its fractal dimension.[2] A promising method of studying the fractal properties of deformation surfaces is to measure the fractal dimension using a scanning electron microscope.[3] However, no unambiguous data are available on the correlation between the fractal properties of this type of relief and the changes in the internal structure of the material.

Here we propose to study the fractal characteristics of the surface of a deformed solid alloy and to establish a correlation between the parameters of its fine crystalline structure and the deformation relief formed on the surface.

For the investigations we used a solid alloy containing tungsten carbide in an iron manganese steel matrix. The technology used to fabricate the solid alloy was described in Ref. 4. Samples of the solid alloy in the form of $4\times 4\times 5.5$ mm parallelepipeds were compressed using an Instron-1185 machine at a rate of 0.05 mm/s. The samples were compressed in 250 MPa steps and after each step, the load was removed and the side surface was examined.

The crystal structure was studied by x-ray structural analysis using a DRON-UM1 x-ray diffractometer with filtered iron radiation. The relief on the deformed surface was analyzed using an RÉM-200 scanning electron microscope with an accelerating voltage of 30 kV. The fractal dimension of the secondary electron signal emitted by the surface of the object was determined. For these investigations images of sections of the surface were recorded as a 512×512 array of points with a brightness gradation of 0–255. The experimentally determined plots of the surface profile ''roughness'' $Ln(L/L_0)$ as a function of the number of scale sections N are inverse sigmoid dependences (a so-called fractal graph), where L is the length of the broken profile and L_0 is the length of its projection.

A least-squares method was used to determine the slope of the linear section $|\alpha|$ of the fractal graph constructed for each line of the image. The fractal dimension was calculated from the relation $D=1+|\alpha|$ by averaging over all lines. Two methods of calculating the fractal dimension were used to analyze the relief of the deformed surface: measuring the fractal dimension of the surface as a whole (D_f) and measuring the fractal dimension at different scale levels (D_m). In this case, the measurements were made using two magnifications of the scanning electron microscope, $\times 250$ and $\times 5000$, which corresponded to frame sizes of the scanned surface of $400\times 400\,\mu$m and $20\times 20\,\mu$m, respectively. In the first case, an image of the entire surface was obtained by systematically moving the array, whereas in the second case the image was obtained at the center of the $400\times 400\,\mu$m frame section.

Metallographic investigations showed that after the appearance of residual plastic deformation, the surface of the material exhibited a deformation relief in the form of localized strain bands. These were oriented in two directions and were positioned at an angle of 45° to the axis of loading.

The main contribution to the plasticity of a composite material is made by the binder phase and thus changes in the internal structure during the deformation process were only analyzed for the binder, and it was assumed that the tungsten carbide does not undergo deformation. This assumption is justified, since the x-ray diffraction peaks for tungsten carbide showed no significant changes.

The regions of coherent scattering and the microstresses (ε) were determined from the (111) and (222) peaks of the binder phase. The most accurate description of the x-ray line profiles was obtained by approximating these by a Cauchy function. Measurements of the coherent scattering regions and microstresses during deformation of the solid alloy showed that as the residual strain increases, the size of the coherent scattering regions decreases because of the formation of a fine-crystalline structure in the binder phase of the composite, while the microstresses decrease during the plastic deformation process.

Figure 1 gives the fractal dimension as a function of the coherent scattering regions and the microstresses. An increase in the size of the coherent scattering regions leads to an increase in the fractal dimension. It should be noted that the changes in the fractal dimension on the scale level corresponding to the $20\times 20\,\mu$m frame size are considerably greater than those for the lower magnification. Moreover, when the values are extrapolated to large regions of coherent scattering and strong microstresses, the curves intersect, i.e.,

 © 1999 American Institute of Physics

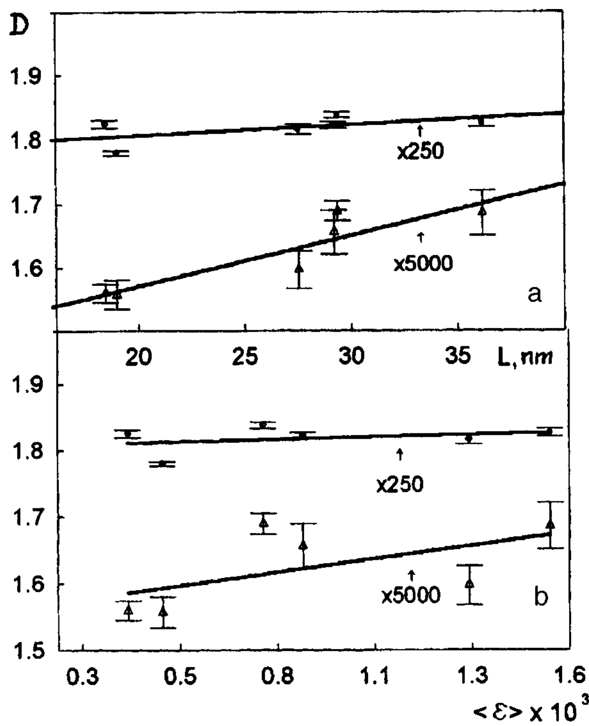

FIG. 1. Variation of the fractal dimension D as a function of the coherent scattering regions (a) and microstresses (b) measured at different scale levels during deformation of a solid alloy.

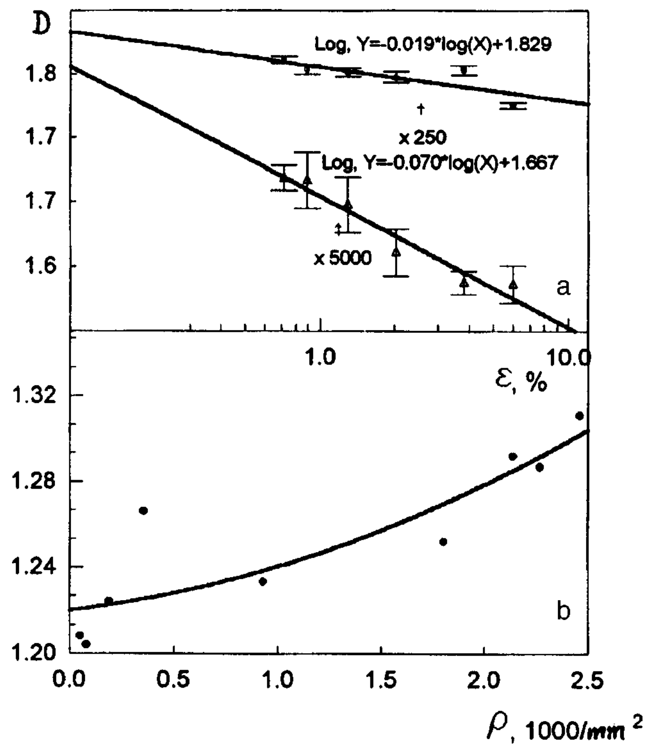

FIG. 2. Variation of the fractal dimension D_m as a function of the residual strain (a) and variation of the fractal dimension D_f as a function of the density of localized strain bands (b).

in the initial state (without residual strain), the fractal dimensions on different structural levels are the same.

Figure 2a gives the fractal dimensions D_m as a function of the residual strain. It can be seen that the values of D_m decrease on both scale levels and the dependences are accurately approximated by a linear function. The values of the fractal dimension show a larger variation on the lower scale level, for the $20\times20\,\mu$m frame size. When the linear plots are extrapolated to the undeformed state they intersect, which suggests that in an undeformed material the values of the fractal dimension D_m are the same at different structural levels.

Measurements of the fractal dimension (D_f) of the structure as a whole showed that this increases as the strain rate increases and as the density (ρ) of the localized strain bands increases (Fig. 2b). Moreover, the variation with increasing residual strain is greater than the variation in the density of the localized strain bands, and the best fit to the experimental values is a quadratic polynomial.

To conclude, these investigations have shown that there is a one-to-one correlation between the relief formed on a surface and its fractal dimension. The fractal characteristics of the relief are related to the microstructural parameters and have a linear functional dependence on the microstructural parameters of the binder phase, i.e., the regions of coherent scattering and the microstresses, which differs at different scale levels.

[1] V. E. Panin, Izv. Vyssh. Uchebn. Zaved. Fiz. No. 1, 7 (1998).
[2] J. Feder, *Fractals* (Plenum Press, New York, 1988; Mir, Moscow, 1991, 260 pp.).
[3] P. V. Korolev and S. N. Kul'kov, Perspekt. Mater. No. 3, 21 (1997).
[4] I. N. Sevost'yanova, S. F. Gnyusova, and S. N. Kul'kov, Izv. Vyssh. Uchebn. Zaved. Ser. Chern. Metall. No. 2, 21 (1996).

Translated by R. M. Durham

Negative differential resistance of a tunnel diode induced by an external microwave signal

D. A. Usanov, S. B. Venig, and V. E. Orlov

N. G. Chernyshevskiĭ State University, Saratov
(Submitted June 1, 1998)
Pis'ma Zh. Tekh. Fiz. **25**, 39–42 (January 26, 1999)

An experimentally observed effect is described in which a section of negative differential resistance appears on the current–voltage characteristic of a tunnel diode exposed to an external microwave signal when the diode bias voltage in the absence of the microwave signal is substantially below the peak value. The measurements were made for signal frequencies in the range 25–140 GHz. © *1999 American Institute of Physics.* [S1063-7850(99)02301-0]

It has been established that when a voltage above a certain (peak) value is applied to a tunnel diode, a section of negative differential resistance appears on its current–voltage characteristic. It has been shown[1] that the N-shaped current–voltage characteristic of a tunnel diode disappears when a high-power external microwave signal acts on the diode. This effect is caused by heating of carriers and by the influence of the direct component of the current through the diode produced by the detection effect.[2]

In Ref. 2 we did not investigate the influence of a microwave signal on the characteristics of a tunnel diode when the applied external bias is below the level at which the N-shaped current–voltage characteristic appears. Note that for this range of bias voltages the current–voltage characteristic of the tunnel diode is close to linear, and it is therefore not clear *a priori* whether action on a tunnel diode biased within the linear section of the current–voltage characteristic can result in a descending section. However, the results[1,2] suggest that the action of a microwave signal can substantially influence the behavior of the current–voltage characteristic, particularly as a result of the thermoelectric power of the hot carriers and the appearance of a microwave signal detection effect.

Experimental investigations were carried out to study the specific influence of an external microwave signal on the current–voltage characteristic. A tunnel diode or several series-connected 1I308 diodes were inserted using holders in a section of short-circuited waveguide of 7.2×3.4 mm cross section. The frequency of the radiation was 38 GHz. Using a waveguide construction and an external filter eliminated any possibility of conditions being established for signal generation by the tunnel diode, whose natural generation frequency was 1–2 GHz. The current–voltage characteristic of the tunnel diode was determined using a cathode-ray curve tracer with a sweep frequency of 10 kHz. As has been noted, the range of variation of the applied bias voltages in the absence of a microwave signal fell within the linear section of the current–voltage characteristic.

Figure 1 gives experimental results obtained by measuring the current–voltage characteristics of a tunnel diode for various currents through the diode without (curves *1*) and with external microwave power being applied (curves *2*). When the currents through the diode were less than half the peak current I_n, which was 22.6 mA for this particular diode, no descending section appeared on the current–voltage characteristic for any applied microwave power up to the maximum of 1.6 W used in these experiments. In this case, the current–voltage characteristic of the diode ''shifted'' toward higher positive voltages as the external microwave signal power increased (Fig. 1a).

For currents I through the diode in the range $I_n/2<I<I_n$, when an external microwave signal was applied a section of negative differential resistance appeared on the current–voltage characteristic above certain power levels and as the current through the diode increased, the descending section appeared at lower microwave powers (b —

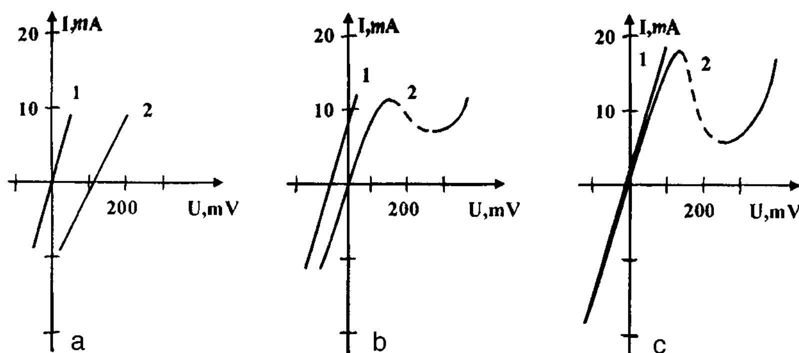

FIG. 1. Current–voltage characteristics of a tunnel diode for various currents through the diode without a microwave signal (curves *1*) and with an applied external microwave signal (curves *2*) at various powers (a — 1600 mW, b — 300 mW, and c — 2 mW).

 © 1999 American Institute of Physics

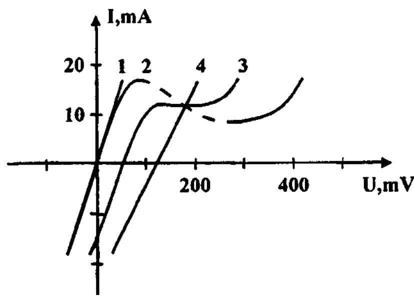

FIG. 2. Current–voltage characteristics of a tunnel diode at various powers of the external microwave signal: *1* — 0 mW, *2* — 2 mW, *3* — 200 mW, and *4* — 1200 mW.

300 mW, c — 2 mW). As the applied microwave power increased, the section of negative differential resistance disappeared and above a certain microwave power (in this case 1.2 W), the current–voltage characteristic of the tunnel diode again became almost linear (Fig. 2) for any initial current through the diode.

For chains of two or three series-connected tunnel diodes, whose current–voltage characteristic in the absence of a microwave signal contains two or three descending sections, respectively, the action of an external microwave signal also resulted in the appearance of descending sections on sweeping over the linear section of the characteristic. It was established experimentally that as the external microwave signal power increased, the current–voltage characteristic of a chain of series-connected tunnel diodes initially showed sections of negative differential resistance whose order and number depended on the ratio of the dc resistances of the diodes and the current through the diodes in the absence of the microwave signal. Then the descending sections gradually disappeared, beginning with the one at high voltages, and the characteristic became close to linear.

The appearance of a section of negative differential resistance on the current–voltage characteristic of tunnel diodes exposed to microwave action and with an applied bias below the peak voltage has been confirmed experimentally at signal frequencies between 25 and 140 GHz.

To conclude, it has been shown that when tunnel diodes forward-biased to voltages below the peak are exposed to microwave radiation, their current–voltage characteristics, which are almost linear in the absence of the microwave signal, may exhibit sections of negative differential resistance.

[1] D. A. Usanov, B. N. Korotin, V. E. Orlov, and A. V. Skripal', Pis'ma Zh. Tekh. Fiz. **16**(8), 50 (1990) [Sov. Tech. Phys. Lett. **16**, 303 (1990)].
[2] D. A. Usanov, A. V. Skripal', B. N. Korotin, and V. E. Orlov, Pis'ma Zh. Tekh. Fiz. **19**(7), 81 (1993) [Tech. Phys. Lett. **19**, 220 (1993)].

Translated by R. M. Durham

Nonequilibrium effects accompanying condensation at a black sphere

M. Yu. Plotnikov and A. K. Rebrov

Institute of Heat Physics, Siberian Branch of the Russian Academy of Sciences, Novosibirsk

(Submitted May 25, 1998)
Pis'ma Zh. Tekh. Fiz. **25**, 43–48 (January 26, 1999)

A Monte Carlo simulation is used to make a detailed analysis of the nonequilibrium zone formed near the surface of a condensing sphere. Significant directional anisotropy of the temperature was observed. It was established that the nonequilibrium near an absolutely black sphere is responsible for the difference between the calculated values of the specific mass flow in comparison with the published data obtained assuming little difference between the vapor state at infinity and temperature saturation conditions at the surface of the sphere. © *1999 American Institute of Physics.* [S1063-7850(99)02401-5]

Condensation–evaporation processes at the surface of a droplet have been studied over the last few decades because of their important applications and interest in nonequilibrium vapor states at the surface. Although condensation models have been constructed for small differences between the vapor state at infinity and conditions of surface temperature saturation,[1,2] the structure of the Knudsen layer has been very little studied even for these conditions.

Here we report results of a direct statistical modeling of condensation at the surface of an absolutely black sphere, i.e., in the limiting case when the temperature of the droplet surface can be taken to be zero and the departure from equilibrium is thus maximized. Conditions close to condensation at an absolutely black sphere occur when severely cooled droplets enter a gas which condenses onto their surface with condensation coefficients close to unity.

The authors only know of one study dealing with condensation at an absolutely black sphere (the problem of an ideal sink).[3] The results of this study can be used to assess the general behavior of the macroscopic parameters, which are qualitatively consistent with the results of solving the Navier–Stokes equations.

The method of direct statistical modeling,[4] which has no constraints on the form of the boundary conditions, can yield data on the evolution of the molecular velocity distribution function when vapor flows onto a sphere at any point. To give a clear representation of the flow structure, we use a definition of the temperatures in terms of the coordinates and the dimensionless flow velocity in Mach number form.

Let us assume that the sphere has radius r_0 and the temperature and gas density at infinity (T_∞, n_∞) are given. The condensation process is a function of the parameters T_∞, n_∞, and the Knudsen number $\mathrm{Kn}=l/r_0$. Here l is the mean free path of the molecules at infinity: $l=1/(\sqrt{2}n_\infty\sigma)$, where σ is the collision cross section for the vapor molecules.

In the calculation scheme used for the direct statistical modeling a sphere of radius r_0 was surrounded by a spherical shell of radius R_0, which was set at the largest value possible when a Pentium computer was used for the calculations. In the range of Knudsen numbers between ∞ and 0.01, the calculations included up to 5×10^5 molecules for a hard-sphere interaction potential. This allowed us to make a detailed analysis of the flow structure for a particular Knudsen number with the parameters for the outer shell differing only slightly from those at infinity. For a given uniform distribution of the parameters in the spherical layer, condensation was ''initiated'' at the surface of the sphere and steady-state flow developed in the course of the modeling. This steady-state flow was then used as the basis to calculate the required flow macroparameters.

Figure 1a shows a typical distribution of the parameters at a condensing sphere for transition regimes for the case Kn = 0.1. Here and subsequently, the temperatures $T_\parallel, T_\perp$, and $T=(T_\parallel+2T_\perp)/3$ (i.e., the temperatures parallel and perpendicular to the radius, and the total temperature) are given relative to that at infinity. The Mach number was determined using the total temperature T, including that in the vicinity of the condensing sphere, where this definition can be considered to be arbitrary but permissible for a qualitative sink-type of flow acceleration characteristic.

The drop in temperature T near the sphere presents no problems, since this reflects the acceleration of the flow and the transfer of heat to the sphere ($T_s=0$). The drop in the temperature $T_\parallel$ requires no qualitative explanation. The increase in the temperature $T_\perp$ above that at infinity was characteristic and unexpected. This effect cannot be treated unilaterally as nonequilibrium. It is caused by a flow of gas to an object of bounded dimensions comparable to the mean free path, when the energy of directional motion in a selected tube of flow is transferred not only to the object but also to its surrounding gas sheath outside the tube of flow. The unexpected increase in the total temperature above that at infinity should also be noted. This effect is clearly impossible in the one-dimensional case of condensation at a planar surface. This effect does not occur even for condensation on a sphere with Kn = 0.01 (Fig. 1b).

Figure 1c shows the distribution of the parameters for the case Kn = 1. The qualitative temperature behavior differs little from the preceding case. We merely note a significant reduction in the size of the nonequilibrium zone (in mean free path lengths) compared with Figs. 1a and 1b. Additional numerical experiments showed that the increase in

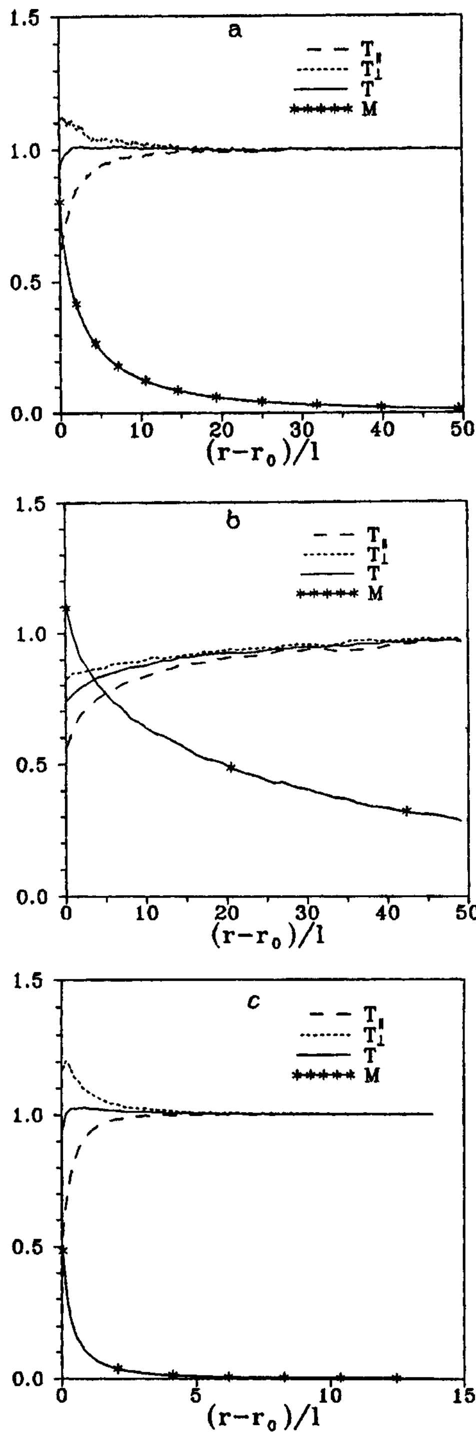

FIG. 1. Temperature distribution for different directions and Mach number for Kn = 0.1 (a), Kn = 0.001 (b), and Kn = 1 (c).

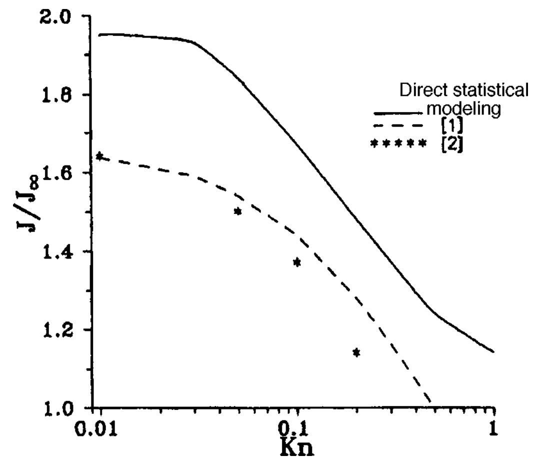

FIG. 2. Relative specific mass flow J/J_∞ as a function of Knudsen number for data obtained by direct statistical modeling.[1,2]

the total temperature above T_∞ has a peak in the range of Knudsen numbers between 0.1 and 1. As the Knudsen number increases further, this effect becomes less defined, which can evidently be explained by a reduction in the mass flow to the sphere.

It can be seen from Fig. 1 that as the Knudsen number decreases from 1 to 0.01, the gas velocity near the surface becomes supersonic, at any temperature. Without discussing the arbitrary nature of the definition of the Mach number near the surface, we note that the translational nonequilibrium becomes appreciable at relatively low subsonic velocity, i.e., in the range of Knudsen numbers greater than 0.01, substantial acceleration of the flow is observed in the nonequilibrium region.

This evolution of the zone of strong nonequilibrium as the Knudsen number increases from 0.01 to 1 is consistent with the dependence of the relative specific mass flow J/J_∞ on the Knudsen number plotted in Fig. 2. Here $J_\infty = 1/4 n_\infty V_\infty$ is the specific mass flow to the surface when $\mathrm{Kn} \to \infty$, $V_\infty = \sqrt{8RT_\infty/\pi}$, and R is the gas constant. These data indicate in particular that the maximum variation in the flow rate corresponds to a zone of substantial flow rearrangement where the thermal energy of the gas is slightly higher than the thermal energy at infinity, an effect familiar from studies of the shock wave structure in a gas. Existing condensation models[1,2] give underestimates of J/J_∞ for condensation conditions at an absolutely black sphere.

This investigation has shown that substantial departure from equilibrium exists near an absolutely black sphere, causing the values of J/J_∞ to differ from those[1,2] obtained assuming that the vapor state at infinity differs little from the conditions of temperature saturation at the surface of an absorbing sphere.

[1] K. Yamamoto and T. Nishitani, in *Proceedings of the 14th International Symposium on Rarefied Gas Dynamics*, 1984, Vol. II, edited by H. Oguchi, pp. 893–900.

[2] G. F. Humber and U. M. Tituluaer, in *Proceedings of the 17th International Symposium on Rarefied Gas Dynamics*, 1990, edited by E. Beilich, pp. 1266–1273.

[3] V. N. Gusev and A. V. Zhbakova, Izv. Akad. Nauk SSSR. Ser. Mekh. Zhidk. Gaza No. 3, 109 (1968).

[4] G. A. Bird, *Molecular Gas Dynamics and the Direct Simulation of Gas Flows* (Clarendon Press, Oxford, 1994), 458 p.

Translated by R. M. Durham

Heterodyne photoelectric signal conversion in periodic transmission lines using Mott diodes

N. M. Ushakov

Institute of Radio Engineering and Electronics, Russian Academy of Sciences, Saratov Branch
(Submitted April 1, 1998)
Pis'ma Zh. Tekh. Fiz. **25**, 49–54 (January 26, 1999)

A description is given of a principle for constructing optoelectronic delay lines in optical information processing systems which can be implemented for various important devices. © *1999 American Institute of Physics.* [S1063-7850(99)02501-X]

A whole range of information processing devices such as various types of delay lines, convolvers, and correlators require a delayed microwave signal. In these devices a signal time delay needs to be introduced either without varying its amplitude spectrum or by varying this spectrum so that the pulse length is reduced (dispersion delay line). The theory of linear signal response based on the shift theorem indicates that a time shift or signal delay can be achieved if all its spectral components acquire a corresponding additional phase shift.[1] In planar Mott-diode periodic transmission lines, which were first proposed by Ushakov *et al.*,[2] the required phase shift is implemented automatically and depends on the central frequency of the microwave signal spectrum. Thus, these new devices may form the basis for constructing optoelectronic delay lines for various purposes in optical information processing systems.

The present paper describes more general laws governing the heterodyne photoelectric excitation and delay of microwave signals in Mott-diode planar periodic transmission lines.

A method of heterodyne detection of signals by a photodetector, based on quadratic conversion of the radiation field, is widely used in optical interferometry and spectroscopy,[3] and also in optical information processing systems.[4] This method is also of interest for the photoelectric excitation of microwave signals in periodic transmission lines because of the independent control of the interacting optical fields. This will be explained through an example. Assume that there are two interacting optical signals written in the scalar form $E_1(r,t)=E_{01}(r)\exp(j\omega t)$ and $E_2(r,t)=E_{02}(r)\times\exp(j(\omega\pm\Delta\Omega)t+\phi(r))$ with frequencies ω and $\omega\pm\Delta\Omega$. As a result of their summation at the photosensitive area of the photodiode array, a response appears in the electrical circuit in the form of the "useful" photocurrent component:

$$\dot{I}_{\text{ph}}(r,V_0,t)=2(\eta(V_0)q/h\nu)E_1^*E_2(r,t)\exp(j\Delta\Omega t+\phi(r)), \tag{1}$$

where E_1^* and $E_2(r,t)$ are the complex-conjugate amplitudes of the interacting optical fields, $\phi(r)$ is the phase difference of the complex amplitudes, $\eta(V_0)$ is the quantum efficiency of photoelectric conversion, q is the electron charge, V_0 is the photodiode displacement voltage, h is Planck's constant, and $\nu=\omega/2\pi$ is the optical signal frequency.

Relation (1) indicates that the photoresponse of the photodiode array in the heterodyne detection regime can be controlled using three independent parameters $E_1(r,t)$, $E_2(r,t)$, and $\phi(r)$ which characterize the interacting optical fields.

It is well known that periodic transmission lines, periodic waveguiding systems, and delay lines are essentially the same devices, designed to delay the signal in time and provide a frequency-dependent phase shift.[5] In the quasistatic approximation, when the signal wavelength is much greater than the characteristic dimensions of the transmission line, these new Mott-diode optoelectronic periodic transmission lines can be represented as multilink chains of identical quadrupoles. Each link of the chain is then an active quadrupole such as a low-pass filter (Fig. 1a) or a high-pass filter (Fig. 1b). Figure 1c shows the equivalent circuit of two opposed Mott diodes in the form of a planar multielement periodic Mott-barrier structure of the interdigital or anti-spiral type.[6] Assuming that the active quadrupole can be replaced by a passive quadrupole with additional external sources in the primary and secondary circuits whose electromotive forces are equal to the voltages at the open terminals of the active quadrupole,[7] the equivalent circuit in Fig. 1c can be simplified. In the equivalent circuits shown in these figures the following notation is introduced: $\dot{X}_L=\dot{G}_L^{-1}=j\Omega L$ is the inductive reactance and $\dot{G}_c=\dot{X}_c^{-1}=j\Omega C$ is the capacitive susceptance. Since $\dot{G}_0=\dot{I}_{\text{ph}}/V_0$, the expression for the susceptance $\dot{G}_0$ with allowance for formula (1) has the form

$$\dot{G}_0=2(\eta q/V_0 h\nu)E_1^*E_2(r,t)\exp(j\Delta\Omega t+\phi(r)). \tag{2}$$

In the theory of O-type vacuum microwave devices, a physical concept such as the radiation resistance or conductance is widely used, characterizing the efficiency of excitation of the signal in the delay line as a result of interaction between the electron beam and the field of the slowed electromagnetic wave. By analogy, it is suggested that the susceptance $\dot{G}_0$ given by formula (2) should also be called the radiation conductance of the optoelectronic interaction.

We study the general case in which a mixed optical signal is supplied to each component of the delay line in the modulation band $\Delta\Omega$ with the phase shift $\phi(r)$, which is equal to the phase shift of the microwave signal per unit cell of the delay line $\Psi_0(\Omega)$. As a result of homodyne detection

 © 1999 American Institute of Physics

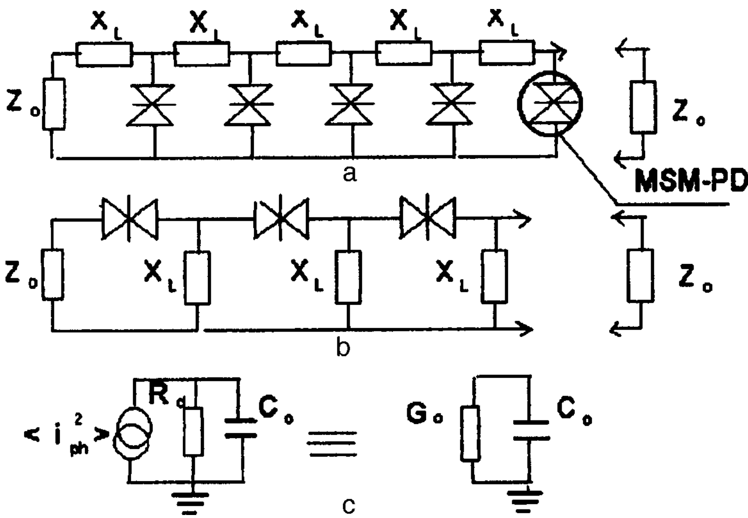

FIG. 1.

of the optical signal in the Mott-barrier structure, a microwave signal is excited within this band and propagates in the delay line as a traveling wave. At each unit cell in the transmission line, this signal acquires the phase shift $\Psi_0(\Omega) = \Omega t_{tr} + \theta_0(\Omega)$, where Ωt_{tr} is the phase shift caused by the finite transit time for the majority carriers of the interdigital gap in the Mott-barrier structure (t_{tr} is the transit time) and $\theta_0(\Omega)$ is the phase shift per unit cell in the delay line. The dispersion relation for a lossless low-pass (high-pass) filter has the form

$$\theta_0 = 2 \arcsin(\Omega/\Omega_0)^m, \quad (3)$$

where $m=1$ for a low-pass filter and $m=-1$ for a high-pass filter. Then, knowing that $\Omega t_{tr} = 2.4$ and $\arcsin(x) \approx x$ for the phase shifts $f = \Omega/2\pi \leqslant 0.4 f_0$ (low-pass filter) or $f \geqslant 2.5 f_0$ for a high-pass filter, we obtain the approximate spatial phase-matching condition:

$$\phi(r) = \Psi_0(\Omega) = 2.4 + 2(\Omega/\Omega_0)^m. \quad (4)$$

The delay time t_d of the microwave signal in the delay line with allowance for Eq. (4) is given as

$$t_d = Np/v_{ph} = N\Psi_0(\Omega)/\Omega, \quad (5)$$

where N is the number of unit cells in the delay line, v_{ph} is the phase velocity of the microwave signal in the delay line, and p is the length of a unit cell of this system.

Figures 2a and 2b give the time delay for a delay line cutoff frequency of 6 GHz in the frequency range $f = \Omega/2\pi \leqslant 2.4$ GHz for the low-pass filter and $f = \Omega/2\pi \geqslant 15$ GHz for a high-pass filter, plotted as a function of the reduced frequency $a = \Omega/\Omega_0$. These time delays indicate that optoelectronic delay lines are a good supplement to acoustic delay lines with conventional time delays longer than 1 μs. Unlike Ref. 2, where the photoelectric conversion process takes place in series from one cell to another in the delay line, in our case this process takes place in parallel, which enhances the controllability of the homodyne photoelectric conversion process in the delay line. By varying the spatial coordinates of the optical signal using an electromechanical scanner (for example, using a bimorphic mirror), it is possible to control the time delay of the microwave signal in the delay line.

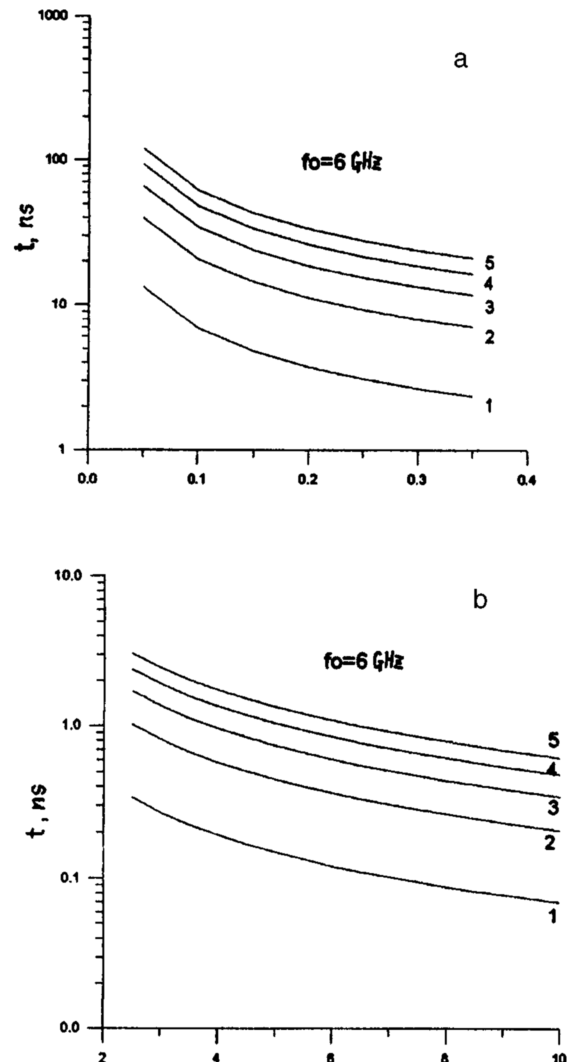

FIG. 2.

To conclude, the proposed principle for phase matching between the optical signal and the microwave signal excited in the delay line can be applied to various important optical information processing devices where a controllable signal time delay is required.

[1] F. T. S. Yu, *Introduction to Diffraction, Information Processing, and Holography* (MIT Press, Cambridge, Mass., 1973).
[2] N. M. Ushakov and V. I. Petrosyan, in *Proceedings of the International Scientific and Technical Conference on Topical Problems in Electronic Instrument Manufacture, APÉP-92*, Novosibirsk, Russia, 1992, Vol. 6 [in Russian], p. 15.
[3] V. V. Protopopov and N. D. Ustinov, *Laser Heterodyning* [in Russian], Moscow (1985), 288 pp.
[4] T. M. Terpin, Proc. IEEE **69**, 92 (1981).
[5] Sh. Élashi, IEEE **64** (1976).
[6] N. M. Ushakov and V. I. Petrosyan, Pis'ma Zh. Tekh. Fiz. **22**(14), 60 (1996) [Tech. Phys. Lett. **22**, 582 (1996)].
[7] L. R. Neĭman and K. S. Demirchyan, *Theoretical Principles of Electrical Engineering*, 2 Vols. [in Russian] (1967), Ch. 1, 522 pp.

Translated by R. M. Durham

TECHNICAL PHYSICS LETTERS VOLUME 25, NUMBER 1 JANUARY 1999

Enhancement of the efficiency of *i–n*-GaN light-emitting diodes by electrochemical etching

V. G. Sidorov, A. G. Drizhuk, M. D. Shagalov, D. V. Sidorov, and A. S. Usikov

Vologda Polytechnic Institute

(Submitted July 2, 1998)
Pis'ma Zh. Tekh. Fiz. **25**, 55–60 (January 26, 1999)

An investigation was made of the electrochemical etching of *i–n*-GaN light-emitting diode structures in aqueous solutions of KOH and NaOH to remove parasitic low-resistivity layers and inclusions in the structures which shunt the active current flow channels through the structures and lower the electroluminescence intensity. The electroluminescence intensity of the structures increased by two or three orders of magnitude during the etching process.
© *1999 American Institute of Physics.* [S1063-7850(99)02601-4]

Etching of semiconductor materials and device structures is used at all stages of the fabrication of semiconductor devices. One of the most important operations is known as (post-etching), i.e., etching the finished device structures before protective coatings are applied or before hermetic sealing. The aim of this operation is to remove any contaminants from the surface of the structure and to reduce and stabilize the surface recombination velocity, which reduces the leakage currents and enhances the efficiency and operating stability of the fabricated devices. Aqueous solutions of acids, alkalis, or salts are used most frequently as etchants. The methods used are chemical or electrochemical etching.

Unlike many other semiconductors, gallium nitride has an extremely high chemical stability. It barely dissolves in acids or alkalis even at high temperatures. Gallium nitride can only be etched using melts of alkalis and various salts.[1] However, this type of etching damages any masking coating as well as the substrate, and is not suitable for GaN layers and structures. At present, no efficient aqueous etchants operating at room temperature are available for GaN. Thus, dry etching methods[2] are mainly used to produce the required geometric relief in GaN structures during the fabrication of devices.

The search for possible treatments of GaN crystals using aqueous etchants is currently being intensively pursued.[3–10] As yet, perhaps the only method of achieving fairly rapid dissolution of GaN at room temperature is electrochemical etching in dilute alkalis.[1,7,8] Photochemical etching of GaN is also carried out using dilute alkalis and at room temperature, but under intensive illumination by natural light.[3,6] The mechanism for GaN dissolution in this method of etching is broadly similar to electrochemical etching. The only difference is that the free carriers involved in the etching process are not supplied to the surface of the sample being etched by an electric field but are generated near the surface by natural light. Photoelectrochemical etching[9] combines both these methods.

In electrochemical etching GaN dissolves selectively, with the highest rate at sites where the largest currents flow, i.e., in regions of the crystal possessing the most defects and highest conductivity. Thus, electrochemical etching can be used to identify electrical and structural inhomogeneities in epitaxial layers and GaN structures. Moreover, this method of etching can be used to enhance the electroluminescence efficiency of *i–n*-GaN light-emitting diode structures, which is the subject of the present Letter.

Emitting *M–i–n*-GaN structures are a type of metal–insulator–semiconductor structure. The dielectric region of the structure is fabricated as a semi-insulating *i*-layer made of heavily compensated GaN. The compensating impurity is selected so that it is also an efficient radiating center.

The electroluminescence of the *i–n* structure is excited in the *i*-layer. The excitation mechanism involves the acceleration of majority and nonequilibrium carriers in the strong electric field of the *i*-layer to energies sufficient for ionization or impact excitation of luminescence centers. Nonequilibrium carriers appear in the *i*-layer as a result of tunneling or impact ionization of impurities or atoms of the GaN crystal. In this case, the simplest method of enhancing the electroluminescence efficiency is to increase the concentration of "hot" carriers by increasing the electric field strength in the *i*-layer. However, this is impeded by the fundamental inhomogeneity of GaN epitaxial layers.

Epitaxial GaN layers typically grow as closely intergrown unidirectional blocks. Since the crystal has this block property, impurities and structural defects are distributed nonuniformly over the surface and over the layer thickness. The distribution of these inhomogeneities correlates closely with the distribution of the spectral characteristics and the luminescence intensity over the sample.[7] Nonuniform doping of the *i*-layer gives rise to low-resistivity microinclusions during growth, including penetrating conducting channels. These inclusions shunt the *i*-layer, reducing the electroluminescence efficiency. This efficiency would obviously be enhanced if the conducting inclusions in the *i*-layer could be removed in some way.

Emitting *i–n*-GaN structures, oriented in the (11–20) plane, were grown on (10–12) sapphire substrates by vapor-phase epitaxy using a chloride–hydride system. First a low-resistivity undoped *n*-GaN layer was grown at 1050 °C.

 © 1999 American Institute of Physics

Then, a high-resistivity *i*-region was grown at 950 °C, consisting of two layers to spatially separate the region of strong field and the region of electroluminescence generation. The inner layer of the *i*-region was doped with both zinc and oxygen. The surface layer had a higher resistivity than the GaN(Zn,O) layer and was only doped with zinc. Pale blue electroluminescence with a maximum at 2.55 eV was excited in the *i*-GaN(Zn,O) layer. As a result of the asymmetry of the structure, electroluminescence was only excited when the voltage at the contact to the *i*-GaN(Zn) layer was negative.[11]

The growth conditions for $i-n$-GaN structures were such that the final stage of the process always involved the growth of a thin ($\sim 0.1\,\mu$m) highly conducting *n*-GaN(Zn) layer on the surface of the *i*-layer. That is to say, all the structures grown in this way were in fact $n-i-n$-type structures. The surface conducting *n*-GaN(Zn) layer and the low-resistivity inclusions in the *i*-layer, which we discussed above, increase the currents flow and the leakage currents in the structures, shunt the *i* layer, and reduce the electroluminescence efficiency. Moreover, electroluminescence can only be excited in the pulsed mode. At dc current thermal breakdown of the structure usually occurs before the electroluminescence threshold is reached.

The $i-n$-GaN structures were etched electrochemically using a (0.1–0.2)N aqueous solution of KOH or NaOH at 300 K and current density (0.05–0.1) A/cm^2. A positive potential was applied to a contact on the surface of the structure, which was protected with a chemically resistant varnish, and a negative potential applied to the electrolyte. The voltage on the structure was selected with the electroluminescence threshold in mind, which was determined under pulsed excitation and remained constant during the etching process. The gallium hydroxide formed on the GaN surface during etching blocks any further dissolution of the GaN. In order to avoid this and to dissolve the gallium hydroxide, a small amount of HCl was added to the electrolyte.

Current initially flows mainly through the conducting *n*-GaN(Zn) surface layer which dissolves. After this layer has dissolved, the positive contact potential is shorted through the *i*-layer to the underlying layer of conducting undoped *n*-GaN and again across the *i*-layer to the negative electrolyte potential which has the same polarity as the electroluminescence excitation in the structure. Most of the current flows through the conducting inclusions in the *i*-layer. As these are etched, an increasing fraction of the current flows through the high-resistivity active region of the *i*-layer. This leads to a gradual rise in electroluminescence (see Fig. 1) whose intensity can be monitored visually or using a photodetector. The etching process must be stopped when the electroluminescence intensity reaches saturation otherwise the undoped *n*-GaN layer beneath the *i*-layer will dissolve. This reduces the electroluminescence intensity and sections of the *i*-layer also begin to peel off. The total etching time before the electroluminescence reaches a maximum is 1–3 min. Its intensity increases by two or three orders of magnitude during etching, and the $i-n$-GaN structures become suitable for fabricating light-emitting diodes with acceptable parameters for practical purposes.[12]

This work was supported by the Federal Target Program "Integration," Project No. 75, and was also partially supported by the University of Arizona.

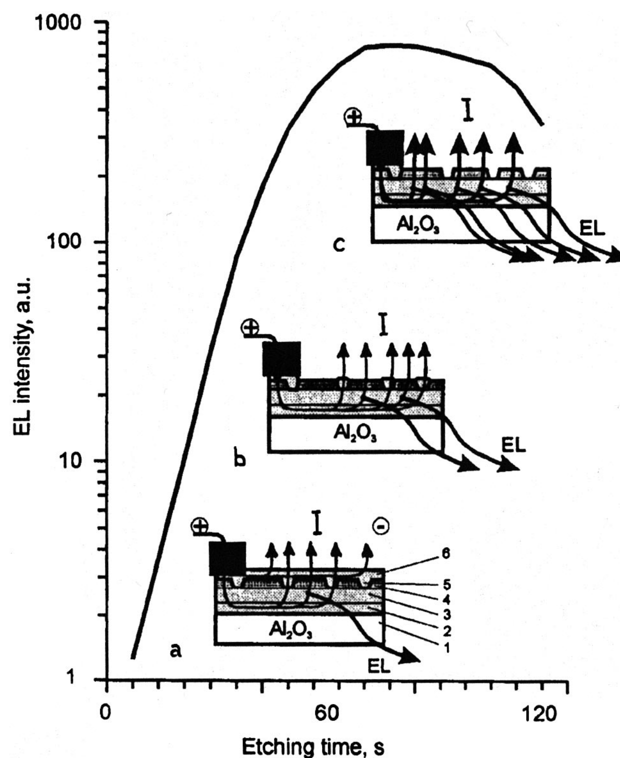

FIG. 1. Intensity of pale blue electroluminescence of $i-n$-GaN structure as a function of etching time. Insets: a, b, c — structure at different stages of etching: *1* — sapphire substrate, *2* — layer of conducting *n*-GaN, *3* — active *i*-GaN(Zn,O) layer, *4* — high-resistivity *i*-GaN(Zn) layer, *5* — low-resistivity *n*-GaN(Zn) inclusions in *i*-GaN(Zn) layer, *6* — low-resistivity *n*-GaN(Zn) layer; the current lines (I) through the structure are shown and the electroluminescence flux is also shown schematically by the lines marked EL.

[1] J. J. Pankove, J. Electrochem. Soc. **119**, 1118 (1972).
[2] J. C. Zolper and R. J. Shul, Mater. Res. Bull. Feb. 1997, 36.
[3] M. S. Minsky, A. M. White, and E. L. Hu, Appl. Phys. Lett. **68**, 1531 (1996).
[4] J. R. Mileham, S. J. Peatron, C. R. Abernathy, J. D. Mackenzie, R. J. Shul, and S. P. Kilcoyne, J. Vac. Sci. Technol. A **14**, 836 (1996).
[5] C. V. Vartuli, S. J. Peatron, J. W. Lee, C. R. Abernathy, J. D. Mackenzie, J. C. Zolper, R. J. Shul, and F. Ren, J. Electrochem. Soc. **143**, 3681 (1996).
[6] C. YontSey, I. Adesida, and G. Bulman, Appl. Phys. Lett. **71**, 2151 (1997).
[7] M. Ohkubo, in *Proceedings of the Second International Conference on Nitride Semiconductors — ICNS'97*, Tokushima, Japan, 1997, pp. 2–24, 284.
[8] M. Ohkubo, Jpn. J. Appl. Phys., Part 2 **36**, L955 (1997).
[9] T. Rotter, D. Uffmann, J. Ackermann, J. Aderhold, J. Stemmer, and J. Graul, Proc. Mater. Res. Soc. **482**, 1003 (1998).
[10] F. A. Ponce, Mater. Res. Bull. Feb. 1997, 51.
[11] A. G. Drizhuk and V. G. Sidorov, Fiz. Tekh. Poluprovodn. **20**, 144 (1986) [Sov. Phys. Semicond. **20**, 87 (1986)].
[12] A. G. Drizhuk, M. V. Zaitzev, V. G. Sidorov, and D. V. Sidorov, in *Compound Semiconductors: Proceedings of the 23rd International Symposium on Compound Semiconductors*, St. Petersburg, Russia, 1996, Inst. Phys. Conf. Ser. No 155, edited by M.S. Shur and R.A. Suris (Institute of Physics Press, Bristol, 1997), Chap. 4, p. 401.

Translated by by R. M. Durham

Modification of the tip shape of a scanning probe microscope using ion sputtering

G. V. Dedkov and S. Sh. Rekhviashvili

Kabardino–Balkar State University, Nalchik

(Submitted April 8, 1998; resubmitted September 8, 1998)
Pis'ma Zh. Tekh. Fiz. **25**, 61–67 (January 26, 1999)

The process of ion sputtering of the tip of a scanning probe microscope is modeled to determine the conditions for the formation of protrusions at the apex of the tip. It is shown that for an isotropic sputtering process sharper protrusions form at the apex of a conical tip if the initial radius of curvature of the tip is not too large and the angular dependence of the sputtering coefficient has a fairly sharp peak at angles of incidence of 60–70°. © *1999 American Institute of Physics.* [S1063-7850(99)02701-9]

The problem of modifying and monitoring the tip shape of scanning probe microscopes (including atomic force, tunneling, and friction microscopes) is a vitally important one, since the increasingly widespread application of a new generation of these devices as precision measuring instruments means that the real shape and atomic structure of the sensitive element, i.e., the tip, must be taken into account. The tip shape is most commonly determined using electron transmission microscopy.[1]

Electrochemical etching[2–4] or ion sputtering[5–7] is used to modify (sharpen) the apex part of the tip. For instance, Vasile *et al.*[5] sputtered wire made of tungsten and a platinum–iridium alloy using a 0.4 μm diameter Ga^+ ion beam. In most cases, the end of the wire facing the beam acquired a conical shape with an opening angle of 8–10° but in some cases, flat-ended cylindrical protrusions appeared. The radii of curvature of the protrusions were 1–5 nm.

The present study is a continuation of Ref. 8, in which we proposed a method of determining the tip shape of a probe microscope by using backscattering spectroscopy. Our aim is to study the evolution of the tip shape by modeling the sputtering process and determining the physical conditions promoting the formation of protrusions. Note that both operations (sputtering and shape monitoring) can be carried out in the same vacuum chamber by varying the orientation of the beam.[8]

In order to solve this problem, we consider a homogeneous model of a silicon tip whose initial shape is a paraboloid of revolution of height H and radius of curvature R at the apex section. The orientation of the incident beam B relative to the tip is shown schematically in Fig. 1.

It has been established experimentally that the angular dependence of the sputtering coefficient has a maximum for angles of incidence of 60–85° (Ref. 9) and thus for the numerical calculations the corresponding function $K(\alpha)$, where the angle α is measured from the normal to the surface, was approximated by

$$K(\alpha)=K_0\left[\exp\left(-\frac{(|\alpha|-\alpha_0)^2}{2\sigma_1^2}\right)\theta(\alpha_0-|\alpha|)+\exp\left(-\frac{(|\alpha|-\alpha_0)^2}{2\sigma_2^2}\right)\theta(|\alpha|-\alpha_0)\right], \quad (1)$$

where K_0, α_0, σ_1, and σ_2 are the model parameters and

$$\theta(x)=\begin{cases}1, & x\geqslant 0,\\ 0, & x<0.\end{cases}$$

The angle α_0 corresponds physically to the maximum of the angular dependence of the sputtering coefficient and the parameters σ_1 and σ_2 characterize its slope on either side of the maximum.

The approximation (1) can take into account the main characteristics of the sputtering coefficient (Fig. 2): the existence of a peak, a fairly slow ascending section on the left, and a sharply descending section on the right. The crosses give the experimental values[9] of the sputtering coefficient for Ar^+-SiO_2 (32 keV beam energy), the model function (1) for the parameters $K_0=3$, $\sigma_1=0.65$ rad, and $\sigma_2=0.133$ rad, and the theoretical dependence[10] $K(\alpha)=1/\cos\alpha$ (dashed curve) to the left of the peak.

For a homogeneous target the rate of sputtering of the planar boundary in the normal direction is

$$\Delta x/\Delta t=\frac{IK(\alpha)\cos(\alpha)}{n}, \quad (2)$$

where I is the ion beam intensity and n is the volume concentration of target atoms. Assuming that $\Delta x=I\Delta t/n$, we can trace the evolution of the shape of a tip of arbitrary initial shape, by dividing its surface area into a finite number of quasiplane sections. For our calculations we assumed that $\Delta x=0.05$ nm, $H=1000$ nm, and the initial radii of curvature R and the angles α_0 varied.

The results of the modeling for different initial conditions are plotted in Figs. 3–5. Curves *1–4* correspond to the

 © 1999 American Institute of Physics

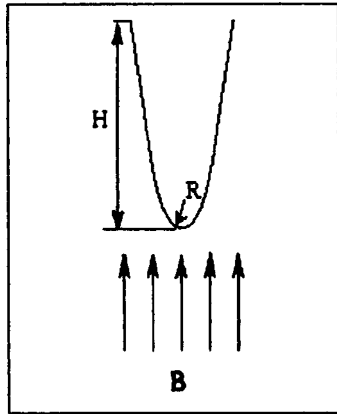

FIG. 1. Schematic showing ion beam treatment of a probe microscope tip.

initial tip shape after 500, 1000, and 2000 ''sputtering steps,'' respectively. The values of the parameters σ_1 and σ_2 for all cases are the same as those in Fig. 2.

It can be seen that protrusions only begin to appear at the apex of the tip for angles $\alpha_0 < 80°$ and are formed earliest for smaller values of R (compare Figs. 4a and 4b). The radii of curvature of the protrusions are approximately an order of magnitude smaller than R. For $\alpha_0 = 60°$ (Fig. 3) protrusions are observed for all values of R between 10 and 100 nm but for $\alpha_0 = 70°$, they only appear for $R = 10$ and 50 nm, and for $\alpha_0 = 80°$ (and above) they do not appear at all (Fig. 5). A further increase in the sputtering time does not change these conclusions. For $\alpha_0 > 80°$ no protrusions are observed even for $R < 10$ nm (these curves are not given). For $\sigma_1 = \sigma_2$, when the function $K(\alpha)$ is symmetrical, again no protrusions appear.

Under longer treatment the side surface of the protrusions becomes cylindrical and the apex flattens out. In cases where no protrusions form, the shape of the tip tends to conical with time, with an opening angle close to $\pi - 2\alpha_0$.

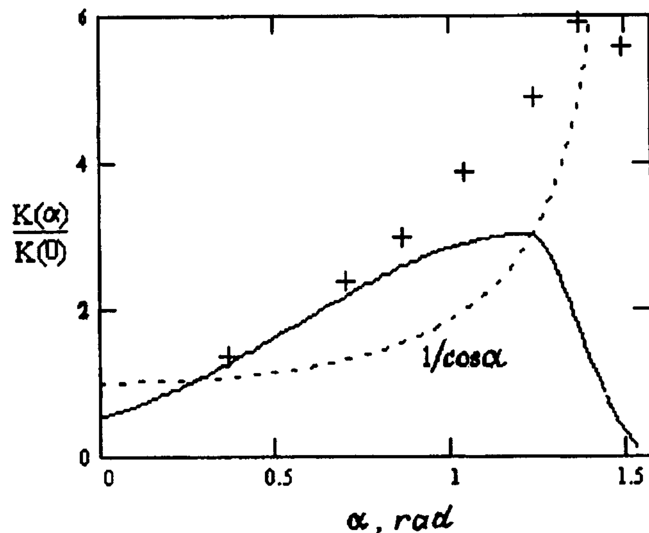

FIG. 2. Angular dependence of the sputtering coefficient. Solid curve — model function (1) for $\alpha_0 = 70°$, $K_0 = 3$, $\sigma_1 = 37°$, $\sigma_2 = 8°$; crosses — experimental values[9] for $Ar^+ - SiO_2$ sputtering (32 keV); dashed curve — theoretical dependence $1/\cos\alpha$ (Ref. 10).

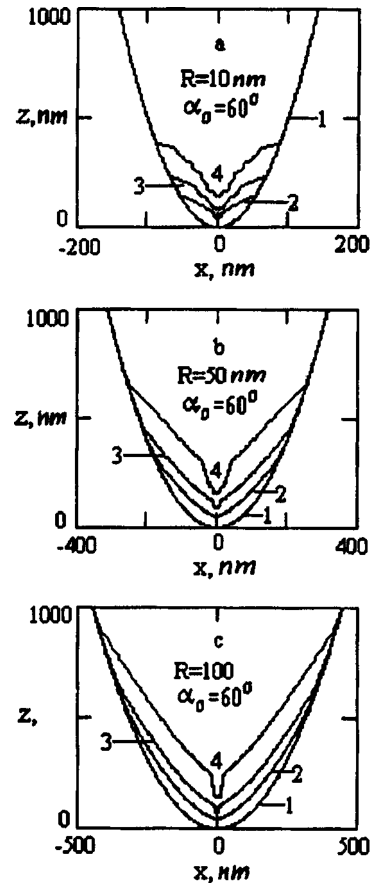

FIG. 3. Evolution of tip shape sputtered by an ion beam for various angles corresponding to the maximum sputtering coefficient, and initial radius of curvature of parabaloid. The curves numbered 1–4 correspond to the initial tip shape after 500, 1000, and 2000 sputtering steps, respectively.

This is consistent with the theoretical estimates given by Carter *et al.*[11] and with the experimental results reported by Hasuyama *et al.*[12] who treated a ''thick'' 100 μm diameter copper wire.

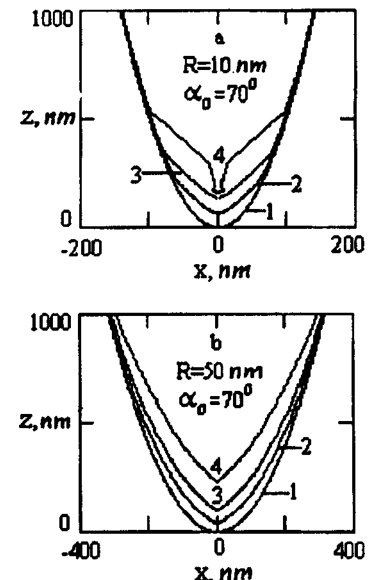

FIG. 4.

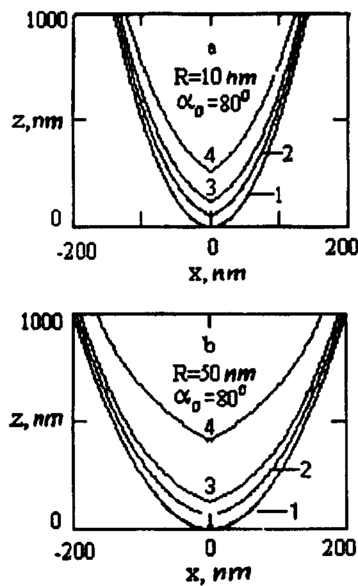

FIG. 5.

The figures also show that the tip has a rougher surface for $\alpha_0 = 60°$, whereas for larger angles the surface is smoother. This is because when the maximum of the sputtering coefficient occurs at smaller angles, etching pits form more rapidly, since a larger surface area is involved. At the same time, protrusions may be absent for large initial radii of curvature because the sections of the tip for which the angle of incidence of the beam corresponds to the sputtering maximum are too far apart and thus do not merge during subsequent treatment. This implies that the initial shape of the tip is ''too flat.''

To sum up, these results show that under certain conditions, ion sputtering can give rise to protrusions at the apex of probe microscope tips, having a considerably smaller radius of curvature than the initial surface. Under more prolonged ion beam treatment the protrusions may become cylindrical with a flattened end. This is consistent with the experimental results[4–6,12] and the theory.[11] Cylindrical tips are preferable when the microscope is used to probe a surface relief with vertical walls.

[1] M. A. Lantz, S. J. O'Shea, M. E. Welland, and K. L. Johnson, Phys. Rev. B **55**, 10776 (1997).

[2] Chen Yufeng, Xu Wei, and Huang Jinlin, J. Phys. E **22**, 455 (1989).

[3] J. P. Ibe, P. P. Bey Jr., S. L. Brandow, C. R. K. Brizzolara, and R. J. Colton, J. Vac. Sci. Technol. A **8**, 3570 (1990).

[4] M. V. H. Rao and B. K. Mathur, Indian J. Pure Appl. Phys. **31**, 574 (1993).

[5] M. J. Vasile, D. A. Crigg, J. E. Griffith, E. A. Fitzgerald, and P. E. Russel, Rev. Sci. Instrum. **62**, 2167 (1991).

[6] L. C. Hopkins *et al.*, J. Vac. Sci. Technol. B **13**, 335 (1995).

[7] S. Morishita and F. Okuyama, J. Vac. Sci. Technol. A **9**, 167 (1991).

[8] G. V. Dedkov and S. Sh. Rekhviashvili, Pis'ma Zh. Tekh. Fiz. **23**(11), 88 (1997) [Tech. Phys. Lett. **23**, 452 (1997)].

[9] H. H. Andersen and H. L. Bay, in *Sputtering by Particle Bombardment I*, edited by R. Berish (Springer-Verlag, Berlin, 1981), p. 200.

[10] G. Falcone, Riv. Nuovo Cimento **13**(1), 1 (1990).

[11] G. Carter, B. Navinsek, and H. L. Whitton, in *Sputtering by Particle Bombardment II*, edited by R. Berish, Springer Topics in Applied Physics Vol. 52 (Springer-Verlag, Berlin 1983), p. 231.

[12] H. Hasuyama, Y. Kanda, T. Soeda, K. Niiya, and M. Kimura, Mater. Sci. Eng. **90**, 33 (1987).

Translated by R. M. Durham

TECHNICAL PHYSICS LETTERS VOLUME 25, NUMBER 1 JANUARY 1999

Trajectory tracing — a new method of studying the evolution of states of dynamic systems

P. N. Gorley, P. P. Horley, and P. M. Tomchuk

Chernovtsy State University, Chernovtsy;
Institute of Physics, National Academy of Sciences of the Ukraine, Kiev

(Submitted March 19, 1998)
Pis'ma Zh. Tekh. Fiz. **25**, 17–24 (January 12, 1999)

A rapid method of trajectory tracing is proposedand described, which can clearly determine the points of period doubling bifurcations and provide clear information on the transformation of the states of a system in phase space. © *1999 American Institute of Physics.*
[S1063-7850(99)00301-8]

Self-organization processes in various nonequilibrium dynamic systems are currently being studied intensively both from the purely academic perspective of developing a new paradigm and because of the possibility of developing new principles for the functioning of complicated technological systems.[1,2] The evolution of dynamic systems as a function of their control parameters is usually studied using numerical characteristics which describe the phase portrait of the system as a whole (such as the Hausdorff dimension or the Lyapunov exponents[1,2]) or by determining the spectral characteristics of the components.[3] These methods have the disadvantage that they require a relatively large amount of computer time and the accuracy of the calculations depends strongly on the initial conditions and the choice of integration step.[1–4] Thus, there is an urgent need to develop simple rapid methods which do not have these disadvantages and can be used to study the evolution of complicated dynamic systems with the necessary accuracy.

Here we propose one such method, which we term trajectory tracing, which can clearly determine the points of period-doubling bifurcations and provide clear information on the transformation of the states of a system in phase space. This method also has the advantages of a simple algorithm and high speed. In addition, a method of constructing bifurcation diagrams developed earlier for iteration processes[4] is modified here for the case of continuous dynamic processes. In this case, the bifurcation diagram is a set of points corresponding to the extrema of one of the components of the phase space as a function of the control parameter. This modified method can be used to determine with a high degree of accuracy the values of the control parameters for which low-order period-doubling bifurcations occur, and can also qualitatively trace the scenarios for transition from order to chaos.

1. In order to describe the essential features of the tracing method, we shall consider a phase trajectory in N-dimensional space, which is obtained experimentally or numerically and consists of M points. The trajectory points usually ''loop'' for a certain time before reaching an attractor.[5,6] Thus, we position the origin at a point M_0 which definitely belongs to the attractor. To be specific, we shall assume that $M_0 = M/2$. We construct an initial N-dimensional vector from the point M_0 to the point M_0+1 and some other vector, for example, having the coordinates $(M_0+1;\ M_0+2)$. Let us assume that the spatial angle between these vectors is α. We also determine the angles α_R between the initial vector and an arbitrary Rth vector constructed between the points $(M_0+R,\ M_0+R+1)$, where $0 \leqslant R \leqslant M_0$. We construct the dependence of $\cos\alpha_R$ on the length of the tracing section of the phase trajectory R, which will be the tracing curve. The cosine of the angle for the N-dimensional case is then determined by a standard method using a scalar vector product.[7]

We bear in mind that a phase portrait is a discrete set of points whose distribution density along the phase trajectory is generally nonuniform. Obviously, if the phase portrait points were uniformly distributed, for example, over a circle, the tracing curve would be close to sinusoidal. If the phase portrait is an ellipse, the phase points are usually more densely distributed at the sites of maximum curvature. In this case, depending on the type of ellipse, the tracing curves will be very close to triangular (for a prolate ellipse) or rectangular (for an oblate ellipse). Naturally, doubling of the peaks on the tracing curves is observed in the presence of period-doubling bifurcations, with higher-order bifurcations generating smaller peaks.

2. We now report the results of comparative calculations for the most comprehensively studied attractors, those of Lorenz and Rössler, which are described by the following systems of equations:[4]

a) Lorenz attractor

$$\dot{x} = \delta(y-x), \quad \dot{y} = x(r-z)-y, \quad \dot{z} = xy-bz, \tag{1}$$

b) Rössler attractor

$$\dot{x} = -y-z, \quad \dot{y} = x+ay, \quad \dot{z} = b+z(x-\mu), \tag{2}$$

where a, b, r, μ, and δ are the control parameters.

Figures 1 and 2 give the maximum Lyapunov exponent as a function of the control parameter (a), the evolution of the tracing curves (b), and bifurcation diagrams of the y component of the system (c) for Rössler and Lorenz attractors, respectively. The general form of these attractors is

 © 1999 American Institute of Physics

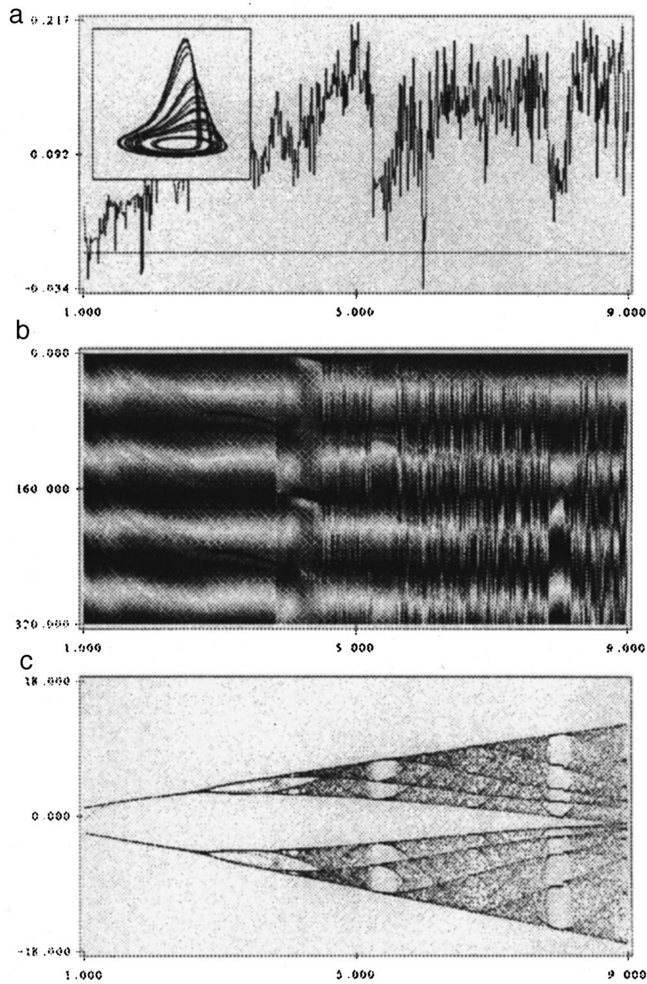

FIG. 1. Characteristics of a Rössler attractor as a function of the control parameter μ: a — maximum Lyapunov exponent, inset — general form of the attractor; b — evolution of the tracing curve. The dark sections correspond to $\cos\alpha_R=+1$ and the light sections correspond to $\cos\alpha_R=-1$. The length of the tracing section of the phase trajectory R is plotted on the ordinate; c — bifurcation diagram of component y.

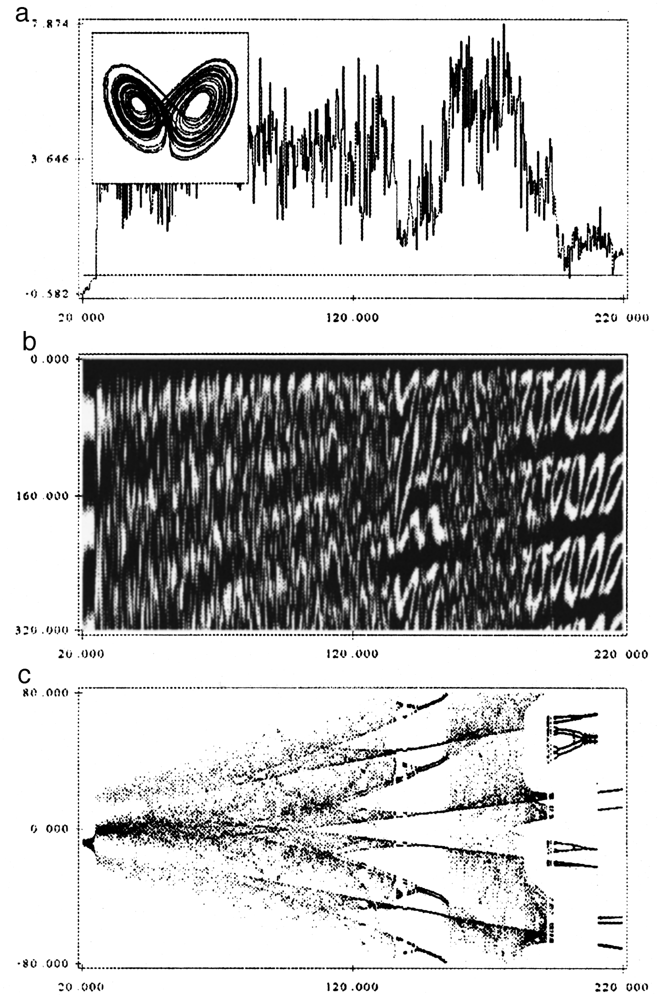

FIG. 2. Characteristics of a Lorenz attractor as a function of the control parameter r: a — maximum Lyapunov exponent, inset — general form of the attractor; b — evolution of the tracing curve. The dark sections correspond to $\cos\alpha_R=+1$ and the light sections correspond to $\cos\alpha_R=-1$. The length of the tracing section of the phase trajectory R is plotted on the ordinate; c — bifurcation diagram of component y.

shown in the insets. For the Lorenz attractor we selected r as the control parameter and for the Rössler attractor we selected μ.

As is well known,[4] the Rössler attractor is a fairly stable ordered system, as is evidenced by the low values of the maximum Lyapunov exponent (Fig. 1a). As the values of the control parameter increase, the Lyapunov exponent increases, indicating that the stability of the system deteriorates and a transition then takes place to a chaotic state. The bifurcation diagram (Fig. 1c) consists of two almost symmetric branches and at the initial stage the transition of the system from order to chaos takes place via period-doubling bifurcations of the oscillations, similar to the dynamics of Verhulst populations.[4]

Disadvantages of the Lyapunov exponents and the Hausdorff dimension, which are calculated for the phase portrait as a whole (i.e., taking into account all the phase variables), include their low information content since only the degree of stability of a system can be assessed from their sign or magnitude. Although the bifurcation diagram possesses greater clarity, it also has some shortcomings. For instance, it is usually calculated for iterative processes[4] or, as in our case, for a single phase variable and can only be used to determine the first few values (in practice three or at most four) of the control parameter for which period-doubling bifurcations of the oscillations take place.

The proposed tracing method yields results which have significant advantages over the Lyapunov exponents (like the Hausdorff dimension) and the bifurcation diagram. It can be seen from Fig. 1b that the mapping of the evolution of the tracing curve is clearer not only compared with the functional dependence of the maximum Lyapunov exponent but also compared with the bifurcation diagram. This mapping can also be used to determine fairly accurately more (or at least no fewer) values of the control parameter for which the oscillations undergo period-doubling bifurcations compared with the bifurcation diagram and most importantly, this mapping clearly shows that even in the chaotic state, the system contains information on its essential topological features. This last property is evidenced by the fact that in our particular case of a Rössler attractor, the topological form of the

attractor characteristic of the system exhibits random changes (shifting and stretching) in the chaotic region, which is shown in Fig. 1b by alternating dark and light bands with a specific period. In other words, the proposed tracing method can clearly demonstrate so-called deterministic chaos.[5]

All the above reasoning, with one exception, can also be applied to a Lorenz attractor (Fig. 2). Before specifying this exception, we note that this attractor is substantially more random than the Rössler attractor.[1,4] This can be seen clearly from the data plotted in Fig. 2: in the range of control parameters being studied, the values of the maximum Lyapunov exponent are more than an order of magnitude larger than those for the Rössler attractor and the bifurcation diagram predominantly incorporates chaotic states separated by a small region of stability. Thus, the scenario for the transition from order to chaos in a Lorenz attractor can most likely be classified as state intermittance.[2] It can also be seen that the intervals of ordered motion on the mapping of the tracing curves (Fig. 2c) and the bifurcation diagram (Fig. 2b) are the same.

The meaning of the exception for the Lorenz attractor is that in the randomized state for values of the control parameter in the range $20 \leqslant r \leqslant 165$, competition takes place between two equivalent attracting centers[1,4] and thus even a negligible change in the value of the control parameter can change the order in which the phase point goes round the trajectory. In Fig. 2b this corresponds to the fact that as the control parameter decreases, the stable structures which exist for $r > 180$ decay into two types of alternating dark and light bands of competing influence (width). Thus, the proposed tracing method can also clearly demonstrate the dynamics of the formation of stable structures from competing possibilities.

It should be noted that calculations made using our algorithms both for the tracing curves and for the bifurcation diagram are almost 1.5 times faster than the calculations of the Hausdorff dimension and at least twice as fast (depending on the number of evolution steps of the phase vector) as the calculations of the maximum Lyapunov exponents.

Thus, we have proposed an effective new method of studying the evolution of the states of nonequilibrium dynamic systems whose advantages over the Lyapunov exponents, the Hausdorff dimension, and bifurcation diagrams include informativeness, clarity, a simple algorithm, and fast calculations.

This work was partially supported by the Ukraine State Fund for Fundamental Research (Grant No. 2.4/745, 1977).

[1] H. Haken, *Advanced Synergetics: Instability Hierarchies of Self-Organizing Systems and Devices* (Springer-Verlag, New York, 1983; Mir, Moscow, 1985, 423 pp.).

[2] G. Nicolis and I. Prigogine, *Self-Organization in Non-Equilibrium Systems* (Wiley, New York, 1977; Mir, Moscow, 1979, 512 pp.).

[3] S. L. Marple, Jr., *Digital Spectral Analysis with Applications* (Prentice-Hall, Englewood Cliffs, N. J., 1987; Mir, Moscow, 1990, 584 pp.).

[4] A. J. Lichtenberg and M. A. Liberman, *Regular and Stochastic Motion* (Springer-Verlag, New York, 1982; Mir, Moscow, 1984, 528 pp.).

[5] H. G. Schuster, *Deterministic Chaos* (Physik-Verlag, Weinheim, 1984; Mir, Moscow, 1988, 240 pp.).

[6] P. N. Gorleĭ, P. P. Horleĭ, and P. M. Tomchuk, Pis'ma Zh. Tekh. Fiz. **22**(20), 82 (1996) [Tech. Phys. Lett. **22**, 857 (1996)].

[7] G. A. Korn and T. M. Korn, *Mathematical Handbook for Scientists and Engineers* (McGraw-Hill, New York, 1961; Nauka, Moscow, 1970, 720 pp.).

Translated by R. M. Durham

Phase work hardening in lithium niobate ferroactive binary solid solutions

E. A. Dul'kin, L. V. Grebenkina, I. V. Pozdnyakova, L. A. Reznichenko, and V. G. Gavrilyachenko

Rostov State University
(Submitted July 2, 1998)
Pis'ma Zh. Tekh. Fiz. **25**, 68–70 (January 26, 1999)

Acoustic emission, dilatometric, and dielectric methods have been used to study the characteristics of phase work hardening in lithium niobate ferroceramic samples. A correlation is established between the corresponding dependences for the third, fifth, and eighth thermal cycles in the phase transition region of the samples. It is hypothesized that the observed hardening characteristics are caused by annihilation of dislocations and their diffusion toward crystallite boundaries. © *1999 American Institute of Physics.* [S1063-7850(99)02801-3]

The phenomenon of phase work hardening was observed by Gavrilyachenko *et al.*[1] in ferroelectric $PbTiO_3$ crystals from acoustic emission data. It was established that the acoustic emission activity $\dot{N}$ reaches a maximum for the sixth phase transition cycle, and this was attributed to annihilation of aftergrowth and work hardening dislocations. As the number n of phase transition cycles increased further, $\dot{N}$ decreased exponentially as for phase work hardening in metals.[2] Quite clearly, phase work hardening should also be observed in a ferroelectric ceramic.

In a ferroceramic the phase transition is complicated by the interaction of a large number of crystallites which are intercoupled via the intercrystallite layer. This leads first, to the evolution of mechanical stresses produced by a spontaneous deformation jump and second, to the formation of a nonuniform depolarization field because the electroneutrality condition is not satisfied at the crystallite boundaries. These factors strongly influence the phase transition kinetics in ferroceramics.[3]

The aim of the present paper is to study the characteristics of phase work hardening in lithium niobate ferroceramic samples using acoustic emission, dilatometric, and dielectric methods.

The ceramic samples were synthesized by solid-phase reactions followed by hot pressing. Disk samples 10 mm in diameter and 1 mm thick were investigated using the complex method.[4] The acoustic emission activity $\dot{N}$ and the relative dilatation $\Delta L/L$ of the samples were measured simultaneously in the phase transition region. At the same time, the permittivity was measured by the bridge method at a frequency of 20 kHz and the broadening D of the phase transition was determined by a method described in Ref. 5.

We studied a wide range of samples of $(Na_{1-x}Pb_x)(Nb_{1-y}Ti_y)O_3$ and $(Na_{1-x}Li_x)NbO_3$ binary solid solutions in which phase work hardening was observed to varying degrees. We present the characteristics of phase work hardening in $(Na_{1-x}Li_x)NbO_3$ ferroceramic samples with $x=0.1175$ (see Fig. 1).

The broadening D of the phase transition decreases monotonically, with minima in the third, fifth, and eighth phase transition cycles. After the eighth cycle, the curve $D(n)$ gradually saturates.

The dilatation curve has the form of a typical hysteresis loop. During thermal cycling the amplitude of the loops and their slope remain constant, with only their width varying, i.e., the temperature hysteresis ΔT_g. The value of ΔT_g decreases monotonically, passing through minima for the third and eighth cycles and a maximum for the fifth cycle. After

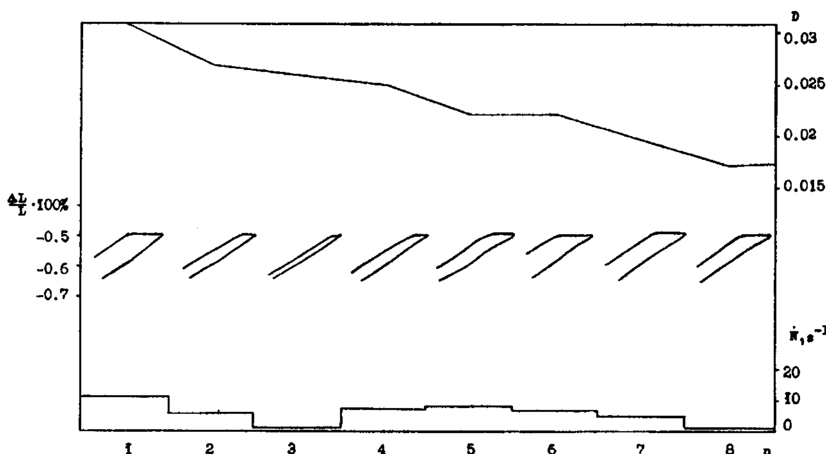

FIG. 1. The phase transition broadening D, temperature hysteresis ΔT_g, and acoustic emission activity $\dot{N}$ versus the number n of thermal cycles in the phase transition region of $(Na_{1-x}Li_x)NbO_3$ ferroceramic samples with $x=0.1175$.

 © 1999 American Institute of Physics

the eighth cycle the value of ΔT_g also saturates.

The acoustic emission activity $\dot{N}$ has the highest value for the first cycle. During thermal cycling the value of $\dot{N}$ decreases slightly, exhibiting minima for the third and eighth cycles and a maximum for the fifth cycle. After the eighth cycle, the value of $\dot{N}$ continues to decrease monotonically.

A comparison of the experimental behavior of $D(n)$, $\Delta T_g(n)$, and $\dot{N}(n)$ reveals that these are correlated.

The acoustic emission maximum $\dot{N}$ for the fifth phase-transition cycle corresponds to the most intensive annihilation of dislocations, as in Ref. 1. Interestingly, some increase in ΔT_g is observed. Conversely, the decrease in ΔT_g for the third and eighth cycles indicates that the ceramic crystallites have fewer defects. The low level of $\dot{N}$ for these phase transition cycles suggests that at the same time as the dislocations are being annihilated, they diffuse toward crystallite boundaries, promoting relaxation of the mechanical stresses at the crystallite–matrix boundary. For the first cycles this process has a wave-like nature and then attenuates with increasing n as a result of the hardening of the material.

[1] V. G. Gavrilyachenko, E. A. Dul'kin, and A. F. Semenchev, Fiz. Tverd. Tela (St. Petersburg) **37**, 1229 (1995) [Phys. Solid State **37**, 668 (1995)].
[2] V. A. Plotnikov, L. A. Monasevich, and Yu. M. Paskal', Fiz. Met. Metalloved. **65**, 1219 (1988).
[3] V. G. Gavrilyachenko, V. D. Komarov, and E. G. Fesenko, *Fundamental Problems of Ferroelectronics*, Vol. 1 [in Russian], Rostov State University Press, Rostov (1995), pp. 150–157.
[4] E. A. Dul'kin, Sverkhprovodimost' (KIAE) **5**, 103 (1992).
[5] J. Dudek, M. F. Kupriyanov, and G. N. Konstantinov, Ferroelectrics **81**, 249 (1988).

Translated by R. M. Durham

Effect of electric fields on the amorphous state⇒crystal transition in BiPbSrCaCuO (2223) films

V. N. Varyukhin, V. D. Okunev, and Z. A. Samoĭlenko

Donetsk Physicotechnical Institute, National Academy of Sciences of Ukraine

(Submitted August 21, 1998)
Pis'ma Zh. Tekh. Fiz. **25**, 71–77 (January 26, 1999)

Results of studying the influence of electric fields on the structure and electrical properties of BiPbSrCaCuO (2223) films undergoing the transition from the amorphous to a crystalline state are discussed. It is shown that passing a current through the samples during high-temperature annealing substantially increases the growth anisotropy, improves the quality of the texture, and increases the electrical conductivity of the films by between one and five orders of magnitude compared with control samples. It is concluded that the mechanism is attributable to carrier transport in (001) type planes, which facilitates changes in the atomic order. Unlike in the control samples, this family of planes plays a leading role in structural transformations. © *1999 American Institute of Physics.* [S1063-7850(99)02901-8]

Recently, the problem of controlling the structure of solids by acting on their electronic subsystem has attracted increased interest among researchers.[1] However, examples of applying these results to technology are few and far between.

We know that if various conditions are satisfied, the amorphous-state–crystal transition can be used to obtained textured high-temperature superconducting (HTSC) films with high critical parameters.[2–5] This technology is preferable for complex systems such as BiPbSrCaCuO (2223) for which *in situ* preparation presents difficulties. The conditions to be satisfied include constraints on the thickness of the amorphous layer and stringent constraints on its structure and annealing conditions. For instance, the thickness of the amorphous film should be less than 1 μm. Only then can the influence of the crystal field of the substrate and the elastic stresses at the interface have the maximum effect on the formation of the cluster structure and the subsequent crystallization of the films.[6] As their thickness increases, the influence of the interface becomes weaker, the formation of the cluster structure becomes similar to the spontaneous self-organization of a noncrystalline substance, and the amorphous-state–crystal transition results in the formation of a normal polycrystalline structure.

The cluster structure of the amorphous films should contain elements characteristic of the 2223 phase and be well-suited to texture growth under high-temperature annealing: the main type of clusters should comprise fragments of (001) planes, which can be achieved in a narrow range of growth temperatures for amorphous films.[7,8]

Finally, of course, the annealing procedure itself plays an important role: to produce the 2223 phase the fastest possible heating is required to temperatures of ~865–870 °C, close to the melting point, followed by holding at this temperature for several hours.

Electric fields are an easily applied external influence capable of exaggerating the anisotropy of the crystal growth from the amorphous phase, reducing the azimuthal misorientation of the blocks, and enhancing the quality of the texture. The multicomponent nature of high-temperature superconductors and the many types of structural transformations accompanying amorphous-state–crystal transitions are conducive to the influence of external effects on the crystallization of amorphous films. For a Bi system the dominant factor in this process is the competition between the 2212 and 2223 phases[5] and the families of $(11l)$ and $(00l)$ planes.[9]

Here we study the influence of electric fields $F \leqslant 2 \times 10^3$ V/cm on an amorphous-state–crystal transition in $Bi_{1.8}Pb_{0.2}Sr_2Ca_2Cu_3O_{10+x}$ films in the temperature range 840–870 °C using platinum electrodes clamped to the film (Fig. 1). The thickness of the films grown on MgO substrates was 0.2–1.0 μm and their resistivity in the amorphous state was $(10^6–10^8)\,\Omega\cdot$cm. We varied the heat treatment times in the electric field between ~20 s and several tens of minutes. Control samples were annealed under the same conditions but without an electric field. The experiments were carried out under current-limited conditions so that the maximum currents through the sample did not exceed the levels normally used for measuring currents ($<1\ \mu$A) and could not alter the temperature of the samples. The initial amorphous layers were grown in a diode system by sputtering stoichiometric targets under moderate plasma activation regimes.[10]

The experiments showed that the structure and properties of the crystallizing films depend strongly on the presence of an electric field. In the presence of a field, the resistivity of the films after crystallization is always lower than that of the control samples; this difference, which decreases with increasing temperature and annealing time, always remains and can be as much as five orders of magnitude if the initial conditions of crystal structure formation were unfavorable.

Specific features of the film behavior depend on the composition, initial structure, thickness, type of substrate, and experimental conditions. Despite this, some general features exist:

Electric fields always intensify growth anisotropy, in fa-

 © 1999 American Institute of Physics

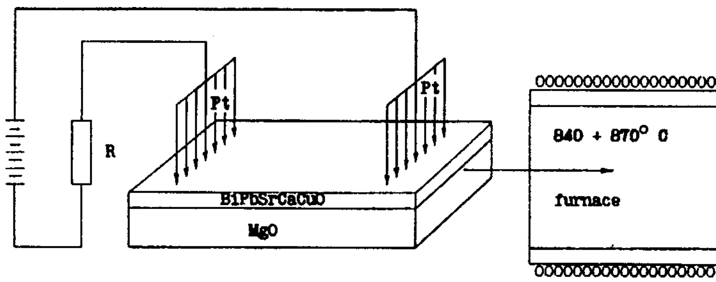

FIG. 1. Schematic of experiment.

vor of the preferential development of (00l) planes which are responsible for the conductivity and superconductivity of high-temperature superconductors;

In 2223 films electric fields stimulate the evolution of the 2223 phase and suppress the formation of structural elements of the 2212 phase;

The electric field reduces the resistivity of the crystallized layers by 1–5 orders of magnitude.

By way of example Fig. 2 gives comparative data for treated and control samples under unfavorable conditions (low annealing temperature) of an amorphous-state–crystal transition. It can be seen that the electric field intensifies the growth anisotropy and stimulates preferential development of the family of 2223-phase (00l) planes — (008), (00$\underline{10}$), (00$\underline{12}$), (00$\underline{14}$), (00$\underline{16}$). For the control sample, however, the dominant reflections are assigned to (11l) planes of both phases: in addition to the 2223-phase (111) line, the (115) and (117) lines of the 2212 phase are also observed. Since the annealing temperature (840 °C) is low for the formation of the 2223 phase, the intensities of the (00$\underline{10}$), (00$\underline{14}$), and (00$\underline{16}$) lines comprising the family of (00l) planes are negligible in the control sample.

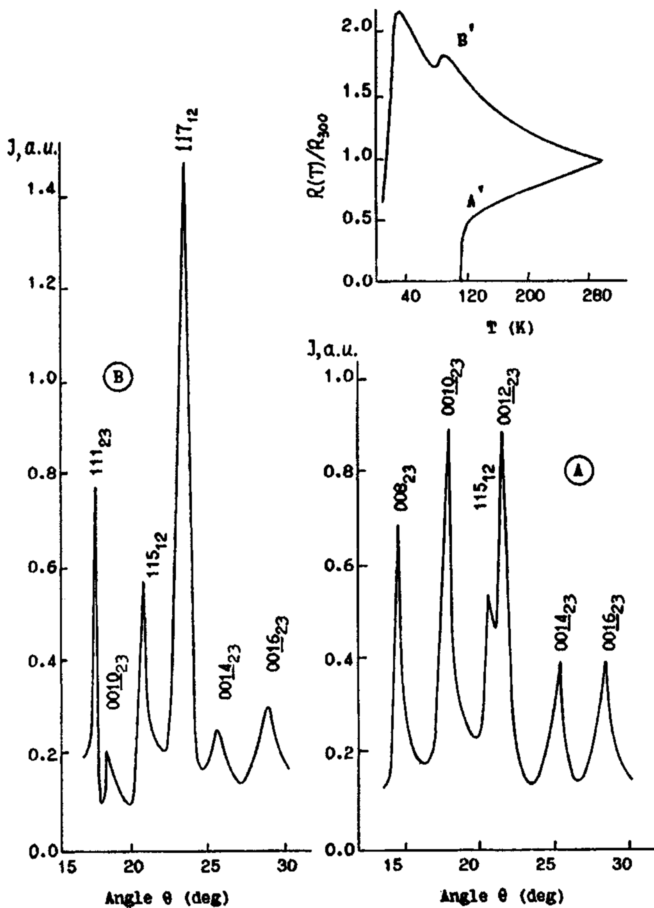

FIG. 2. Influence of an electric field ($F=1\times10^3$ V/cm at $T=300$ K) on the structure and temperature dependence of the resistance. A — diffraction pattern of the film after annealing in an electric field; the subscripts indicate whether the lines belong to the 2212 or 2223 phases. The inset gives the temperature dependence of the resistance (A'). B and B′ — as A and A′ but for the control sample (annealing without an electric field). Film thickness $d=0.7\,\mu$m, annealing temperature $T_a=840\,°$C, annealing time $t_a=3$ min. The samples were annealed in air at atmospheric pressure.

The electric fields used here ($F\leqslant2\times10^3$ V/cm) are too weak to directly influence the structure of the films. The fields may have an indirect influence, inasmuch as they may reduce the potential barriers impeding changes in the configuration of atomic bonds. However, even with rapidly increasing temperature, this influence is restricted to temperatures of 350–450 °C, when heated to which the resistance of the samples decreases by 4–5 orders of magnitude.

As a result of the need to limit the currents through the sample, even at the beginning of crystallization (450 °C), the electric fields did not exceed 100 V/cm. Here the nonuniform distribution of fields in the samples may play an important role in converting clusters into crystallites. The concentration of fields in the peripheral regions of the clusters, as a result of the enhanced resistance of these structural elements, locally increases the electric field strength and creates conditions for intensified growth anisotropy at the beginning of the formation of the crystal phase. The initial anisotropy in the cluster structure of amorphous films is an important factor for texture growth.[6]

Nevertheless, despite the weak fields an electric current flows through the sample in all cases, even under annealing in the working temperature range (840–870 °C). We attribute the characteristic structural changes considered here to this charge transport. The influence of the mobile electron subsystem on the atomic order and properties of films was observed by us earlier and has been used in technology.[4,5,7,8] For example, depending on the growth temperature T_s of the amorphous films, the values of T_c may vary between ~60 and 110 K for the same high-temperature annealing regimes.

As a result of electron diffusion, aging without an applied external electric field for several months (annealing the samples at room temperature) leveled out the difference in the resistivities of the freshly prepared samples; for some samples the coefficient of optical absorption α in the photon energy range $\hbar\omega=0.5-2.5$ eV increased between two and five times. As a result, when the films crystallized after aging

all the samples were single-phase (2223 phase) and the temperature dependences of their resistance were almost indistinguishable.[5] A zero-resistance state is established in these samples at temperatures between 102 and 105 K.

These results are a good illustration of the fundamental mechanism of self-organization in noncrystalline materials:[11] they tend to undergo a transition to a structural state which is determined by the lowest energy of the forming phase. Aging takes place at ~ 300 K, when ion diffusion over appreciable distances is highly unlikely. The dominant role in the formation of the long-range order in the ion configuration is played by the displacement of carriers and redistribution of the electron density between ions of different species, followed by changes in the configuration of the interatomic bonds, preferentially within the short-range order. Changes in the charge state and therefore the valence of copper or bismuth ions are the most probable.[12–14]

Experiments to study the influence of current training ($T \simeq 300$ K) on the structure and properties of amorphous Bi(Pb)SrCaCuO films confirmed the action of the electron diffusion mechanism. It was established that even under weak electrical influences, the electronic and atomic subsystems undergo rearrangement. When the currents through the samples are $\sim 10^{-10}$–10^{-8} A the aging processes are accelerated by two or three orders of magnitude. The currents can also influence the electronic structure of HTSC crystalline films.[15]

At high temperatures the carrier flux increases the possibility of changes in the film structure still further. The spatially anisotropic motion of the electrons, mainly in $(00l)$ planes, facilitates the subsequent predominant evolution of this atomic order in the incipient multicomponent crystal structure, with the participation of clusters which have fragments of these planes oriented along the lines of flow and thus parallel to the surface of the film. The current flow does not influence the fragments of $(11l)$ planes with dielectric properties which do not participate in the charge transport. The $(11l)$ family characterizes the structure and properties of the control film (Fig. 2B) when the experimental parameters are unfavorable for the evolution of the family of $(00l)$ planes.

To conclude, the carrier flux under the action of an electric field in amorphous Bi(Pb)SrCaCuO samples activates the peripheral regions of the $(00l)$ clusters, systematically preparing first the electronic subsystem and then the ionic subsystem for an increase in the sizes of the ordered regions. This is stimulated by elementary second-order phase transitions of the disorder⇒order type, mainly at the broadened interfaces of $(00l)$ clusters. This selectivity of the electric current flow to the type of structural elements is responsible for the increased crystallographic anisotropy and the formation of a texture with the c axis perpendicular to the surface of the films, which ensures that the films have high critical parameters.

[1] V. S. Vavilov, Usp. Fiz. Nauk **167**, 407 (1997).
[2] Atsushi Tanaka, Takato Machi, Nobuo Kamehara, and Koichi Niwa, Appl. Phys. Lett. **54**, 1362 (1989).
[3] Yu. Mei, H. L. Luo, and R. Hu, Appl. Phys. Lett. **56**, 581 (1990).
[4] V. D. Okunev, N. N. Pafomov, B. I. Perekrestov, and V. M. Svistunov, Pis'ma Zh. Tekh. Fiz. **20**(10), 60 (1994) [Tech. Phys. Lett. **20**, 414 (1994)].
[5] V. D. Okunev, N. N. Pafomov, I. Iguchi, and V. M. Svistunov, Zh. Tekh. Fiz. **65**(12), 106 (1995) [Tech. Phys. **40**, 1260 (1995)].
[6] V. D. Okunev, Z. A. Samoĭlenko, E. I. Pushenko, Yu. F. Revenko, and B. I. Perekrestov, Neorg. Mater. **30**, 226 (1994).
[7] V. D. Okunev, Z. A. Samoĭlenko, N. N. Pafomov, and T. A. D'yachenko, Neorg. Mater. **32**, 855 (1996).
[8] Z. A. Samoĭlenko, V. D. Okunev, E. I. Pushenko, N. N. Pafomov, and O. P. Cherenkov, Neorg. Mater. **32**, 359 (1996).
[9] V. D. Okunev and Z. A. Samoĭlenko, Pis'ma Zh. Tekh. Fiz. **24**(1), 13 (1998) [Tech. Phys. Lett. **24**, 6 (1998)].
[10] V. D. Okunev, N. N. Pafomov, Z. A. Samoĭlenko, and V. M. Svistunov, Pis'ma Zh. Tekh. Fiz. **19**(5), 39 (1993) [Tech. Phys. Lett. **19**, 147 (1993)].
[11] V. D. Okunev and Z. A. Samoĭlenko, JETP Lett. **53**, 44 (1991).
[12] H. Ishizuka, Y. Idemoto, and K. Fueki, Physica C **195**, 145 (1992).
[13] Y. Idemoto, H. Tokunaga, and K. Fueki, Physica C **231**, 37 (1994).
[14] T. V. Sukhareva and V. V. Eremenko, Fiz. Tverd. Tela (St. Petersburg) **39**, 1739 (1997) [Phys. Solid State **39**, 1548 (1997)].
[15] V. N. Samovarov, Fiz. Tverd. Tela (St. Petersburg) **39**, 1747 (1997) [Phys. Solid State **39**, 1556 (1997)].

Translated by R. M. Durham

Control of the spectral characteristics of organic dye molecules adsorbed in porous glass by preliminary chemical modification of the pore surface

V. N. Beger, A. Yu. Fadeev, and G. V. Lisichkin

St. Petersburg State Institute of Precision Mechanics and Optics (Technical University); M. V. Lomonosov State University, Moscow
(Submitted August 22, 1997)
Pis'ma Zh. Tekh. Fiz. **25**, 78–82 (January 26, 1999)

The electron spectra of organic dye molecules adsorbed in silicate porous glass were modified by preliminary chemical hydrophobization of the pore surface. A comparative study was made of the absorption spectra of various laser dyes introduced in modified and initial unmodified porous glasses. © *1999 American Institute of Physics.* [S1063-7850(99)03001-3]

Optical materials formed by organic polyatomic molecules adsorbed in pores of silicate glasses are attracting considerable interest because of the possibility of efficiently using these materials in quantum electronics and applied optics, mainly as active media of solid-state tunable lasers.[1–3] Numerous studies have been made of the electron spectra and Raman spectra of dye molecules adsorbed in porous silicate glasses (see, for example, Refs. 4–7). So far, however, the range of these materials has been extended by varying the dyes used without making any appreciable changes to the nature of the carrier surface. We note that the polymer-impregnated, dye-activated porous glasses used as active elements of tunable lasers[2,8] are constructed using porous matrices with unmodified pore surfaces and have spectral characteristics very similar to those of dyes in porous glass which have not been impregnated with polymer.

At the same time, it is well known that molecules of many laser dyes exhibit substantial solvatochromism and solvatofluorochromism,[9] i.e., the electron absorption and fluorescence spectra of these molecules depend strongly on the interaction between each dye molecule and its nearest-neighbor molecules (for example, the solvate molecules in solutions). Quite clearly, in cases of adsorption, atomic and molecular groups of the adsorbent surface groups play the role of nearest neighbors for the adsorbed molecules. For porous silicate glasses these nearest neighbors are mainly silanol groups, which determine the main adsorption, chemical, and other properties of the pore surface of these materials and also determine the determine the electron spectra of dyes adsorbed in unmodified porous glasses.

Since chemical modification of the surface of siliceous materials[10–12] can alter the nature of the adsorbent surface fairly extensively and thus can change the local neighborhood of the adsorbed molecules, this type of modification of porous glasses may well prove extremely promising for controlling the spectral and other properties of adsorbed dyes. Note that this method of modifying the electron spectra of the adsorbates offers a completely new way of extending the range of solid-state microheterogeneous optical materials based on a combination of inorganic and organic components. Most importantly, this method may be applied not only to ''traditional'' laser dyes but also to molecules which, for various reasons, could not be used efficiently under adsorption conditions at an unmodified silica surface. Finally, no less important is the fact that covalent grafting of a modifier monolayer to the surface of a porous carrier generally does not affect its topology and porous structure.

Here the preparation of chemically modified porous matrices for subsequent saturation with organic dye molecules was carried out in two stages. First, we prepared unmodified porous glasses using well-known methods (as described by Zemskiĭ *et al.*[13]). The surface of the pores was then hydrophobized by treating the porous matrices with octyldimethylchlorosilane in toluene. The degree of modification of the surface was determined from the results of an atomic analysis for carbon. The grafting density was around 2 groups/nm^2. The maximum experimentally observed grafting density for a monolayer of alkyldimethylsilanes on silica is between 2.4 and 2.8 groups/nm^2 depending on the length of the alkyl chain.[14] Thus, the degree of hydrophobization of the pore surface can be fairly high. Various dyes were then introduced into the modified matrices from solutions and the solvent was removed from the pores by evaporation.

These experiments yielded the following results. First, it was found that for the hydrophobized porous glass and for the initial unmodified glass the dye adsorption is reversible, which indicates that physical adsorption mechanisms predominate. It was also observed that the spectral characteristics of the adsorbed dyes in the hydrophobized porous glass are fairly stable and in particular, do not vary when dye is repeatedly introduced and removed from the matrix pores (''washing'' with pure solvent). This also indicates that this modifying layer is stable in the presence of the various solvents used (such as heptane and toluene).

Second, and most importantly, we observed that the electron spectra of the dyes in the hydrophobized matrices differ appreciably from those of the same dyes in unmodified porous glass (see Fig. 1). For the modified matrices the spectra are shifted and their width changes. Moreover, the influence of the different nature of the adsorbent surface on the spectral characteristics of the adsorbed molecules is observed to differing degrees for different molecules. For instance, for

 © 1999 American Institute of Physics

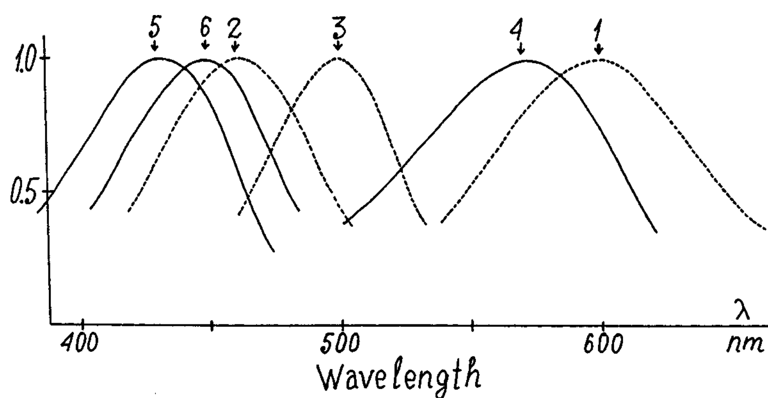

FIG. 1. Absorption spectra of dyes adsorbed in unmodified (*1*, *2*, *3*) and hydrophobized (*4*, *5*, *6*) porous glass. The dyes were introduced into the porous matrices from heptane solutions. Dyes: *1*, *4* — oxazine 17, *2*, *5* — coumarin 30, and *3*, *6* — coumarin 7.

oxazine 17 the maximum of the absorption band in hydrophobized porous glass is only shifted by $850\,cm^{-1}$ whereas for coumarin 30 the shift is $1650\,cm^{-1}$ and for coumarin 7 the shift is $2220\,cm^{-1}$. The shift of the absorption spectra is accompanied by a specific increase in their width (around 15% on average). The nature of the increase in the width of the electron spectra of the adsorbates may be attributed to an increase in the inhomogeneous component of the spectra (as a result of the presence of molecules adsorbed on the modified surface and on sections which have remained unmodified). It is also possible that the change in the width of the adsorbate spectra may be caused by a change in the homogeneous component of the spectra. Further investigations are required to determine for sure which particular mechanism predominates.

In order to study the possibility of dimers and other higher molecular association compounds being formed, we made a comparative study of the absorption spectra of dye molecules adsorbed in hydrophobized matrices when the concentration of adsorbate molecules was varied. However, no significant changes in the position and shape of the absorption spectra of these adsorbates were detected up to concentrations of order $10^{18}\,cm^{-3}$ (higher concentrations were not studied). Note that earlier studies of this type for unmodified porous glass[15] yielded a similar result. Thus, hydrophobization of the pore surface at least does not increase the probability of dimers and association compounds of dye molecules being formed under adsorption.

[1] G. N. Dul'nev, V. I. Zemskiĭ, V. V. Krynetskiĭ, I. K. Meshkovskiĭ, A. M. Prokhorov, and O. M. Stel'makh, Pis'ma Zh. Tekh. Fiz. **4**(9), 1041 (1978) [Sov. Tech. Phys. Lett. **4**, 420 (1978)].
[2] V. I. Zemskiĭ, Yu. L. Kolesnikov, and I. K. Meshkovskiĭ, Pis'ma Zh. Tekh. Fiz. **12**(3), 331 (1986) [Sov. Tech. Phys. Lett. **12**, 136 (1986)].
[3] V. S. Smirnov, V. I. Zemskiĭ, and A. I. Yartsev, Opt. Spektrosk. **68**, 960 (1990) [Opt. Spectrosc. **68**, 562 (1990)].
[4] V. I. Zemskiĭ, I. K. Meshkovskiĭ, and A. V. Sechkarev, Dokl. Akad. Nauk SSSR **267**, 1357 (1982) [Sov. Phys. Dokl. **27**, 1047 (1982)].
[5] V. I. Zemskiĭ, Yu. L. Kolesnikov, and I. K. Meshkovskiĭ, Opt. Spektrosk. **60**, 932 (1986) [Opt. Spectrosc. **60**, 574 (1986)].
[6] V. N. Beger and V. I. Zemskiĭ, Opt. Spektrosk. **74**, 552 (1993) [Opt. Spectrosc. **74**, 328 (1993)].
[7] A. V. Sechkarev and V. N. Beger, Izv. Ross. Akad. Nauk. Ser. Khim. No. 7, 1284 (1995).
[8] S. M. Dolotov, M. F. Koldunov, A. A. Manenkov, G. P. Roskova, N. M. Sitnikov, N. E. Khaplanova, and T. S. Tsekhomskaya, Kvantovaya Élektron. (Moscow) **19**, 1134 (1992) [Sov. J. Quantum Electron. **22**, 1060 (1992)].
[9] N. G. Bakhshiev (Ed.), *Solvatochromism: Problems and Methods* [in Russian], Leningrad (1989).
[10] I. V. Grebenshchikov, and T. A. Favorskaya, Tr. Gos. Opt. Inst. **7**, 1 (1931).
[11] *Modified Silicas in Sorption, Catalysis, and Chromatography*, edited by G. V. Lisichkin [in Russian], Khimiya, Moscow (1986), 248 pp.
[12] *Adsorption on New and Modified Inorganic Sorbents*, edited by A. Dabrowsk and V. A. Tertykh, Studies in Surface Science and Catalysis, Vol. 99 (Elsevier, 1995).
[13] O. S. Molchanova, *Sodium Borosilicate and Porous Glasses* [in Russian], Oborongiz, Moscow (1961), 162 pp.
[14] Yu. A. Fadeev and V. A. Eroshenko, Ross. Khim. Zh. **39**(6), 93 (1995).
[15] V. I. Zemskiĭ, I. K. Meshkovskiĭ, and I. A. Sokolov, Opt. Spektrosk. **59**, 328 (1985) [Opt. Spectrosc. **59**, 197 (1985)].

Translated by R. M. Durham

Use of porous dielectric films for electron-optical image conversion

Kh. N. Vezirov

Institute of Photoelectronics, Academy of Sciences of Azerbaijan, Baku
(Submitted May 21, 1998)
Pis'ma Zh. Tekh. Fiz. **25**, 83–87 (January 26, 1999)

It was established experimentally that, unlike the photoelectronic principle, the image conversion principle developed here can convert an image in a broader spectral range with a suitable choice of semiconductor material. For example, a device was fabricated with a sensitivity of 5 and 2 mA/W at the 2 and 2.5 μm wavelength, respectively. © *1999 American Institute of Physics.* [S1063-7850(99)03101-8]

It is known that electron-optical image converters operate on the principle of photoelectronic emission, i.e., emission of electrons by a photocathode under the action of incident radiation.[1] The long-wavelength photoelectronic emission threshold, which determines the spectral sensitivity of the image converter, depends mainly on the work function of the photocathode. Since a silver–oxygen–cesium photocathode has the lowest work function of all known films, approximately 0.5–0.8 eV (Ref. 2), image converters with this photocathode exhibit at least some sensitivity to the 1.5 μm wavelength range. However, no images converters capable of operating beyond 1.8 μm are available, which is a major disadvantage. Thus, extending the spectral sensitivity range of image converters into the middle infrared is a very relevant scientific and technical problem.

The present author succeeded in extending the sensitivity range of the image converter by using a different operating principle. Figure 1a shows the operating principle of this type of image converter. The molybdenum glass image converter consists of a casing *1*, 9 cm in diameter and 10 cm long, with entrance and exit windows *2* and *3*. A luminescence screen comprising a layer of phosphor *4* and a layer of aluminum *5* was fabricated at the exit mirror using conventional technology for image converter production. Unlike conventional image converters, this device also contains a cooling system *6* shown separately in cross section in Fig. 1b. The cooling system consists of a curved glass tube *6* filled with a coolant (such as dry ice) as required during operation of the image converter. The surface of a transparent plate *7* affixed to the tube *6* was coated with a semitransparent molybdenum film *8* around 10 nm thick by thermal deposition in vacuum. The edges of this film *8* were made thicker in the form of a ring *9* (this ring *9* is the baffle of a normal image converter[1–3]). In practice, the ring *9* and the film *8* are a single entity, since the film *8* was fabricated first and then the ring *9* was added. The baffle *9* and the luminescence screen have contact outputs *10* and *11* (0.2–0.3 mm diameter molybdenum wire) vacuum-tight welded into the glass. After suitable heat treatment (outgassing at 300–450 °C under vacuum), a semiconducting film *12* was grown onto the film *8*, for example, polycrystalline lead sulfide 2.5 cm in diameter and 200–500 nm thick.

After the film *12* was sensitized, a friable (very porous) dielectric film *13* of aluminum oxide around 150–250 nm thick was deposited on its surface. The dielectric film was produced by thermal deposition of aluminum in air at a pressure of 0.4–0.6 Torr. After the dielectric film had been outgassed in vacuum at 120–180 °C, a silver–oxygen–cesium photocathode *14* only around 10 nm thick was fabricated on its surface using a special technology. This photocathode had an island-like structure and functioned as a film with a minimal work function. The photocathode *14* was fabricated by heating an oxidized layer of silver in cesium vapor. The cesium atoms also penetrate into the pores of the dielectric film *13* and reach the surface of the semiconducting film *12*. This can lead to the formation of donor surface states at the surface of the semiconducting film and matching of the Fermi level in the bulk of the semiconductor to the top of the valence band. In this case, the photoemission threshold or the photoelectronic work function corresponds to the work function determined by thermionic emission.

In order to increase the emission of photoelectrons transferred to the semiconductor conduction band, the electron affinity energy of the material must obviously be reduced, which is equivalent to reducing the thermionic work function. This reduction in the thermionic work function is automatically achieved by cesium atoms reaching the surface of the semiconductor. The cesium atoms form a dipole layer on the vacuum-facing semiconductor surface, with the positive pole directed toward the vacuum. The electric field concentrated inside this layer facilitates the emission of electrons from the semiconductor into vacuum (into the pores of the dielectric). The reduction in the work function is proportional to the surface density of adsorbed cesium atoms and their dipole moment.

A very important factor for understanding the mechanism responsible for these processes is that the real value of the electron affinity does not depend on the bulk semiconductor doping and is determined by the material and state of its surface. In addition to cesium atoms the surface of the semiconductor may also have cesium oxide molecules, which have a higher dipole moment than cesium, so it is quite likely that states close to negative or zero electron affinity will form on the surface of the semiconductor.

When a working voltage (2–15 kV) is applied between the outputs *10* and *11*, thermal electrons which are always

 © 1999 American Institute of Physics

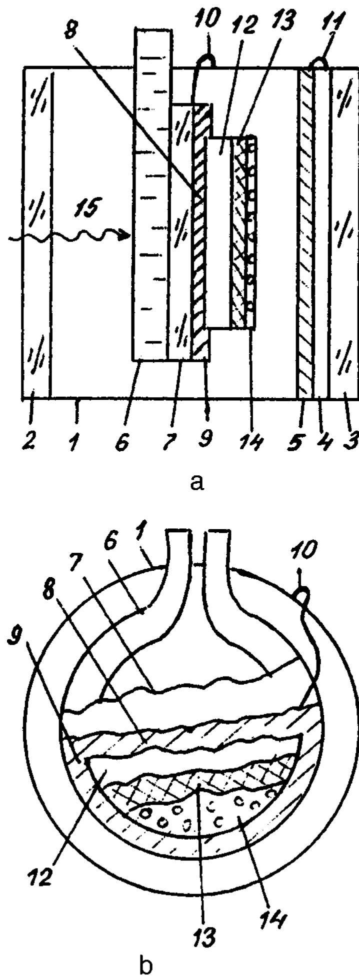

FIG. 1. Schematic of image converter (a) and cooling system (b).

present at room temperature as an electron cloud above the photocathode *14* are drawn off to the luminescence screen and as a result, the surface of the dielectric film *13* becomes positively charged and an electric field is created in the bulk. When the radiation being converted *15* enters the semiconducting film *12*, electrons form in its conduction band. Half of these drift toward the vacuum-facing surface and are emitted into the pores of the dielectric film *13* because of the extremely low work function (electron affinity). On entering the dielectric film *13*, the electrons emitted by the semiconducting film are accelerated and undergo avalanche multiplication in the pores as a result of secondary electron emission. This causes an even greater increase in the charge of the dielectric film, lowers the electron affinity, and results in the establishment of self-sustaining electron emission.[4] As they pass through the film *13*, the electrons enter the vacuum where they are accelerated by the anode voltage, bombard the screen, and cause it to luminesce.

Infrared radiation *15* from an object passes through the window *2* and the plate *7* and creates a specific irradiance distribution on the surface of the film *12*. This leads to an increase in the bulk concentration of free carriers, where the spatial distribution of the free electron concentration corresponds to the spatial distribution of the irradiance on the surface of the film *12* and thus corresponds to the spatial distribution of the brightness on the surface of the screen.

A change in the illuminance (irradiance) of sections of the film *12* changes the free electron concentration in these sections and alters the self-sustaining emission current from these sections, which produces a change in the brightness of the corresponding sections of the luminescence screen.

Electrons leaving points in the film *12* as a result of the radiation *15* are replenished mainly from the film *8*.

The sensitivity of this image converter at 1.06, 2.0, and 2.5 μm was 4.0, 5.0, and 2.0 mA/W, respectively, the spectral sensitivity characteristic was practically the same as that of zinc sulfide, and the spatial resolution was $\sim$12 r lm/mm.

To sum up, it has been established experimentally that unlike the photoelectronic principle, the proposed self-sustaining emission principle for image conversion can convert an image in a broader spectral range with a suitable choice of semiconductor material, which substantially extends the range of application of the image converter.

[1] M. M. Butslov, B. M. Stepanov, and S. D. Fanchenko, *Image Converters and Their Application in Scientific Research* [in Russian], Nauka, Moscow (1978),432 pp.

[2] V. S. Fomenko, *Handbook of Emission Properties of Materials* [in Russian], Naukova Dumka, Kiev (1981), 340 pp. [previous edition published as *Handbook of Thermionic Properties, Electronic Work Functions, and Richardson Constants of Elements and Compounds* Consultants Bureau, New York (1966)].

[3] V. Gartman and F. Berngard, *Photomultipliers* [in Russian], Gosénergoizdat, Moscow (1961), 208 pp.

[4] N. A. Soboleva and A. E. Melamid, *Photoelectronic Devices* [in Russian], Vysshaya Shkola, Moscow (1974), 327 pp.

Translated by R. M. Durham

Magnetic crystallographic anisotropy of Fe/GaAs(100) epitaxial films

S. L. Vysotskiĭ, S. S. Gel'bukh, A. S. Dzhumaliev. G. T. Kazakov, Yu. A. Filimonov, and A. Yu. Tsyplin

Saratov Branch of the Institute of Radio Engineering and Electronics, Russian Academy of Sciences
(Submitted July 31, 1998)
Pis'ma Zh. Tekh. Fiz. **25**, 88–95 (January 26, 1999)

An investigation was made of the anisotropic properties of Fe films obtained by molecular-beam epitaxy on GaAs(100) substrates. It is shown that at thicknesses t=40–50 Å the Fe films begin to exhibit cubic magnetic anisotropy. At thicknesses $t>100$ Å the first constant of cubic anisotropy K_1 has values similar to those for "bulk" Fe single crystals. Films of intermediate thickness $50<t<100$ Å possess both isotropic and anisotropic phases. © *1999 American Institute of Physics.* [S1063-7850(99)03201-2]

For many years the magnetic properties of thin films and multilayer structures have attracted close attention,[1–7] with the aim of improving the properties of media for magnetic recording of information, as well as being of fundamental interest. The most promising technology for fabricating these structures is molecular beam epitaxy, which can comparatively easily produce structures consisting of different layers of widely varying thickness, from a single monolayer up. Studies of such thin films can reveal their formation and in particular their anisotropic properties as a function of their thickness, crystallographic orientation, and the surface state of the substrate, and other factors. It has been observed that as the layer thickness varies, the direction of the axis of easy magnetization may change as a result of a change in the ratio of the contributions of the surface and bulk anisotropy. For example, for a single-crystal Fe(110) film grown on a GaAs {110} substrate the direction of the easy axis changes from [110] to [001] as the film thickness increases.[2] Similar results were obtained for an Fe(1$\bar{1}$0) film grown on a {110} substrate.[8]

Here we report results of an investigation of the anisotropic properties of Fe films grown by molecular beam epitaxy on GaAs(100) substrates. Gallium arsenide was chosen as the substrate material because, first, it is widely used for fabricating planar integrated microcircuits and second, its crystal lattice parameter is a multiple of the Fe crystal lattice parameter, at least to within 5%.

The Fe films were obtained using an ÉS 2301 electron spectrometer whose vacuum system incorporated the growth chamber for the molecular beam epitaxy and an analytical chamber for studying the elemental composition of the surface using Auger spectroscopy. The samples were moved between the chambers using a manipulator. Before the deposition process the pressure in the chamber was less than 10^{-9} Torr and during deposition it was no less than $\sim 10^{-8}$ Torr. The rate of deposition of the iron was 9–10 Å/min at a substrate temperature close to room temperature. The deposition times were 3, 7, 10, and 14 min, respectively for Fe film thicknesses $t_1\approx 30$ Å, $t_2\approx 70$ Å, $t_3\approx 100$ Å, and $t_4\approx 140$ Å (see Table I).

The GaAs(100) substrates were class 14 surface polished and had an in-plane size of $\sim 3\times 3$ mm. Before deposition, the substrates were cleaned chemically for 5 min in 40% KOH, rinsed in distilled water, treated with a $H_2SO_{4\,conc}:H_2O_{2\,conc}:H_2O$ (16 : 1 : 1) solution, again rinsed in distilled water and dried. Immediately before being placed in the growth chamber, the GaAs surface was cleaned with ultraviolet radiation as in Refs. 9 and 10, and then annealed for 30 min at $\sim 800\,^\circ$C. This treatment substantially reduced the level of carbon and oxygen impurities, which were monitored from the Auger spectra of the surface. The surface composition was monitored again after the end of the deposition process and indicated that an Fe film had formed.

The films were investigated using the ferromagnetic resonance (FMR) method at $f_0\approx 9.8$ GHz at room temperature. The samples were placed in a rectangular resonator so that the magnetic field H was tangential to the surface and formed the angle θ with the [100] direction (Fig. 1). The dependence of the resonance field H_r on the angle θ was recorded. The angle θ was measured to within (2–3)°.

The experimental orientational dependence of the resonance field on the angle of rotation of the films $H_r(\theta)$ was compared with the calculations of $H_r(\theta)$, which were made with allowance for the field of cubic $H_c=K_1/M_0$, normal uniaxial $H_\perp=2K_\perp/M_0$, and in-plane uniaxial anisotropy $H_\parallel=2K_\parallel/M_0$, where K_1, $K_\perp$, and $K_\parallel$ are the constants of cubic, normal uniaxial, and in-plane uniaxial anisotropy, respectively. It was also assumed that the direction of equilibrium magnetization M_0 forms the angle ψ with the direction of the field H_0 and the direction of the axis $\mathbf{l}$ of uniaxial in-plane anisotropy forms the angle β with the direction of the [100] axis (Fig. 1). The angle ψ was calculated from

$$-2H_0\sin\psi+H_c\sin 4\alpha+H_\parallel\sin 2\eta=0, \qquad (1)$$

where $\alpha=\theta-\psi$, $\eta=\alpha+\beta$. The expression to determine $H_r(\theta)$ then has the form

$$(H+4\pi M_0+H_\perp)(H-3H_c\sin^2 2\alpha-H_\parallel\sin^2\eta)=f_0^2/\gamma^2, \qquad (2)$$

where $H=H_r(\theta)\cos\psi+H_c(2-\sin^2\alpha)+H_\parallel\cos^2\eta$ and $\gamma=2.96$ is the gyromagnetic ratio for Fe.

 © 1999 American Institute of Physics

TABLE I. Film parameters.

No.	t, Å	$4\pi M_{\text{eff}}$, kG	H_c, Oe	$H_\parallel$	ΔH, Oe
1	30	8.48	–	–	210
2	70	14.2	–	–	150
		14.2	56	−80	100
3	100	15.5	–	–	190
		15.5	232	−156	50
4	140	14.5	252	−70	150

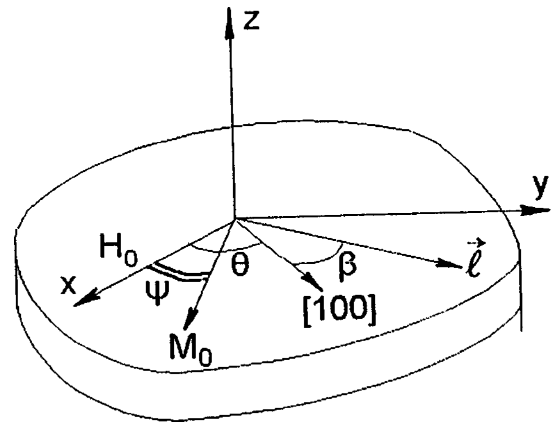

FIG. 1. Coordinate system.

Figures 2a and 2c give the experimentally determined dependence (circles) and the approximate dependence of the resonance field calculated using formulas (1) and (2) for these Fe films (see Table I). The insets to Fig. 2 give the typical dependence of the derivative of the power reflected from the resonator as a function of the static magnetic field $dP/dH_0(H_0)$, where the distance between the extrema corresponds to the FMR line width ΔH and the arrow indicates the position of the resonance field H_r.

It can be seen from Fig. 2a that at $f_0=9.8$ GHz in the range of fields H_0 = 0.5–5 kOe only one resonance absorption line is observed for films Nos. 1 and 4, which can be ascribed to the dominant FMR mode. Film No. 1, having the smallest thickness $t_1\approx 30$ Å, is isotropic (curve *1*), whereas for film No. 4 of thickness $t_4\approx 140$ Å the orientational dependence $H_r(\theta)$ indicates some anisotropy (curve *2*). The curve $H_r(\theta)$ for film No. 4 corresponds to the case in which a cubically anisotropic film having the direction of easy magnetization [100] ($K_1>0$) also possess uniaxial in-plane anisotropy with the easy axis directed along [110]. Table I gives the effective magnetizations of the films $4\pi M_{\text{eff}} = 4\pi M_0 + 2K_\perp/M_0$ and the anisotropy fields H_c and $H_\parallel$ selected using formulas (1) and (2), as well as the lowest recorded values of ΔH.

For Fe films of intermediate thicknesses, $t_2\approx 70$ Å and $t_3\approx 100$ Å, the FMR spectra revealed two absorption lines each, separated by the field $|\delta H_0|<1$ kOe (see inset to Fig. 2b). The behavior of the curves $H_r(\theta)$ for these lines was

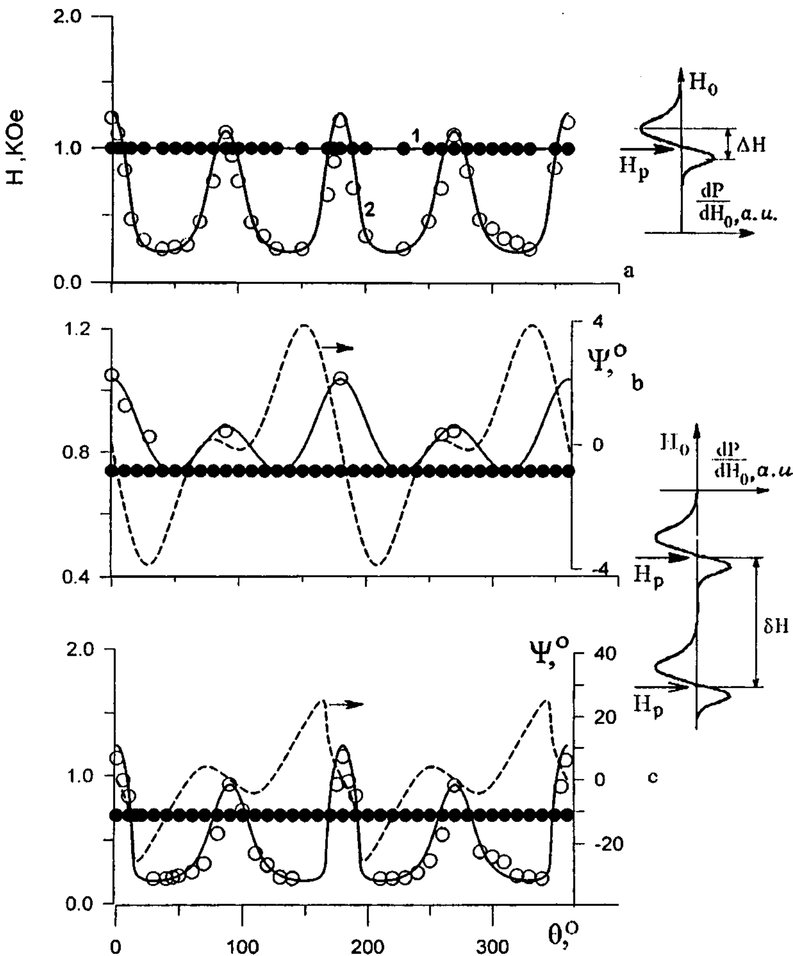

FIG. 2. Calculated dependence $H_r(\theta)$ (solid curve) and $\Psi(\theta)$ (dashed curve): a — for films Nos. 1 (curve *1*) and 4 (curve *2*), b — for film No. 2, and c — for film No. 3. The filled and open circles give the experimental data for the isotropic and anisotropic phases, respectively.

different and corresponded either to the isotropic case or to the case of a cubically anisotropic film with in-plane uniaxial anisotropy (see Figs. 2b and 2c).

The additional line observed for films Nos. 2 and 3 cannot be attributed to the excitation of nonuniform magnetization fluctuations characterized by an integral number of half-waves over the thickness ($n \geqslant 1$) and in the plane ($k,m \geqslant 1$) of the film. In fact, for Fe films having the magnetization $\pi M_0 = 12$ kG, exchange rigidity $A = 2\times 10^{-6}$ erg/cm, and thickness $t \leqslant 100$ Å the resonance fields of the dominant ($n=0$) and first ($n=1$) spin-wave resonance modes differ by

$$\delta H_0^{(0,1)} = \frac{\pi^2 2A}{t^2 M_0} \geqslant 40\,\text{kOe}, \tag{3}$$

which not only substantially exceeds the observed values of δH_0 but also the experimentally attainable range of variation of the field H_0. However, the difference between the resonance fields of the dominant mode and the mode having a nonuniform magnetization distribution in the plane of the film, can be estimated using the dispersion relation for the magnetostatic waves in a tangentially magnetized ferromagnetic film:[10]

$$\delta H_0^{(0,1)} \approx \frac{\pi^2 k t M_0}{L(1 + H_0/4\pi M_0)} < 0.1\,\text{Oe}, \tag{4}$$

where L is the length of one side of the film along which k half-waves fit.

The most probable reason for the appearance of two absorption lines in the FMR spectrum of films Nos. 2 and 3 may be the inhomogeneity of their surface texture, which shows up in the coexistence of isotropic and single-crystal phases. This may also be indicated by the change in the ratio of the amplitudes of the isotropic and anisotropic responses and by the broadening of the range of angles θ in which the anisotropic response is observed, with increasing film thickness in Figs. 2b and 2c.

This behavior may be attributed to the influence of exchange interaction at the boundaries of the anisotropic and isotropic phases when the directions of equilibrium magnetization M_0 within these phases differ. The misorientation of the magnetizations within the isotropic and anisotropic phases is determined by the angle ψ, which for the parameters corresponding to the anisotropic phases of films Nos. 2 and 3 varies in the ranges $|\psi| \leqslant 5°$ and $|\psi| \leqslant 25°$, respectively (see dashed curves in Figs. 2b and 2c). These figures show that only one isotropic response is observed in films Nos. 2 and 3 for those angles θ for which $|\psi|$ has the highest values. For $\psi \rightarrow 0$, which corresponds to magnetization in the $\langle 100 \rangle$ and $\langle 110 \rangle$ crystallographic direction ($\theta = \pi N/4$, where N is an integer), both isotropic and anisotropic responses are observed.

Note that the values of the parameters $4\pi M_{\text{eff}}$, H_c, and $H_\parallel$ in films Nos. 1 and 4 and their dependence on thickness are consistent with the data given in Refs. 2 and 6 for epitaxial Fe films on GaAs(100) and (110) substrates. However, the possible coexistence of the isotropic and anisotropic phases in Fe films has not yet been observed. In our view, the explanation lies in the surface state of the films. Figure 3 shows an image of part of the substrate surface obtained using a scanning atomic-force microscope. The roughness amplitude R_z of the substrate surface is $R_z \leqslant 200$ Å and is within the limits specified for class 14 substrate treatment but is still of the same order as the thicknesses of the deposited layers. An estimate of the mean square roughness amplitude σ, made by analogy with Ref. 11, gives $\sigma \approx 30$ Å. Comparing the values of σ and the film thickness t, we can see that for $t \leqslant \sigma$ an isotropic phase is formed, whereas for $t \geqslant 3\sigma$ the film exhibits cubic anisotropy. In the thickness range $\sigma < t < 3\sigma$ the film has both isotropic and anisotropic phases.

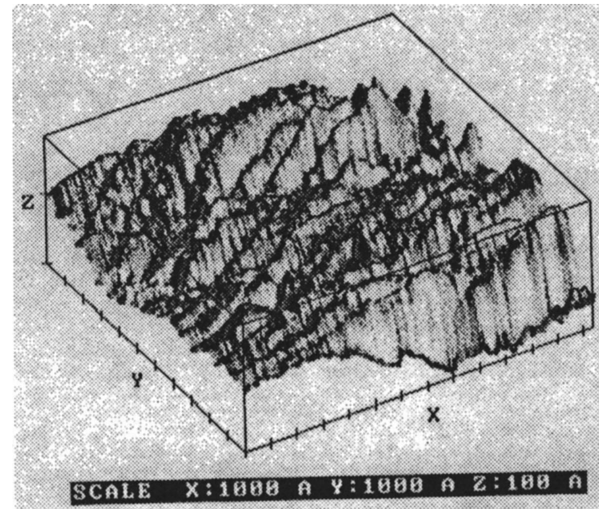

FIG. 3. Image of the surface of a GaAs substrate.

To conclude, we have shown that Fe films obtained by molecular beam epitaxy on standard GaAs(100) substrates whose surface has the roughness amplitude $R_z < 100$ Å and mean square $\sigma \approx 30$ Å, cubic magnetic anisotropy begins to appear starting with thicknesses t = 40–50 Å. For $t > 100$ Å the first constant of cubic anisotropy K_1 has values close to those for bulk Fe single crystals. Films of intermediate thickness $50 < t < 100$ Å exhibit both isotropic and anisotropic phases.

The authors are grateful to A. S. R'yanov, S. A. Sysuev, and S. A. Nikitov for assistance with the work and useful discussions.

This work was supported by the Russian Fund for Fundamental Research Grant No. 97-02-18614 and by Grant No. 97-3.16 under the State Program ''Topical Directions in Physics of Condensed Media,'' subprogram ''Surface Atomic Structures.''

[1] G. A. Prinz and J. J. Krebs, Appl. Phys. Lett. **39**, 397 (1981).
[2] G. A. Prinz, G. T. Rado, and J. J. Krebs, J. Appl. Phys. **53**, 2087 (1982).
[3] B. Hillebrands, Phys. Rev. B **41**, 530 (1990).
[4] Eric. E. Fullerton, M. J. Conover, J. E. Mattson *et al.*, Appl. Phys. Lett. **63**, 1699 (1993).
[5] W. Folkerts and F. Hakkens, J. Appl. Phys. **73**, 3922 (1993).

[6] Yu. V. Goryunov, N. N. Garif'yanov, G. G. Khaliullin *et al.*, Phys. Rev. B **52**, 13 450 (1995).
[7] Y. Endo, S. Okamoto, O. Kitakami *et al.*, J. Appl. Phys. **81**, 344 (1997).
[8] K. Kawagachi and M. Sohma, Phys. Rev. B **46**, 14 772 (1992).
[9] M. Tabe, Appl. Phys. Lett. **45**, 1073 (1984).
[10] A. G. Gurevich and G. A. Melkov, *Magnetic Oscillations and Waves*, CRC Press, Boca Raton, FL, (1996); [Russ. orig., Fizmatlit, Moscow (1994), 464 pp.].
[11] Chin Y. Poon and B. Bhushan, J. Appl. Phys. **79**, 5799 (1996).

Translated by R. M. Durham